TURUN
YLIOPISTO
UNIVERSITY
OF TURKU

CANTILEVER ENHANCED PHOTOACOUSTIC SPECTROSCOPY

The First Two Decades

Vesa Koskinen

TURUN YLIOPISTON JULKAISUJA – ANNALES UNIVERSITATIS TURKUENSIS
SARJA – SER. AI OSA – TOM. 706 | ASTRONOMICA – CHEMICA – PHYSICA – MATHEMATICA | TURKU 2024

TURUN
YLIOPISTO
UNIVERSITY
OF TURKU

CANTILEVER ENHANCED PHOTOACOUSTIC SPECTROSCOPY

The First Two Decades

Vesa Koskinen

TURUN YLIOPISTON JULKAISUJA – ANNALES UNIVERSITATIS TURKUENSIS
SARJA – SER. AI OSA – TOM. 706 | ASTRONOMICA – CHEMICA – PHYSICA – MATHEMATICA | TURKU 2024

University of Turku

Faculty of Science
Department of Physics and Astronomy
Physics
Doctoral programme in Exact Sciences

Supervised by

Adjunct Professor, Tom Kuusela
Department of Physics and Astronomy
University of Turku
Turku, Finland

Professor Emeritus, Jyrki Kauppinen
Department of Physics and Astronomy
University of Turku
Turku, Finland

Reviewed by

Adjunct Professor, Satu Ojala
Faculty of Technology
University of Oulu
Oulu, Finland

Adjunct Professor, Markus Metsälä
Department of Chemistry
University of Helsinki
Helsinki, Finland

Opponent

Professor, Ilkka Tittonen
Department of Electronics and Nanoengineering
Aalto University
Helsinki, Finland

ISBN 978-951-29-9612-4 (PRINT)
ISBN 978-951-29-9613-1 (PDF)
ISSN 0082-7002 (PRINT)
ISSN 2343-3175 (ONLINE)
Painosalama, Turku, Finland, 2024

UNIVERSITY OF TURKU
Faculty of Science
Department of Physics and Astronomy
Physics
KOSKINEN, VESA: Cantilever Enhanced Photoacoustic Spectroscopy
Doctoral dissertation, 129 pp.
Doctoral programme in Exact Sciences
February 2024

ABSTRACT

Two decades ago, the first experiments with a novel optical microphone using a small silicon cantilever as its sensing element were conducted at the University of Turku. In retrospect, those experiments revealed the potential enhancing the sensitivity of photoacoustic spectroscopy (PAS) by using this cantilever microphone as a replacement for the conventionally used condenser microphone. In just a few years, this replacement had led to a very sensitive technique, nowadays known as cantilever enhanced photoacoustic spectroscopy, CEPAS. The introduction of CEPAS and its first years of development including a complete physical model of the system are described in the first part of this thesis. Covering the first two decades after the introduction of CEPAS, the latter part presents a unique retrospective study on its influence on the applied spectroscopy research.

During the introduction of CEPAS as well as in the early development of the technique, a broadband IR source was used. For the comparison to the other techniques, the same unoptimized prototype with a tunable diode laser source was used to detect carbon dioxide. The achieved normalized noise equivalent sensitivity (NNEA) was at the same level as the best ever reported by PAS until then. The detector was then optimized for laser sources mainly by changing the properties of the cantilever and the design of the cell, that enabled minimizing the dead volume of the sample cell. This optimization of the detector in 2007 led to a NNEA value of $1.7 \times 10^{-10}\mathrm{cm}^{-1}\mathrm{W}/\sqrt{\mathrm{Hz}}$. At that time it was the best ever reported in PAS and is still – after fifteen years – among the very best ones. The realized sensitivity as well as the presented future improvements were based on the accuracy of the developed physical model.

CEPAS has been used in several applications, ranging from medical and pharmaceutical sciences to the detection of radioactive and toxic materials or greenhouse gases. In several application areas it is only just taking its first steps. CEPAS has also inspired hundreds of scientific publications, numerous research projects as well as new techniques. Nowadays, it has become a recognized and functional technique that has already had and still has impact on several scientific fields worldwide.

KEYWORDS: Photoacoustic spectroscopy, trace gas analysis, cantilever microphone

TURUN YLIOPISTO
Matemaattis–luonnontieteellinen tiedekunta
Fysiikan ja tähtitieteen Laitos
Fysiikka
KOSKINEN, VESA: Cantilever Enhanced Photoacoustic Spectroscopy
Väitöskirja, 129 s.
Eksaktien tieteiden tohtoriohjelma
Helmikuu 2024

TIIVISTELMÄ

Kaksi vuosikymmentä sitten tehtiin Turun yliopistolla ensimmäiset tutkimukset optisella mikrofonilla, jonka anturina käytettiin pientä piiläppää. Jälkikäteen arvioituna jo nuo ensimmäiset kokeet paljastivat potentiaalin, joka fotoakustisen spektroskopian herkkyyden parantamiseksi oli saavutettavissa korvaamalla yleisesti käytetty kondensaattorimikrofoni tällä optisella läppämikrofonilla. Muutamassa vuodessa tutkimukset johtivat erittäin herkkään tekniikkaan, joka sittemmin on nimetty läppäavusteiseksi fotoakustiseksi spektroskopiaksi (englanniksi cantilever enhanced photoacoustic spectroscopy, CEPAS). Tässä väitöskirjassa kuvataan näiden vuosien aikana tehty tutkimus, joka sisältää mm. menetelmän fysikaalisen mallinnuksen. Kirjan jälkimmäisessä osassa esitetään kahden vuosikymmenen tieteelliseen kirjallisuuteen perustuva taannehtiva selvitys menetelmän vaikutuksesta tieteelliseen tutkimukseen.

Menetelmää julkaistaessa sekä ensimmäisissä tutkimuksissa sen herkkyyden osoittamiseksi käytettiin laajakaistaiselle infrapunalähteelle suunniteltua prototyyppiä. Samaa laserkäyttöön optimoimatonta prototyyppiä käytettiin myös säädettävän diodilaserlähteen kanssa hiilidioksidimittauksissa, joiden perusteella menetelmän herkkyyttä kyettiin vertaamaan muihin menetelmiin. Määritetty normalisoitu herkkyys (NNEA) oli heti parhaiden fotoakustisessa spektroskopiassa julkaistujen tulosten tasolla. Laserlähteelle optimoinnin ansiosta menetelmällä saavutettiin vuonna 2007 NNEA-arvo 1,7 $\times 10^{-10}\mathrm{cm}^{-1}\mathrm{W}/\sqrt{\mathrm{Hz}}$. Tulos oli siihen mennessä paras fotoakustisessa spektroskopiassa saavutettu, ja on edelleen yli viidentoista vuoden jälkeen yksi parhaista. Herkkyyden parannus sekä samassa yhteydessä esitetyt mahdolliset tulevat keinot sen parantamiseen edelleen perustuivat menetelmän fysikaalisen mallinnuksen tarkkuuteen.

Tieteellisen kirjallisuuden perusteella CEPAS-menetelmää on käytetty lukuisissa sovelluksissa aina lääke- ja farmaseuttisesta tieteistä radioaktiivisten ja myrkyllisten aineiden sekä kasvihuonekaasujen havaitsemiseen. Lisäksi useilla sovellusalueilla menetelmän käyttöönotto on vielä alkutekijöissään. CEPAS-menetelmää on käytetty, tutkittu ja kehitetty sadoissa tieteellisissä julkaisuissa sekä lukuisissa tutkimusprojekteissa, opinnäytetöissä ja uusissa tekniikoissa. Kahden vuosikymmenen aikana siitä on kehittynyt tunnustettu ja käytännöllinen tekniikka, jolla on ollut ja on edelleen vaikutusta usealla tieteenalalla maailmanlaajuisesti.

ASIASANAT: fotoakustinen spektroskopia, kaasuanalyysi, läppämikrofoni

Acknowledgements

The experimental part of the present work has mainly been carried out in the Laboratory of Optics and Spectroscopy at the Department of Physics and Astronomy, University of Turku, during the years between 2003 and 2008; the literature review in the latter part of the thesis in 2023.

I wish to express my sincerest gratitude to my supervisors, Professor emeritus Jyrki Kauppinen and Docent Tom Kuusela.

I am very grateful to all my co-authors for their valuable contribution. Especially, I want to thank M.Sc. Juha Fonsen for his valuable co-operation and M.Sc. Kari Roth for all the help he provided with his excellent programming skills. I would also like to thank the members of the former Laboratory of Optics and Spectroscopy not only for their valuable work but also for keeping up the pleasant atmosphere.

Docent Satu Ojala and Docent Markus Metsälä are gratefully acknowledged for carefully reviewing this thesis.

I would like to thank my current employer, Sirate Group Oy, as well as my current and previous colleagues for their support and encouragement on this journey.

I owe my warmest thanks to my parents for their never-ending support and presence. This work would never have been completed without my wife's constant care for our family and especially for the health of our children. Finally, I would like to thank my children Eino, Atte and Sohvi for bringing so many wonderful aspects into my life and for teaching what really is important in life.

21.12.2023
Vesa Koskinen

Table of Contents

Abbreviations

AFM	Atomic force microscope
AM	Amplitude modulation
AOPAS	All-optical photoacoustic spectrometer
ATR	Attenuated total reflectance, see FTIR
CE	Cavity-enhanced
CEPAS	Cantilever enhanced photoacoustic spectroscopy
CERPAS	Cantilever enhanced resonant photoacoustic spectroscopy
CM	Centre of mass
CWA	Chemical warfare agents
DFB	Distributed feedback laser
DR-FTIR	Diffuse reflectance Fourier transform Infrared
EDFA	Erbium-dobed fibre amplifier
EMBIR	Electrically modulated broadband infrared
FFT	Fast Fourier Transform
FTIR	Fourier transform Infrared
FTIR-PAS	Fourier transform Infrared-Photoacoustic spectroscopy
FWHM	Full-width at half-maximum
GHG	Greenhouse gases
HITRAN	High-resolution transmission molecular absorption database
HWHM	Half-width at half-maximum
IAQ	Indoor air quality
IR	Infrared
ISI-WoS	ISI Web of Science (citation database)
LED	Light emitting diode
NEC	Noise-equivalent concentration
NNEA	Normalized noise equivalent absorption coefficient
OBD	Optical beam deflection
OPO	Optical parametric oscillator
PA	Photoacoustic
PAI	Photoacoustic imaging
PAS	Photoacoustic spectroscopy
ppb	parts per billion (10^{-9}) by volume
ppm	parts per million (10^{-6}) by volume

ppt	parts per trillion (10^{-12}) by volume
PVDF	poly(vinylidene fluoride)
QCL	Quantum cascade laser
QEPAS	Quartz enhanced photoacoustic spectroscopy
Scopus	Elsevier API Scopus (citation database)
SNR	Signal-to-Noise ratio
TDL	Tunable diode laser
TDLPAS	Tunable diode laser based photoacoustic spectroscopy
VOC	Volatile organic compound
WM	Wavelength modulation

List of Original Publications

This dissertation is based on the following original publications, which are referred to in the text by their Roman numerals:

I J. Kauppinen, K. Wilcken, I. Kauppinen, and V. Koskinen.
High Sensitivity in Gas Analysis with Photoacoustic Detection, Microchem. J. **76**, 151–159 (2004).

II T. Laurila, H. Cattaneo, V. Koskinen, J. Kauppinen, and R. Hernberg.
Diode Laser-Based Photoacoustic Spectroscopy with Interferometrically-Enhanced Cantilever Detection, Optics Express, **13**, 2453–2458 (2005). Erratum: Optics Express, **14**, 4195 (2006).

III V. Koskinen, J. Fonsen, J. Kauppinen, and I. Kauppinen.
Extremely Sensitive Trace Gas Analysis with Modern Photoacoustic Spectroscopy, Vibr. Spectrosc. **42**, 239–242 (2006), (Proc. of Int. Conf. on Advanced Vibrational Spectroscopy, ICAVS-3, Delavan, Wisconsin, USA 2005).

IV V. Koskinen, J. Fonsen, K. Roth, and J. Kauppinen.
Cantilever Enhanced Photoacoustic Detection of Carbon Dioxide Using a Tunable Diode Laser Source, Appl. Phys. B **86**, 451–454 (2007), Rapid communication.

V V. Koskinen, J. Fonsen, K. Roth, J. Kauppinen.
Progress in cantilever enhanced photoacoustic spectroscopy, Vibr. Spectrosc. **48**, 16–21 (2008), (Proc. of Int. Conf. on Advanced Vibrational Spectroscopy, ICAVS-4, Corfu, Greece 2007)

VI J. Fonsen, V. Koskinen, K. Roth and J. Kauppinen.
Dual cantilever enhanced photoacoustic detector with pulsed broadband IR-source, Vibr. Spectrosc. **50**, 214–217 (2009)

The following articles to which I have contributed are related to this work but are not included in this thesis:

[1] J. Kauppinen, V. Koskinen, I. Kauppinen and J. Uotila,
Extremely sensitive CWA analyzer based on a novel optical pressure sensor in photoacoustic gas analysis, Proc. of SPIE, **5617**, 115-127 (2004), (Optically based biological and chemical sensing for defence, London, UK 2004).

[2] J. Uotila, V. Koskinen, J. Kauppinen,
Selective differential photoacoustic method for trace gas analysis,
Vibr. Spectrosc. **38**, 3-9 (2005).

[3] T. Laurila, H. Cattaneo, T. Pöyhönen, V. Koskinen, J. Kauppinen and R. Hernberg,
Cantilever-based photoacoustic detection of carbon dioxide using a fiber-amplified diode laser, Appl. Phys. B **83**, 285-288 (2006).
Erratum: Appl. Phys. B **83**, 669 (2006).[4]

1 Introduction

Infrared (IR) spectroscopic methods have been one of the leading technologies to meet the increasing demands for sensitive, selective and non-destructive gas analysis. The need for trace gas applications regards several fields such as environmental monitoring [5; 6], aerosol measurements [7], industrial and traffic emissions [8], exhaled breath analysis [9; 10; 11], indoor air quality (IAQ) measurements [12; 13], and detection of toxic gases [14; 15], chemical warfare agents (CWA) [1; 16], explosives [16; 17], and illicit drugs [18].

At the beginning of the 2000s low-resolution Fourier transform infrared (FTIR) spectrometers were known to be the best multicomponent gas analysers using broadband black body sources and conventional absorption technique. However, they were already developed very close to their theoretical performance limits. Thus, further development demanded new approaches like photoacoustic spectroscopy (PAS). As a zero background method, PAS was a promising method in order to overcome those limits, even though it was known to lack both temperature and pressure immunity as well as the required sensitivity with broadband IR sources. Luckily, the sensitivity of the PAS was limited by the microphone, which could be replaced with a more sensitive pressure sensor as presented in Ref. [19] and Paper I. The use of PAS could also enable the measurement of solid and liquid samples without preparation as well as new applications such as depth profiling of surfaces and layered samples [20], opaque or dark matter measurements, 3D imaging [21; 22] and carbon dating [23].

The first part of this thesis introduces the first steps in the research and development of a technique, later named as cantilever enhanced photoacoustic spectroscopy (CEPAS). It is based mainly on the research done between the years 2003 to 2008 at the University of Turku, Finland. Starting from the invention of the silicon cantilever sensor, the major milestones to a proven technique, that was ready to be commercialized, are presented. The basic theory and limitations of conventional PAS are described in Chapter 2. Chapter 3 reveals the major steps to overcome these limitations. The main results achieved during those early years are shortly described, including the demonstration of the sensitivity (Papers I, II and IV), huge linear range (Paper III), modelling the CEPAS (Paper V), noise sources and their compensation (Papers V and VI) and the demonstrations of the usability of CEPAS in different measurements schemas, such as the differential method (Paper III), FTIR setup (Paper V) and with electrically modulated broadband IR sources (Paper VI).

A timeline of two decades after the invention of the cantilever microphone enables a unique retrospective study of the impact of the technique on scientific literature. This study based on scientific publications is presented in the latter part of this thesis and reveals the importance of the CEPAS as the most recent major developmental milestone in the history of photoacoustics. Due to its high sensitivity and selectivity, huge linear dynamic range, robustness and ability to be miniaturized together with constantly developing laser technology, CEPAS has offered solutions to several above-mentioned real-world problems. It has been utilized in at least over 250 of scientific articles and conference presentations as well as several doctoral theses and international research projects. On the other hand, the literature review indicates the accuracy of the presented physical model and the validity of the results achieved already by 2008. Even though the detection limits have been lowered by orders of magnitude mainly due to the development of laser technology, the sensitivities of the PA detectors have not in most cases improved at all. The highest sensitivity achieved in 2007 Paper IV is still one of the best ever reported regardless the several attempts to improve the system. Based on the literature review presented in Chapter 5 it is legitimate to claim that the method and results presented almost two decades ago has had and still has a remarkable impact on a number of scientific fields worldwide.

2 Photoacoustic Spectroscopy

Photoacoustic spectroscopy (PAS) combines the photoacoustic (PA) effect with optical spectroscopy, providing a non-destructive and zero background method for studying the properties of gases, liquids, and solids. Interest in PAS has alternately declined and increased as a result of the significant developmental steps during its history that began in the 1880s. This chapter begins with a brief history review of PAS and provides basic information about absorption and spectral line profiles required to understand the PAS and its sensitivity. The theory of traditional PAS, as well as the advantages and limitations of the method, are also presented.

2.1 Brief History

The PA effect was observed by Alexander Graham Bell and Mr. Summer Tanter in 1880 while studying the photophone. [24] A rapidly interrupted beam of sunlight, focused on a sample material in a sealed glass tube, emitted sound that could be heard through a hearing tube. Bell also founded out that the strength of the signal was dependent on how strongly the incident light was absorbed by the material in the tube. [25] Among Bell, also John Tyndal [26] and Wilhelm Röntgen [27] studied the effect especially with gas samples and it was already in the 1880s correctly assumed that the sample absorbed all or part of the chopped incident radiation and, by doing so, was itself periodically heated. In the studies with gas samples the heating resulted straight in pressure changes. In case of solid and liquid samples, the pressure changes were produced into a transfer gas surrounding the sample. These changes were periodical, having the same frequency as the light was chopped. [28, p. 10]

The replacement of the hearing tube with a newly invented condenser microphone enabled more practical and quantitative measurements. Thus, according to Ref. [28, p.13] the first major milestone in PA gas analysis was reached in 1938, as Viengerov [29] began using the microphone to study infrared (IR) light absorption in gases and to evaluate the concentrations of gaseous species in gas mixtures. He was able to measure ~ 0.2 vol-% CO_2 concentrations in N_2. Measurements at lower concentrations were limited both by the low sensitivity of his microphone and by the background absorption of the incident radiation by the cell windows and walls. In 1943, Luft [30] described a commercial PA gas analyser utilizing two PA cells in a differential setup, which had the sensitivity of a few parts per million (ppm). [31]

However, the use of the method fell short due to more sensitive analysis techniques involving gas chromatography. [28; 32]

The next major developmental steps in PAS were taken in the late 1960s and 1970s by utilizing the recently discovered electret microphones and lasers. [33; 34; 5] The development of the technique during the next decades is thoroughly reviewed in a book by Michaelian. [34] At the end of the 20^{th} century PAS with laser sources was recognized as a sensitive tool for gas analysis. However, with a broadband black body radiation source, it was known to be less sensitive than FTIR analysers. [31] Therefore, several techniques, adapted especially from the atomic force microscopy (AFM [35; 36; 37]), were developed to replace the capacitive microphone as a sensing element. The optical approach was represented by optical beam deflection (OBD) sensing the displacement of the microphone membrane [38] or a pellicle [39; 40] and by interferometric measurement. [41]

The latest major developmental milestone in the history of PA in gas analysis was the replacement of the condenser or electret microphone in the measurement setup with a more suitable sensor during the early 2000s. [42] The most important ones of those alternative sensors have shown to be a quartz tuning fork in quartz-enhanced photoacoustic spectroscopy (QEPAS) [43] and a silicon cantilever in CEPAS introduced in Ref. [19] and Paper I.

2.2 Absorption Spectroscopy

Spectroscopy can be defined as the study of the interaction of radiation with matter. In optical spectroscopy, where wavelengths vary from the x-rays to the far infrared, the energies are usually too low to significantly alter the material being studied. Conventional spectroscopic measurements tend to fall into two major categories: the study of the light that is transmitted through the material of interest (i.e. the study of those photons that did not interact with the material), and the study of the light that is scattered or reflected from the material. In contrast to them, the energy absorbed by the material is measured directly in PAS. [28]

2.2.1 Beer's Law

When light (electromagnetic radiation) penetrates through an absorbing sample gas x as in Fig. 1, absorption is described by Beer's law:

$$I(\nu) = I_0(\nu)e^{-\alpha_x(\nu)c_xL}, \tag{1}$$

where $I_0(\nu)$ and $I(\nu)$ are incident and transmitted intensities, $\nu = 1/\lambda$ is the wave number of the radiation in inverse centimetres, λ is the wavelength, L is the thickness of the sample (optical path length), c_x the concentration and $\alpha_x(\nu)$ the substance and

wavenumber specific absorption coefficient. [44] In this thesis, concentrations[1] (and detection limits) c_x are expressed by using notations ppm (part per million, 10^{-6}), ppb (part per billion, 10^{-9}) and ppt (parts per trillion, 10^{-12}) by volume. They are always compared with the atmospheric pressure p_0, so that they are independent of the total pressure[2], i.e., the partial pressure $p_x = c_x p_0$.

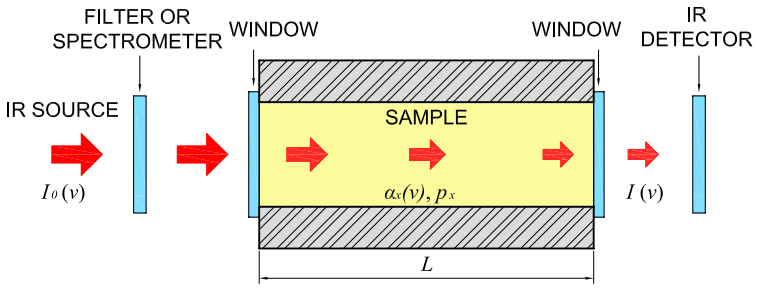

Figure 1. The absorption of radiation. Incident and transmitted intensity are denoted as $I_0(\nu)$ and $I(\nu)$; $\alpha_x(\nu)$, c_x and L are the absorption coefficient, concentration and thickness of the sample.

Further, the fraction $[I_0(\nu) - I(\nu)]/I_0(\nu)$ is called absorption, $I(\nu)/I_0(\nu)$ transmittance, $-\ln[I(\nu)/I_0(\nu)] = \alpha_x(\nu)c_x L$ absorbance. The absorbance as a function of the wave number is called simply the (infrared) absorption spectrum. If the absorbance is small, then $I_0 - I = I_0\left[1 - e^{-\alpha_x c_x L}\right] \approx \alpha_x c_x L I_0$.

The absorption spectrum of the sample gas can be measured, for example, with a FTIR spectrometer. This requires the recording of transmitted radiation when incident radiation is modulated by an interferometer and has to done separately with and without sample gas in the cell. The recorded signals generate sample and background interferograms that can be converted to spectra by Fourier transform (FFT) as shown in Fig. 2. For the transmittance spectrum, the sample spectrum has to be divided by the background spectrum. In trace gas analysis, the sample gas concentrations are usually very low and the absorbed part of the incident radiation is almost negligible to the transmitted one. Therefore, the sample and background spectra are almost identical and the baseline drifts due to interferometer instabilities can be significant in the weak absorbance spectrum.

2.2.2 Absorption Coefficient and Line Intensity

The absorption coefficient $\alpha_x(\nu)$ can be expressed in terms of a line intensity S_x and an area-normalized line shape function $\Phi(\nu)$ as

$$\alpha_x(\nu) = \rho_N S_x \Phi(\nu) = \rho_N \sigma_x(\nu), \tag{2}$$

[1] Both c_x and p_x has been used in Papers I–VI to express the concentrations or partial pressures of the specific gas component x.

[2] For example, 1000 ppm always matches a partial pressure of 0.001 atm $\approx$ 1 mbar.

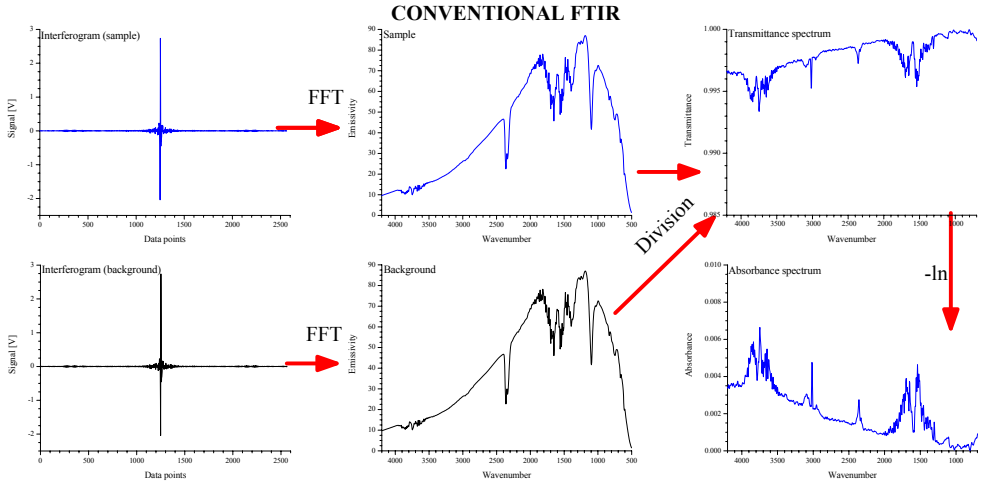

Figure 2. The process of calculating the absorbance spectrum of the sample gas from the separately recorded sample and background interferograms.

where ρ_N is the number density of the absorbing gas, $\sigma_x(\nu) = S_x\Phi(\nu)$ the absorption cross-section, and the dimensionless quantity $\alpha_x(\nu)L$ is called optical density. [45; 46] By using the ideal gas law the number density can be estimated to

$$\rho_N = \frac{p_x N_A}{RT}, \tag{3}$$

where N_A, R, and T are Avogadro's constant, the universal gas constant and absolute temperature, correspondingly. The line intensities of various transitions can be found in large databases, e.g. HITRAN [47].

2.2.3 Spectral Line Profiles

A spectral line extends over a range of wavenumbers (wavelengths), not a single one. This wavenumber dependence on spectral transitions can be taken into account in the absorption coefficient by normalized line shape functions $\Phi(\nu)$, which depend on the broadening mechanisms of the initial and final states. The most important broadening mechanisms in PAS are natural and pressure broadening producing Lorentzian line shapes and thermal Doppler broadening which has a Gaussian line shape. Combinations of Lorentzian and Gaussian line shapes can be approximated by their convolution i.e. by the Voigt profile.

Natural broadening – Lorentzian profile

The natural line width arises from the uncertainty in the energy of the states involved in the spectral transition. [48] According to Heisenberg's uncertainty principle the

energy levels E_i have finite widths ΔE_i, i.e.,

$$\Delta E_i \Delta t_i \geq \hbar. \tag{4}$$

Thus, the excited states having a finite lifetime Δt_i do not have a definite energy. The average energy of the outgoing photon has a peak at the theoretical energy of the state, but the distribution has a finite width called the natural line width. This broadening effect is described by a Lorentzian profile

$$\Phi_L(\nu) = \frac{\gamma}{2\pi} \frac{1}{(\nu_0 - \nu)^2 + \frac{\gamma^2}{4}}, \tag{5}$$

but in PAS, it is usually negligible in comparison to pressure and Doppler broadening.

Pressure Broadening – Lorentzian Profile

The collision of other particles with the absorbing particle interrupts the process. [49; 50] This collision induced broadening yield Lorentzian line profile. [51] The half-widths of the lines can be corrected by using the values (from e.g. the HITRAN database [47]) of the air broadened HWHM (half-width at half-maximum) γ_{air} and the self broadened HWHM γ_{self} at the reference temperature T_{ref} = 296 K and pressure p_{ref} =1 atm. The equation for the correction is [46]:

$$\gamma(p, T) = \left(\frac{T_{\text{ref}}}{T}\right)^n \left[\gamma_{\text{air}}(p_{\text{ref}}, T_{\text{ref}})(p - p_x) + \gamma_{\text{self}}(p_{\text{ref}}, T_{\text{ref}})p_x\right], \tag{6}$$

where n is temperature-dependence exponent for γ_{air}, and p is the total pressure. Thus, the full width at half maximum (FWHM) of the pressure broadening is

$$\Delta\nu_{\text{L}} = 2\gamma(p, T). \tag{7}$$

Doppler Broadening – Gaussian Profile

Due to the Doppler effect, the thermal movement of atoms or molecules shifts the apparent frequency of each emitter. The Maxwell–Boltzmann distribution of these (nonrelativistic) velocities leads to the Doppler or Gaussian profile

$$\Phi_{\text{G}}(\nu) = \frac{2}{\Delta\nu_{\text{G}}} \sqrt{\frac{\ln 2}{\pi}} \exp\left[-\left(\frac{2\ln 2(\nu - \nu_0)}{\Delta\nu_{\text{G}}}\right)^2\right], \tag{8}$$

where $\Delta\nu_{\text{G}}$ is the FWHM of the profile [52], i.e.,

$$\Delta\nu_{\text{G}} = \nu_0 \sqrt{\frac{8k_B T \ln 2}{mc^2}}.$$

In these equations, ν_0 is the wave number of the line centre, k_B is the Boltzmann constant, T is the absolute temperature, m is the mass of the emitter, and c is the speed of light.

Voigt Profile

Usually, both Doppler and pressure broadening contribute to the total lineshape, which in such a case is a convolution of these mechanisms. The convolution of Gaussian and Lorentzian profiles yields a Voigt profile [53]

$$\Phi_{\mathrm{Voigt}}(\nu,T,p) = \frac{2\sqrt{\ln 2}}{\pi^{2/3}}\frac{a}{\Delta\nu_{\mathrm{G}}}\int_{-\infty}^{\infty}\frac{e^{-t^2}}{(u-t)^2+a^2}\mathrm{d}t \qquad (9)$$
$$= \frac{2\ln 2}{\pi^{2/3}}\frac{\Delta\nu_{\mathrm{L}}}{\Delta\nu_{\mathrm{G}}^2}\int_{-\infty}^{\infty}\frac{e^{-t^2}}{\left(\frac{\nu-\nu_0}{\Delta\nu_{\mathrm{G}}}2\sqrt{\ln 2}-t\right)^2+\ln 2\left(\frac{\Delta\nu_{\mathrm{L}}}{\Delta\nu_{\mathrm{G}}}\right)^2}\mathrm{d}t,$$

where the Voigt parameter a (the ratio of the Lorentz to Doppler widths) and the wavenumber scale u are

$$a = \sqrt{\ln 2}\frac{\Delta\nu_{\mathrm{L}}}{\Delta\nu_{\mathrm{G}}} \qquad (10)$$

$$u = 2\sqrt{\ln 2}\frac{\nu-\nu_0}{\Delta\nu_{\mathrm{G}}}. \qquad (11)$$

HITRAN 2004 based Voigt profile simulations of the CO_2 lines investigated in Paper IV are shown in Figures 3 and 4.

2.3 Conventional Photoacoustic Spectroscopy

In contrast to conventional absorption technique, an example of a measurement setup for PA gas detection is shown in Figure 5. The modulated light beam from the IR source enters a closed cell filled with the gaseous sample. All or a portion of the incident radiation is absorbed by the gas resulting in pressure waves that are converted into an electrical signal by means of a microphone located inside the cell.

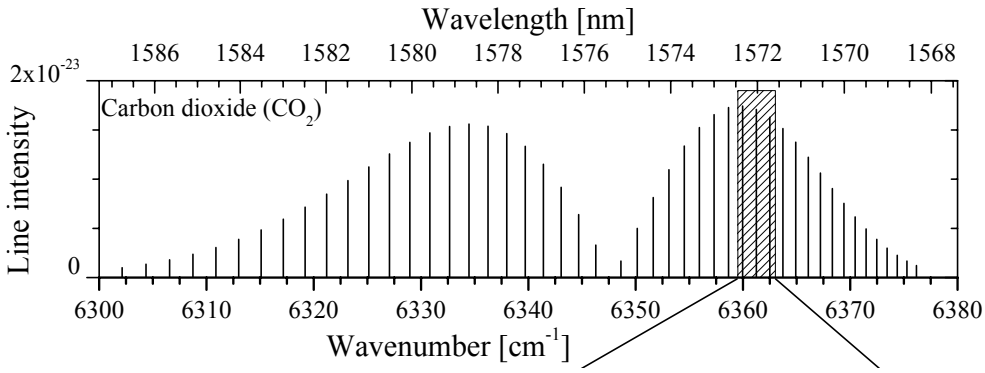

Figure 3. In paper IV, the fairly weak rotational line R(18) in the $[00^00]_{\mathrm{I}} \rightarrow [30^01]_{\mathrm{II}}$ vibrational band was selected for the CO_2 measurement by the laser availability.

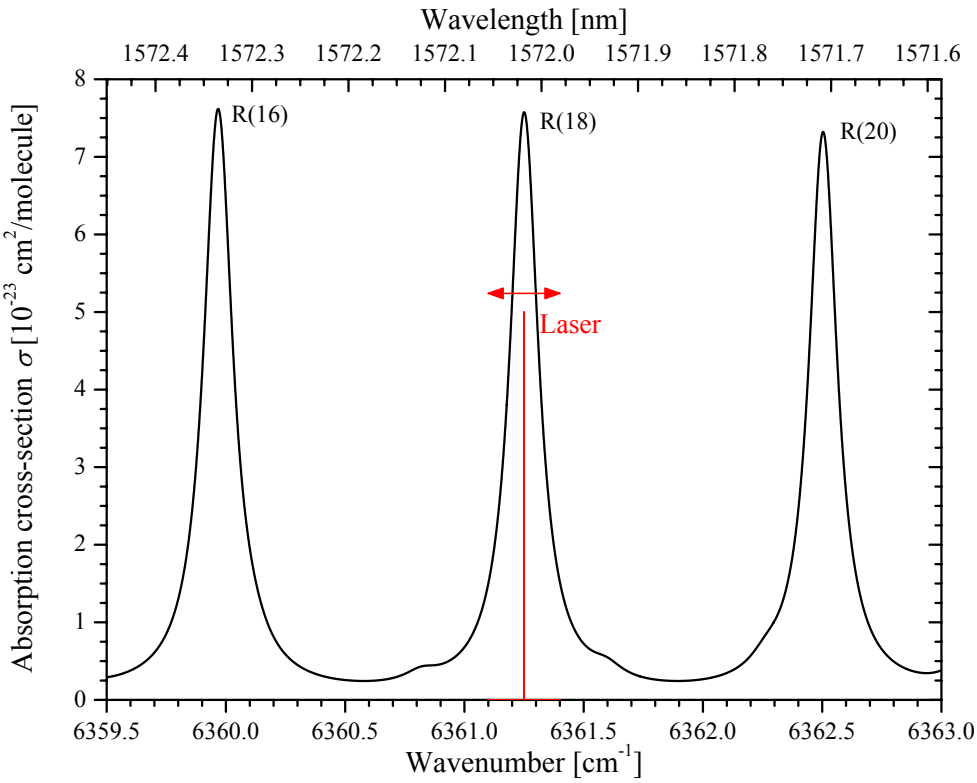

Figure 4. Modulation of the laser wavelength and HITRAN 2004 based Voigt profile simulation (at 296 K temperature and atmospheric pressures) of the CO_2 lines investigated in Paper IV.

The main difference in regard to the setup shown in Figure 1 is that there is no need to measure the incident and the transmitted intensities. The selectivity is achieved by using a proper optical filter or by selecting a laser wavelength according to the absorption lines of the investigated sample gas.

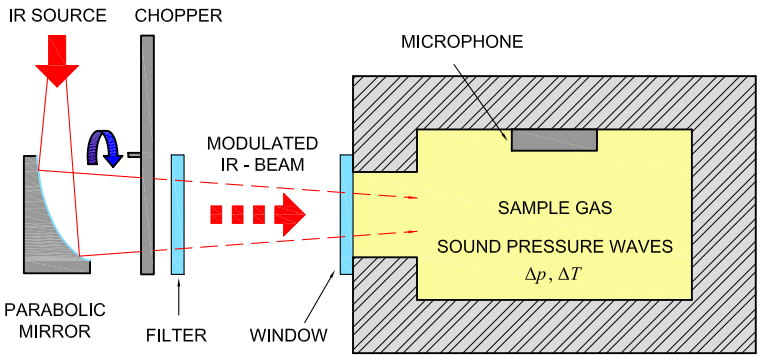

Figure 5. An example of a PA gas measurement setup (Paper III).

Thus, in PAS the signal is created from the absorbed part of the incident radiation, not from the transmitted or scattered parts, as in most other spectroscopic techniques. By selecting the wavelength of the incident radiation based on the gas under study, the signal is produced only if there is a gas component of interest in the sample. Further on, the signal is straight proportional to the concentration of the investigated gas.

2.3.1 Photoacoustic Effect in Gases

When a sample molecule absorbs a photon, it goes from its ground state E_0 to an excited state E_1 (usually a vibrational stage in trace gas analysis, where IR radiation is commonly used). The energy difference between the states is $E_1 - E_0 = hf$, where h is the Planck's constant and f is the frequency of the absorbed photon. The molecule can then lose this energy and return to the ground state through radiative or nonradiative pathways. [28] Because the radiative lifetimes of vibrational levels are long compared with the time needed for collisional deactivation at pressures used in photoacoustics ($\sim$1 atm), the absorbed energy is mainly released as heat, appearing as translational (kinetic) energy of the gas molecules. [54]

Due to the thermal nature of the PA process, the signal can be increased by increasing the heating power of incident radiation or by decreasing the amount of gas to be heated i.e. decreasing the size of the sample cell. To be more specific, the signal is maximized by minimizing the so called dead volume i.e. the parts of the cell, where the incident radiation can not enter. As mentioned in Paper IV, the signal can be further increased by enabling the multiple passing of the light beam through the sample gas. Due to the slowness of thermal processes, the signal is highest at low modulation frequencies.

Acoustical Modes of the Sample Cell

Due to the ambient acoustic noise, the PA signal is almost without exception measured in a closed sample cell. The cell has its own acoustical modes, which can be used to amplify the signal.

The heat $Q(\boldsymbol{r}, t)$, produced by the absorption of light, generates the acoustic signal, which can be described by:

$$\nabla^2 p(\boldsymbol{r}, t) - \frac{1}{v_s^2} \frac{\partial^2 p(\boldsymbol{r}, t)}{\partial t^2} = -\frac{\varkappa - 1}{v_s^2} \frac{\partial Q(\boldsymbol{r}, t)}{\partial t}, \tag{12}$$

where $\boldsymbol{r}$ is the position, t is time, $p(\boldsymbol{r}, t) = p - p_0$ is the pressure of the excited sound wave, v_s is the velocity of sound and $\varkappa = c_p/c_V$ is the ratio of the specific heat constants c_p and c_V at constant pressure and volume, correspondingly. The

solution to the equation (12) can be written as

$$p(\boldsymbol{r}, t) = A_0(t) + \sum_n A_n(t) p_n(\boldsymbol{r}), \tag{13}$$

where A_n is the amplitude of the nth eigenmode component and p_n is the dimensionless eigenmode distribution. The solution is divided into two parts. Firstly, the constant part A_0, which has no dependence on the position inside the cell and secondly, the sum of the acoustical resonances.

The theory of these eigenmodes is thoroughly studied in Refs. [28; 55; 54] and several chamber designs has also been introduced to take the full advantages of these modes. However, at the same time most of the reachable PA signal is sacrificed by increasing the modulation frequency high enough to utilize these modes. One of the basic ideas enabled by the CEPAS is the operation on frequencies far below the first acoustic resonance. In this case, the sound wavelength is much larger than the dimensions of the cell and the average pressure inside the cavity will oscillate with the modulation pressure. [56]

2.3.2 IR Sources and their Modulation

At the early years of the photoacoustics, Bell used focused sun light as an IR source. With such broadband sources a narrow band-pass filter or a monochromator has to be used for the selectivity. A mechanical chopper is usually the only practical method for the intensity modulation of the incident light. However, in FTIR applications the modulation is performed with an interferometer.

In addition to broadband IR sources, also continuous wave or pulsed laser as well as semiconductor IR emitters (Paper VI) can be used. With laser sources, either intensity i.e. amplitude modulation (AM) or wavelength modulation (WM) is easily performed. Recent development in laser technology has made the mid-infrared region accessible which enables the excitation of strong fundamental vibrational transitions of molecules.

2.3.3 Condenser Microphone

The photoacoustic signal is usually measured with a condenser or electret microphone due to low-cost, simplicity and easy operation. [57] The structure, shown in Fig. 6, and the operation principle is shortly described in Paper I with the analysis of its disadvantages in PA detection.

The pressure sensor is a conducting, flexible membrane, which deforms due to the pressure variations in the surrounding gas. The membrane is mounted under a large radial tension and is separated from a fixed metal electrode by distance h_{m}. Thus, they form a condenser, whose capacitance C changes proportional to the pres-

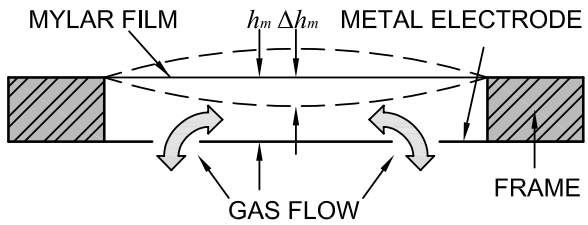

Figure 6. The operation principle of a condenser microphone (Paper III).

sure change Δp via the average displacement $\Delta h_{\mathrm{m}}/3$ i.e.

$$\Delta p \propto \Delta C = -\frac{\varepsilon A_{\mathrm{m}}}{3h_{\mathrm{m}}^2}\Delta h_{\mathrm{m}} \quad (\Delta h_{\mathrm{m}} \ll h_{\mathrm{m}}), \tag{14}$$

where A_{m} is the common area of the electrodes, and ε is the dielectric constant of the gas between the electrodes.

Limitations of the Condenser Microphones in PAS

The demands for a microphone in PAS differ from the specifications in more common applications. In music, for example the flat frequency response and low distortion are crucial. However, in PAS the acoustic signal should be measured as sensitively as possible at single frequency. According to the equation (14) the sensitivity of the condenser microphone can be improved by increasing A_{m} and decreasing h_{m}. However, there is a maximum, which cannot be further improved by this mean. This is due to so called 'breathing effect' i.e. due to viscous effects. [57] The air flow in and out of the gap between the electrodes requires energy, and therefore creates a strong damping on the film. According to the Paper I, this effect increases as A_{m} and h_{m} increases and decreases, respectively. The use of a more flexible material for the membrane in order to increase the amplitude increases the damping effect and decreases the dynamic range of the sensor.

A solution for the damping problem is to measure the movement of the film optically. [58] In this case, the measurement system will create less disturbance to the membrane than in the capacitance measurement, since the other electrode is no longer required. It is also possible to detect the maximum displacement Δh_m at the middle point of the membrane instead of the average displacement $\Delta h_{\mathrm{m}}/3$.

However, the use of a strained membrane as a vibrating element of the pressure sensor is not an optimal solution when the thermal stability is also important. This is due to the fact that the sensitivity of the membrane depends also on its tension, which is a strong function of the temperature. The response of the microphone on external pressure is also non-linear since the membrane has to stretch out radially under the pressure variations.

Noise

Due to their low sensitivities, condenser microphones are not able to detect almost any of the acoustical disturbances from outside of the closed cell. Only the vibrations at very low frequencies (usually below 20 Hz) has to be taken care of. Thus, the noise is mainly electrical and has no dependence on the frequency response of the microphone. Therefore, it is useful to amplify the photoacoustic signal by operating at some acoustical resonance frequency of the PA cell as described earlier.

2.3.4 The Normalized Sensitivity of a Photoacoustic Detector

The detection limits achieved with PA detectors depend not only on the sensitivity and noise level of the detector, but also on the line intensity and shape of the chosen absorption line, the power of the incident light and the measurement time. Therefore, the sensitivities of the PA detectors are usually compared by using a value called the normalized noise equivalent absorption coefficient (NNEA)[59]. It is determined as the minimum optical absorption coefficient α_{min} (signal = noise) multiplied by the optical excitation power P and divided by the square root of the detector bandwidth Δf (or multiplied by the square root of the measurement time t_m):

$$\text{NNEA} = \frac{\alpha_{\text{min}} P}{\sqrt{\Delta f}} = \alpha_{\text{min}} P \sqrt{t_m}. \tag{15}$$

Thus, the smaller the NNEA the better the sensitivity. Typically, the values for NNEA in laser based photoacoustic measurements have been in order of 10^{-8} – 10^{-9} $\text{cm}^{-1}\text{W}/\sqrt{\text{Hz}}$. [60; 61; 62]

3 Cantilever Microphone in Photoacoustic Spectroscopy

The replacement of the conventional microphone with a miniaturized cantilever in the early 2000s has proven to be a major developmental step in PAS. The cantilever enhanced photoacoustic spectroscopy (CEPAS), as the technique was later named, was at first time partly presented in reference [19] and more precisely in Paper I. This Chapter focuses on the cantilever microphone and the development of the physical model for the CEPAS. It gives the tools to understand the physics of the system, that has been shown to be essential for the further development of the technique. The major noise sources and the methods of compensating them are also described.

3.1 Setup for Cantilever Enhanced Photoacoustic Detection

The cantilever sensor changes the principles in the PA sample cell design. The main differences in a setup with a broadband source are (also schematically depicted in Figure 7):

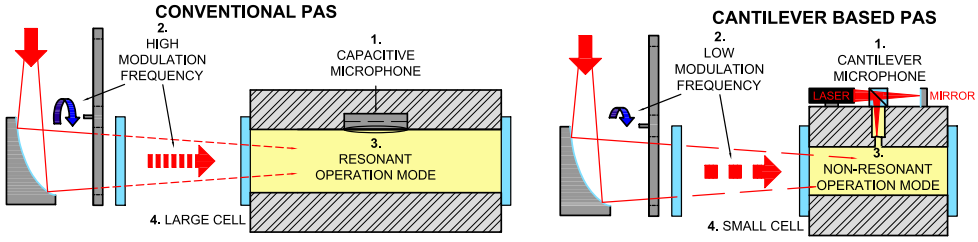

Figure 7. Comparison of the cantilever enhanced and conventional PA detection.

1. In CEPAS the condenser microphone is replaced by the cantilever microphone,
2. The modulation frequency in CEPAS is much lower than in conventional PAS,
3. In CEPAS acoustical resonances of the sample cell are not utilized, and
4. the sample cell can be miniaturized in CEPAS.

Figure 8 shows an example setup for CEPAS measurement using a laser source. The incident beam enters the PA cell, which is usually a small cylindrical tube. However, there is a larger balance cell that is connected to the PA cell only through the narrow gap of the cantilever. This balance cell is needed to prevent the gas spring (see section 3.2.2) to become too strong and further on for the compensation of the acceleration noise (section 3.3.2). A compact Michelson-type laser interferometer can easily be attached to the body of the detector.

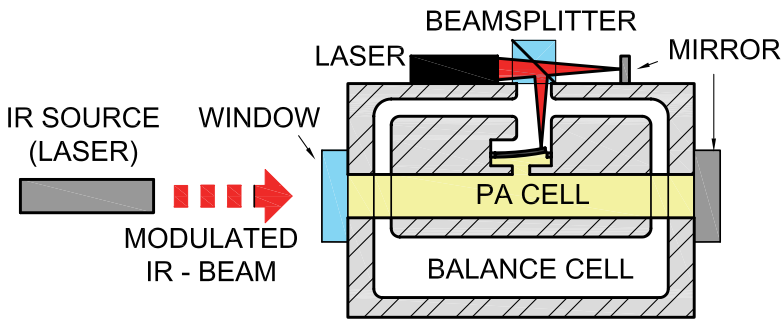

Figure 8. A practical setup for measurements with a cantilever-based PA detector (Paper V).

3.1.1 The Cantilever

The sensor in the cantilever microphone is a thin rectangular flexible bar as shown in Figure 9. It is made of silicon and its typical dimensions for width w and length l are few millimetres, and for thickness d from 5 to 10 μm.

The cantilever differs from the cantilevers used in atomic force microscopy (AFM) [35] not only by its dimensions but also due the fact that it is separated on three sides from the thicker frame with a narrow ($\Delta = 3$ to 10 μm) gap. Therefore, in PA setup shown in Figure 8 it acts like a door between the sample cell and a larger balance cell. The fabrication and characterization of the cantilever sensor is described in Ref. [63].

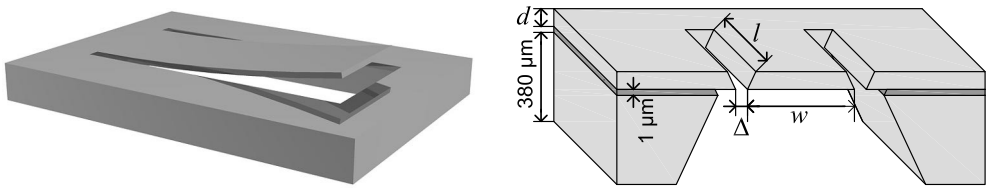

Figure 9. Silicon cantilever sensor.

3.1.2 Interferometric Displacement Measurement

The displacement of the cantilever is measured via a compact Michelson-type laser interferometer (Fig. 10). The laser beam is directed towards the free end of the cantilever and focused very close to it. Both arms of the interferometer are set to equal. The fixed mirror and four photodiodes d_i are arranged in such a way that there is a quarter of an interference fringe over each of them as shown in Fig. 11. Thus, the signals from the photodiodes, have a 90° phase difference between one another.

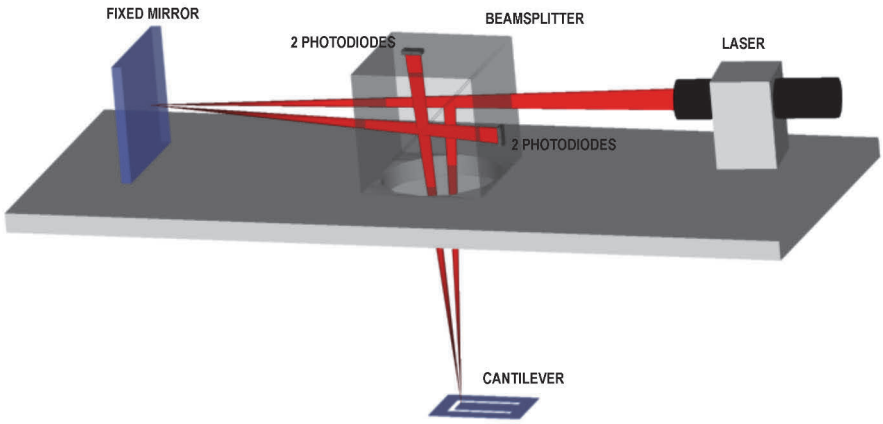

Figure 10. Interferometrically enhanced displacement measurement (Paper III).

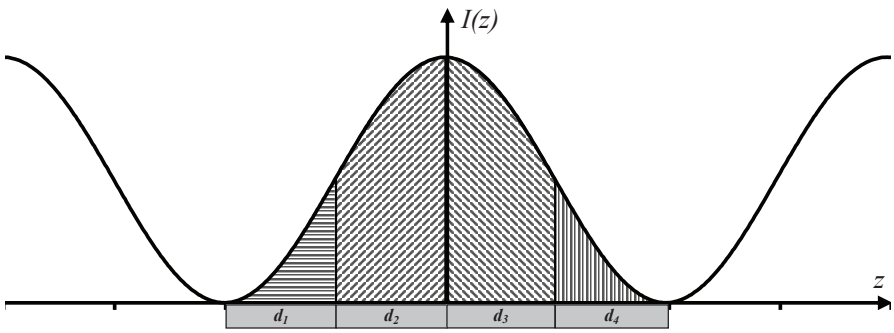

Figure 11. The interference fringe over the four photodiodes d_i.

The intensity distribution of the interference fringe over the diodes is

$$I(z) = \frac{1}{2}B(1+\cos\phi) = \frac{1}{2}B\left[1+\cos\left(4\pi\frac{x}{\lambda}\right)\right], \tag{16}$$

where B is the maximum intensity of the fringe, ϕ is the phase of the interferometer and λ is the wavelength of the laser used in the interferometer. The movement of the

fringe produces four orthogonal signals:

$$I_1 = B(1 + \cos\phi) \tag{17}$$

$$I_2 = B[1 + \cos(\phi + 90^\circ)] = B(1 + \sin\phi) \tag{18}$$

$$I_3 = B[1 + \cos(\phi + 180^\circ)] = B(1 - \cos\phi) \tag{19}$$

$$I_4 = B[1 + \cos(\phi + 270^\circ)] = B(1 - \sin\phi), \tag{20}$$

The signals are then converted to voltages U_i in an analog circuit. By subtracting the signals which have a 180° phase shift from each other we get

$$S_1 = U_1 - U_3 = B(1 + \cos\phi - 1 + \cos\phi) = 2B\cos\phi \tag{21}$$

$$S_2 = U_2 - U_4 = B(1 + \sin\phi - 1 + \sin\phi) = 2B\sin\phi. \tag{22}$$

A division leads to the tangent

$$\frac{S_2}{S_1} = \frac{2B\sin\phi}{2B\cos\phi} = \tan\phi, \tag{23}$$

and further on to the displacement of the cantilever

$$\Delta x = \frac{\lambda}{4\pi}\arctan\left(\frac{S_2}{S_1}\right). \tag{24}$$

Because of the division of the difference signals, the changes in the laser power do not disturb the measurement i.e. the phase of the interferometer does not depend on B. Thus, the displacement information is rather in the frequencies than the amplitudes of the carrier signals S_1 and S_2, which enables a huge dynamic range for the detection system.

If the phase ϕ of the interferometer changes over π, which corresponds to the displacement of $\lambda/4$ of the cantilever, the discontinuity of the tangent (Fig. 12) can be used to produce a $\lambda/4$ -counter. In that case the displacement of the cantilever is

$$\Delta x = \left(k + \frac{1}{2}\right)\frac{\lambda}{4} + \frac{\lambda}{4\pi}\arctan\left(\frac{S_2}{S_1}\right). \tag{25}$$

Thus, the interferometric measurement allows linear range from picometres up to millimetres producing greater dynamic range that can be achieved with any analogue electrical circuit.

3.2 Physical Model of the CEPAS

After the successfully demonstration of the CEPAS in Paper I, the development and optimization of the measurement setup demanded theoretical modelling of the physical phenomena related to the technique. The essential parts of the developed model, relating to the publications included in this thesis, are shortly presented here. A more comprehensive presentation can be found in a review article by Kuusela and Kauppinen. [56]

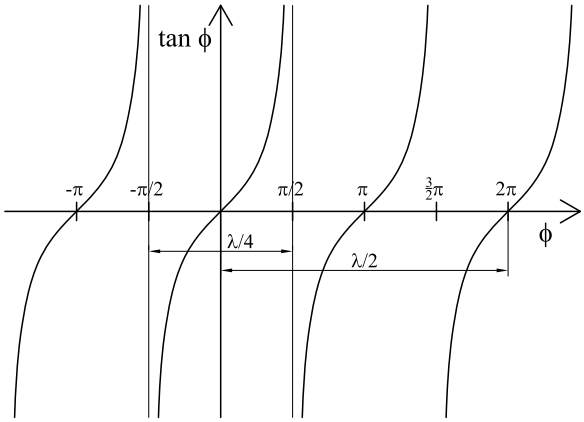

Figure 12. The discontinuity of the tangent as a $\lambda/4$ -counter.

3.2.1 Cantilever Dynamics and Point Mass Model

Bending of a Flexible Bar

By neglecting the effects of the frames and the surroundings of the cantilever (length l, width w and thickness d as in Fig. 13), we find that due an external force, it bends like a rectangular flexible bar, whose equation of motion is

$$E\frac{wd^3}{12}\frac{\partial^4 x(y,t)}{\partial y^4} + wd\rho_c\frac{\partial^2 x(y,t)}{\partial y^2} = 0, \tag{26}$$

where E is the Young's modulus, $x(y,t)$ is the displacement of the cantilever at y, t is the time and ρ_c is the density. [64] For (110) silicon E = 169 GPa and ρ_c = 2.33 g/cm^3.

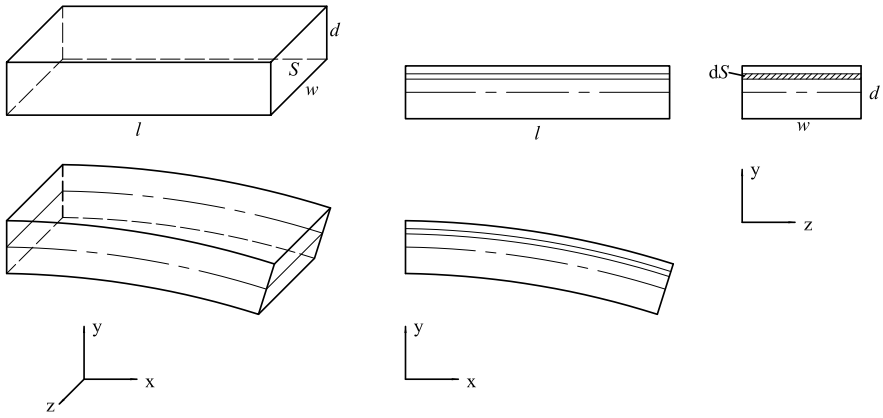

Figure 13. The bending of a flexible rectangular bar.

By using the boundary conditions that the other end of the cantilever is fixed and

the other is free, it is possible to calculate the allowed frequencies:

$$f_n = \frac{\mu_n^2}{2\pi l^2}\sqrt{\frac{Ed^2}{12\rho_c}}, \tag{27}$$

where $\mu_0 = 1.8751$, $\mu_1 = 4.6941$, $\mu_2 = 7.8548$, etc. (solutions of the equation $\cosh\mu\cos\mu = -1$). [65, p. 182] Thus, the fundamental resonance of the cantilever alone is at

$$\omega_{c,0} = 2\pi f_{c,0} = \frac{\mu_0^2}{l^2}\sqrt{\frac{Ed^2}{12\rho_c}}. \tag{28}$$

Point Mass Model of the Cantilever

In CEPAS, the modulation frequencies are well below the first resonance of the cantilever. Therefore, the full 3-dimensional structure model can be replaced with a simple 1-dimensional point of mass model using a harmonic oscillator like in Paper I. The equation of motion is

$$m\ddot{x} + \beta\dot{x} + kx = F_{ext}(t), \tag{29}$$

where the sinusoidal external force $F_{ext}(t) = F_0\cos(\omega t + \phi)$ acts on the whole area of the cantilever. In equation $x(t)$ is the cantilever's free end displacement from its equilibrium, m is the effective mass, β the damping factor, and k the effective spring constant of the system. As will be shown later, all of them depend not only on the properties of the cantilever but also on the environment, i.e., the dimensions and shape of the PA cell and the properties of the sample gas. This has been demonstrated in Paper V (Figure 14), where the experimental frequency responses using three sample gas mixtures were compared to complete theoretical model (see Ch 3.2.4).

The displacement $x(t)$ can be solved from the eq. (29) and its amplitude i.e. the frequency response is

$$A_0(\omega) = \frac{F_0}{m\sqrt{(\omega_0^2 - \omega^2)^2 + (\omega\beta/m)^2}}. \tag{30}$$

The resonance occurs at frequency $\omega_0 = 2\pi f_0 = \sqrt{\frac{k}{m}}$ and its height and width (i.e. the quality factor or Q-factor, given by $Q = \omega_0/\Delta\omega = m\omega_0/\beta$, where $\Delta\omega$ is the half-width of the resonance peak) depends on the damping factor β as shown in figure 15. At low frequencies ($\omega \ll \omega_0$) the response reduces to a constant value $F_0/m\omega_0^2$ and at high frequencies ($\omega \gg \omega_0$) it is degreasing as $F_0/m\omega^2$. However, the comparison of the responses in figures 14 and 15 shows that the model is still not adequate. The increase in signal at low frequencies and the changes in resonance frequencies are not explained by the point mass model alone.

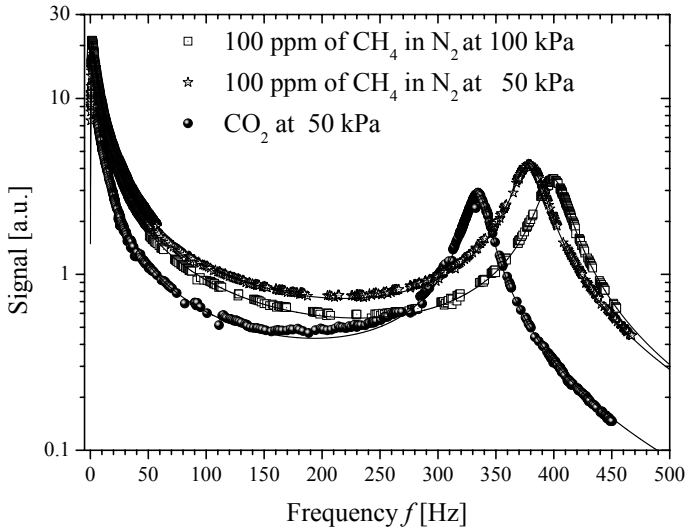

Figure 14. The influence of the sample gas and total pressure on the frequency response of the cantilever, presented in Paper V. The symbols present the measured data and the lines indicate the theoretical model.

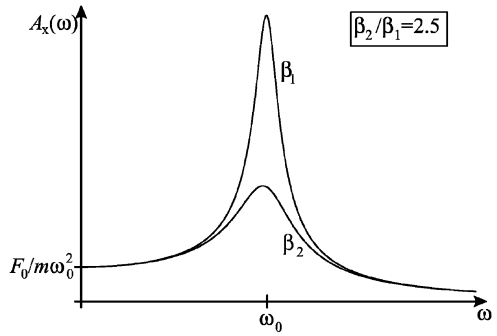

Figure 15. The frequency response of the forced harmonic oscillator with two different damping factors (Paper I).

Spring Constant of the Cantilever

The spring constant of a rectangular cantilever when the force acts on the free end is [64]

$$k_{\text{end}} = \frac{Ewd^3}{4l^3}. \tag{31}$$

If the force acts on the whole surface $A_{\text{c}} = wl$ of the cantilever, this has to be multiplied by 8/3 [66], i.e.,

$$k_{\text{c}} = \frac{2}{3}Ew\frac{d^3}{l^3}. \tag{32}$$

Effective Mass of the Cantilever

The effective mass in a point mass model is chosen such that the resonant frequency of the system $\omega_0 = \sqrt{(k/m)}$ is equal to the lowest flexural vibration frequency ω_0 from Eq. 27 by setting $n = 0$. Thus, by using equations (32) and (28) the effective mass of the cantilever alone[1] is

$$m_{\mathrm{c}}^{*} = \frac{k_{\mathrm{c}}}{\omega_1^2} = \frac{8}{\mu_0^4} wdl\rho_{\mathrm{c}} = \frac{8}{\mu_0^4} m_{\mathrm{c}} \approx 0.647 m_{\mathrm{c}}, \tag{33}$$

where the $m_{\mathrm{c}} = wdl\rho_{\mathrm{c}}$ is the whole mass of the cantilever. (Paper III)

3.2.2 Volume Effects of the PA Cell

If the dimensions of the gas cells are much smaller than the wavelength of the excited sound wave, the temperature T, the total pressure p, and the density of the gas have constant values without any dependence on the location inside the sample cell. Therefore, we can use the equation of the state of an ideal gas

$$pV = nRT \qquad \text{or} \qquad \frac{\mathrm{d}p}{p} + \frac{\mathrm{d}V}{V} = \frac{\mathrm{d}T}{T}, \tag{34}$$

where n is the number of the moles and R is the universal gas constant. By substituting the temperature change $\mathrm{d}T$ from the first law of thermodynamics

$$\mathrm{d}Q = \mathrm{d}U + \mathrm{d}W = nC_V \mathrm{d}T + p\mathrm{d}V, \tag{35}$$

to Eq. (34) we get

$$\frac{\mathrm{d}p}{p} + \varkappa \frac{\mathrm{d}V}{V} = \frac{(\varkappa - 1)\mathrm{d}Q}{pV}. \tag{36}$$

In Eq. (35) Q is the heat going into the gas, U is the internal energy of the gas and W is the work done by the gas. The specific heat ratio $\varkappa$ is given by

$$\varkappa = \frac{C_p}{C_V} = \frac{C_V + R}{C_V}, \tag{37}$$

where C_p and C_V are the molar heat capacities at constant pressure and volume, correspondingly.

Volume Changes of the Gas Chambers Due to Pressure Waves

When the pressure waves hit the cantilever, it starts to oscillate, which results in small volume changes in the gas chambers. The displacement $\mathrm{d}x$ of the cantilever's free end produced by the pressure change $\mathrm{d}p$ is

$$\mathrm{d}p = k_{\mathrm{c}} \mathrm{d}x / A_{\mathrm{c}}, \tag{38}$$

[1] in vacuum, when the effects of the surroundings are neglected

where $A_c = wl$ is the area of the cantilever. By approximating that, the cantilever bends in the shape of an arc of the circle the corresponding differential volume change dV is

$$dV = \frac{2}{5} A_c dx. \tag{39}$$

In Paper I, this was approximated as a triangle to $1/2 A_c dx$.

If we substitute the pressure and volume changes from equations (38) and (39) in Eq. (36) we have

$$\left(k_c + \frac{2\varkappa}{5} \frac{A_c^2 p}{V} \right) dx = \frac{A_c(\varkappa - 1) dQ}{V} = dF, \tag{40}$$

which links the external heating energy Q to the harmonic force. Further on, we get the total force acting on the cantilever by integrating the equation above

$$F_{ext}(t) = A_c \frac{(\varkappa - 1)}{V} \int \frac{dQ}{dt} dt. \tag{41}$$

The Effective Volume of the Gas Chambers

If the volume of the balance cell V_{Bal} (shown in Fig. 8) is not very large in comparison to the volume of the PA cell V_{PA}, the volume V is effective and determined with the relation

$$\frac{1}{V} = \frac{1}{V_{PA}} + \frac{1}{V_{Bal}}. \tag{42}$$

The Gas Spring

Equation (40) represents a harmonic force, but in addition to the spring constant of the cantilever, it has an additional part due to the volume changes of the chambers. This means that the gas volume itself acts like a gas springs $k_g(p)$, whose magnitude is inversely proportional to the effective volume of the chambers (see Eq. (42)) as

$$k_g(p) = \frac{2\varkappa A_c^2 p}{5V}. \tag{43}$$

Thus, if the effective volume is small, this part of the total spring constant

$$k = k_c + k_g(p) = \frac{2}{3} E w \frac{d^3}{l^3} + \frac{2\varkappa A_c^2 p}{5V} \tag{44}$$

becomes significant and should not be neglected.

The Effective Mass of the Gas

As the cantilever oscillates, it has to move the gas molecules around it. The influence of this effect to the system is directly proportional to the density of the gas. It can be modelled with an additional mass so that

$$m = m_c^* + m_{\mathrm{g}}^*(p) = \frac{8m_c}{\mu_0^4} + \frac{V^* M}{RT}p, \tag{45}$$

where M is the molar mass, R the universal gas constant and T temperature. The factor V^* depends on the size and shape of the cell.

Damping Coefficient

The total damping of the system will slightly increase with the density or pressure of the gas. Thus it can be modelled as a composition of the damping of the cantilever itself and the damping of the gas as

$$\beta = \beta_{\mathrm{c}} + \beta_{\mathrm{g}}(p). \tag{46}$$

The Resonance Frequency of the Cantilever in PA Setup

By substituting all the effects described above to the equation (30) we get the frequency response as

$$A_0(\omega) = \frac{A_{\mathrm{c}}(\varkappa - 1)\int \frac{\mathrm{d}Q}{\mathrm{d}t}\mathrm{d}t}{[m_{\mathrm{c}}^* + m_{\mathrm{g}}(p)]V\sqrt{(\omega_0^2 - \omega^2)^2 + \left[\omega\frac{\beta_{\mathrm{c}}+\beta_{\mathrm{g}}(p)}{m_{\mathrm{c}}^*+m_{\mathrm{g}}(p)}\right]^2}}, \tag{47}$$

where the resonance occurs at angular frequency

$$\omega_0^2 = \frac{k}{m} = \frac{k_{\mathrm{c}} + 2\varkappa A_{\mathrm{c}}^2 p/5V}{m_c + V^* M p/RT}. \tag{48}$$

The theoretical model was tested experimentally in Paper V by using three different gas mixtures as shown in Fig. 16. As predicted by the eg. 48, the resonance frequency of the cantilever in CEPAS setup depended on both the sample gas and its pressure. Further on, the additional mass $m_g(p)$ varied in the ratio of the molar masses of the investigated gas mixtures.

3.2.3 Heating and Cooling of the Sample Gas

Heating of the sample gas

Absorption of light produces heat into the sample gas and the thermal conduction through the walls of the cell acts as a heat leak. This can be described by the heat

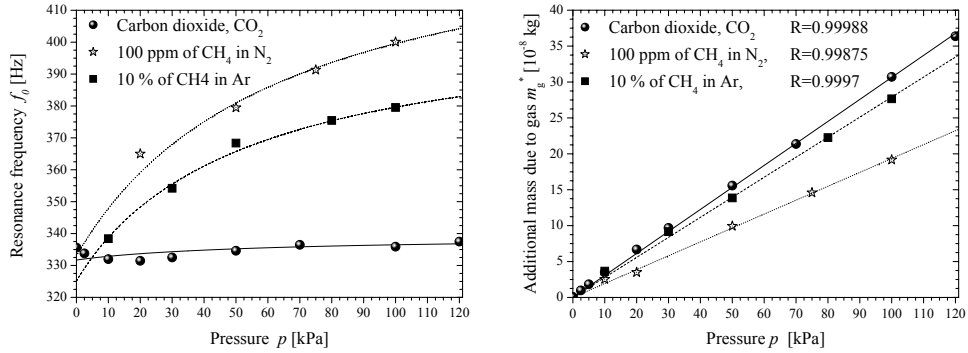

Figure 16. An example of the volume effects presented in Paper V. The resonance frequency of the cantilever in a CEPAS setup and the additional mass due to the sample gas depend on both the gas mixture and the total pressure.

energy rate

$$\frac{\mathrm{d}Q}{\mathrm{d}t} = \alpha_x c_x LP[1 - \cos(\omega t)] - G(T - T_0), \tag{49}$$

where P is the maximum power of the IR beam, G is the total thermal conductivity, T and T_0 are the temperature and initial temperature of the sample gas. [56]

In isochoric (isovolumetric) process, $\mathrm{d}Q = C_V \mathrm{d}T$ and we can derive the integral in Eg. 47 as

$$\int \frac{\mathrm{d}Q}{\mathrm{d}t}\mathrm{d}t = \int C_V \frac{\mathrm{d}T}{\mathrm{d}t}\mathrm{d}t = \frac{\alpha_x c_x LP\frac{C_V}{G}}{\sqrt{1 + \left(\omega\frac{C_V}{G}\right)^2}} \cos(\omega t + \varphi) \tag{50}$$

and further on the frequency response as

$$A^*(\omega) = \frac{A_c(\varkappa - 1)}{V} \frac{\alpha_x c_x LP}{m\sqrt{(\omega_0^2 - \omega^2)^2 + (\omega\beta/m)^2}} \frac{\tau_1}{\sqrt{1 + (\omega\tau_1)^2}}, \tag{51}$$

where the characteristic time constant is $\tau_1 = C_v/G$. In a cylindrical cell with radius r is the time constant is

$$\tau_1 = \frac{1}{2\pi f_1} = \frac{C_V}{G} \approx \frac{\rho_\mathrm{g} c_V r^2}{5.78K}, \tag{52}$$

where $\rho_\mathrm{g} = M/V_m = Mp/(RT)$, c_V and K are the density, specific heat capacity and the thermal conductivity of the sample gas, correspondingly. [56]

For practical purpose, Eg. 51 can be written by using frequencies f instead of angular frequencies and time constants as

$$A^*(f) = \frac{A_1(f)F}{4\pi^2 m\sqrt{4\pi^2(f_0^2 - f^2)^2 + (f\beta/m)^2}}, \tag{53}$$

where

$$F = \frac{A_{\mathrm{c}}(\varkappa - 1)\alpha_x c_x LP}{V} \tag{54}$$

and

$$A_1(f) = \frac{1}{f_1\sqrt{1 + (f/f_1)^2}}. \tag{55}$$

The term $A_1(f)$ acts like a low-pass filter with cut-off frequency f_1.

Gas Flow and Energy Transfer Through the Cantilever Frame Gap

The gas leakage from the PA cell to the balance cell through the narrow gap between the cantilever and its frame dampens the pressure variations. The heated molecules also transfer energy away from the sample cell even if there is no pressure difference between the cells. These mechanisms can be treated separately, but their effects on the response can be combined to one high-pass filter, whose transfer function is

$$A_2(f) = \frac{f/f_2}{\sqrt{1 + (f/f_2)^2}}. \tag{56}$$

The corresponding time constant is

$$\tau_2 = \frac{1}{2\pi^2 f_2} = \frac{4V}{3A_{\mathrm{gap}}}\sqrt{\frac{M}{RT}}, \tag{57}$$

where A_{gap} is the area of the gap. [56]

Relaxation Mechanism

The relaxation time from the absorption to heat generation depends on the complexity of the non-radiative relaxation pathways and the energy level structure of the excited molecules. However, the total relaxation process can be modelled using a low-pass filter

$$A_3(f) = \frac{1}{\sqrt{1 + (f/f_3)^2}}, \tag{58}$$

with one effective time constant $1/\tau_3 = 2\pi f_3$. Typically, τ_3 is less than 1 millisecond and is therefore not important in the normal operational frequencies (less than 100 Hz) of the cantilever-based systems.

3.2.4 The Frequency Response of the CEPAS System

The frequency response of the complete system $A_{\mathrm{tot}}(f)$ is a product of the responses described earlier, i.e.,

$$A_{\mathrm{tot}}(f) = \frac{A_1(f)A_2(f)A_3(f)F}{4\pi m\sqrt{4\pi^2(f_0^2 - f^2)^2 + (f\beta/m)^2}}. \tag{59}$$

This is illustrated in Fig. 17, where we see that the experimental data can be well fitted to Eq. (59).

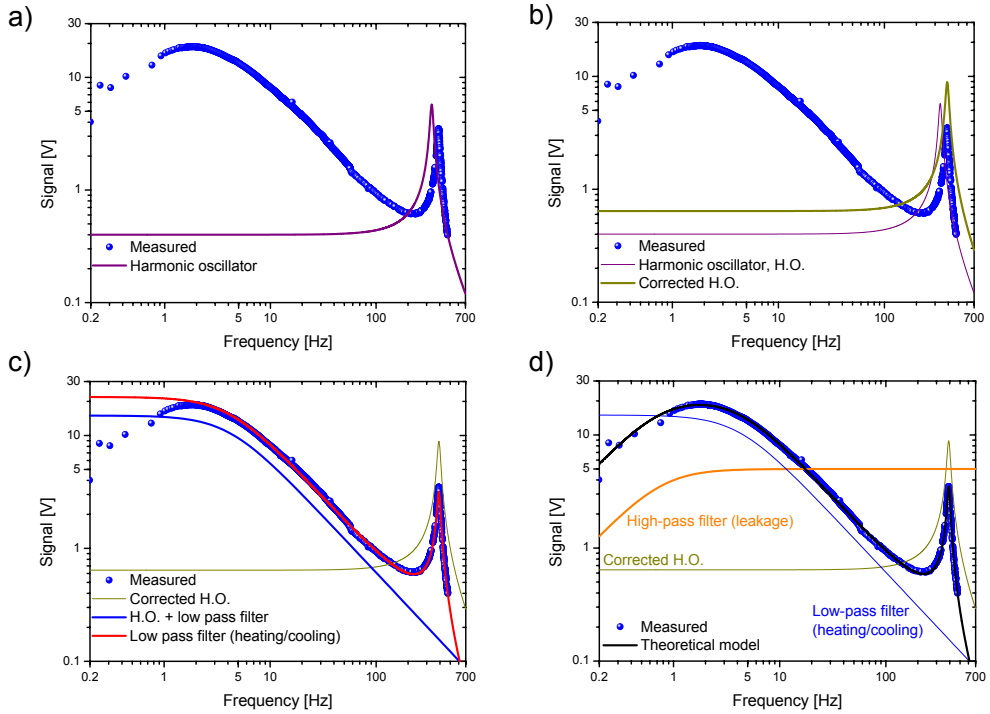

Figure 17. Modelling the frequency response. a) the measured frequency response and the theoretical curve based on harmonic oscillator. b) By correcting the theoretical model by volume effects, the counted resonance frequency corresponds to the measured one. c) The theoretical model corrected by low-pass filter $A_1(f)$ (eq. 55) and d) by $A_2(f)$ (eq. 56).

3.3 Noise

3.3.1 Noise Sources in CEPAS

In addition to the sensitivity, the performance of a detector in trace gas analysis depends also on the noise level i.e. the signal-to-noise ratio (SNR), which can be determined as

$$\mathrm{SNR}(\omega) = \frac{A_{\mathrm{tot}}(\omega)}{\text{Noise amplitude}}. \tag{60}$$

The main noise source in CEPAS is so called acceleration noise, described in Paper V. If it is eliminated the acoustical and the Brownian noise dominates the electrical noise, which is the only noise source that is not dependent on the frequency response of the system.

3.3.2 Acceleration Noise

Characteristics of Acceleration Noise

Acceleration noise is generated from the movements of the cantilever due to external disturbances like constructional vibrations acting on the system. Only the acceleration components, which are perpendicular to the cantilever surface, can make the cantilever bend and therefore produce noise. The corresponding SNR can be estimated by describing the external vibrations as a force

$$\Delta F = m_c \Delta a = \rho_c A_c d \Delta a = k \Delta x, \tag{61}$$

where Δa is the amplitude of the acceleration noise and Δx corresponding movement. [56] In the normal non-resonant operation mode of the CEPAS, we are interested in the frequency band below the resonance of the cantilever ($\omega \ll \omega_0$, SNR can be expressed as

$$\mathrm{SNR}_{\mathrm{accel}}(\omega) \approx \frac{(\varkappa - 1)\alpha_x c_x L P}{\omega V \rho_c d \Delta a}. \tag{62}$$

Thus, the use of more powerful laser sources operating at the wavelength region, where the strongest absorption lines of the investigated sample gas occur, increases the SNR ratio and enables lower detection limits. However, this does not actually improve the sensitivity of the detector itself. Thus, the most effective ways to improve the normalized sensitivity (NNEA) is to minimize the size of the sample cell V without decreasing the optical path length L. Actually, the major improvement in the sensitivity of CEPAS achieved in Paper IV based mostly on this. The NNEA can further be improved by enabling multiple passing of the laser beam through the sample cell.

However, the acceleration noise is not only generated from the acceleration of the cantilever itself due to its inertia, but also the acceleration of the gas inside the cell. Luckily, this latter effect can be used to compensate directly the noise amplitude Δa by using a proper geometrical design as shown in the next section.

3.3.3 The Compensation of the Acceleration Noise

The acceleration affects on the pressure inside both the PA and the balance cells linearly as shown in Fig. 18, i.e.,

$$p = p_0 - \rho_{\mathrm{g}} a x, \tag{63}$$

where p_0 is the original pressure and x the distance from the centre of the mass (CM) in a direction of the acceleration a. Only at the CM of each cell the acceleration does not influence the pressure. The effective (differential) pressure on the cantilever is then

$$p_{\mathrm{eff}} = \rho_{\mathrm{c}} d a + \rho_{\mathrm{g}} D a, \tag{64}$$

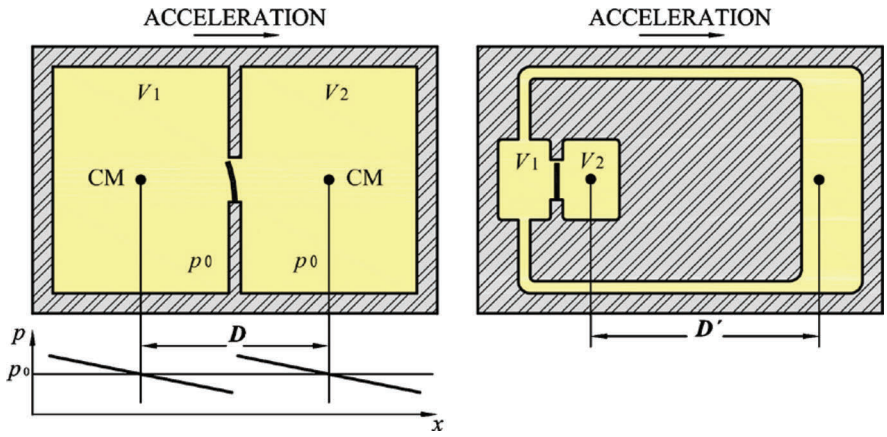

Figure 18. Acceleration noise compensation by a proper geometrical design (Paper V).

where ρ_c is the density of the cantilever and D is the distance between the CMs of the PA and balance cells. The first term describes the inertia of the cantilever and the second the movement of the gas, both acting on the same direction.

With the proper design of the balance cells, such in the right side of the Fig. 18, the effective pressure

$$p_{\text{eff}} = \rho_c da + \rho_g(-D')a, \tag{65}$$

can be set as zero by adjusting the distance between the CMs to $D' = \frac{\rho_c}{\rho_g} d$.

The compensation of the acceleration by using an adjusted balance cell was demonstrated in Paper V resulting in the maximum compensation factor of about 50 (Fig. 19).

Another compensation method of the acceleration noise, presented in Paper VI, is the use of two identical cantilevers. As shown in Fig. 20, the absorption of light inside the PA cell produces pressure waves that force the cantilevers to bend in the opposite directions. However, the acceleration of the detector bends the cantilevers in the same direction. Thus, the signals due to PA effect and the acceleration noise have a 180-degree phase difference. By the subtraction of these signals, the acceleration noise can be reduced.

3.3.4 Acoustical Noise

The term acoustical noise is used here to describe the unwanted pressure waves generated inside the PA cell due to external, usually high frequency mechanical vibrations. These vibrations can force some structures or other parts of the cell, such as valves and tubes, to vibrate and therefore act like a speaker. Similar to acceleration noise, the corresponding force for the noise amplitude Δp is

$$\Delta F = A_c \Delta p = k \Delta x. \tag{66}$$

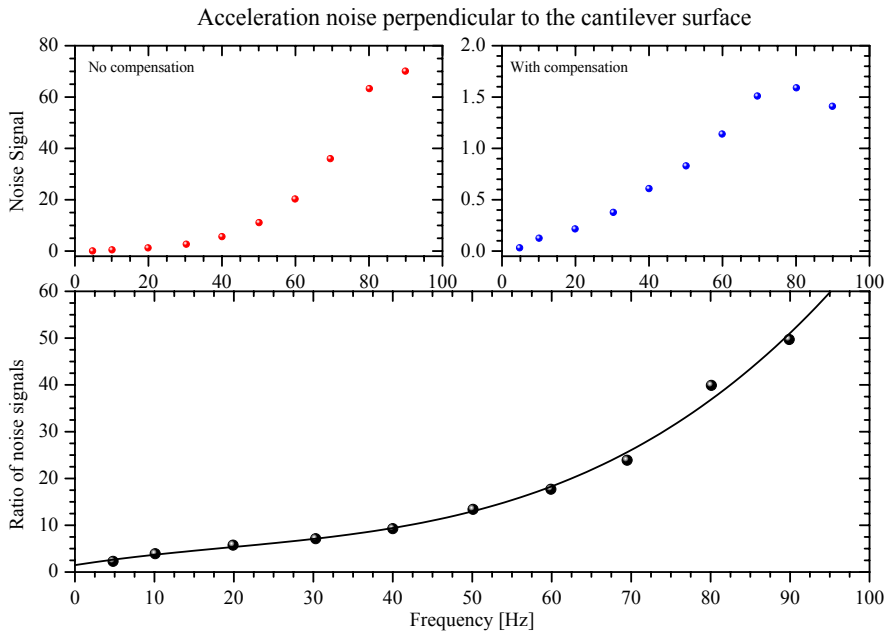

Figure 19. An experimental result in compensating the acceleration noise by geometrically adjusted balance cell (Paper V).

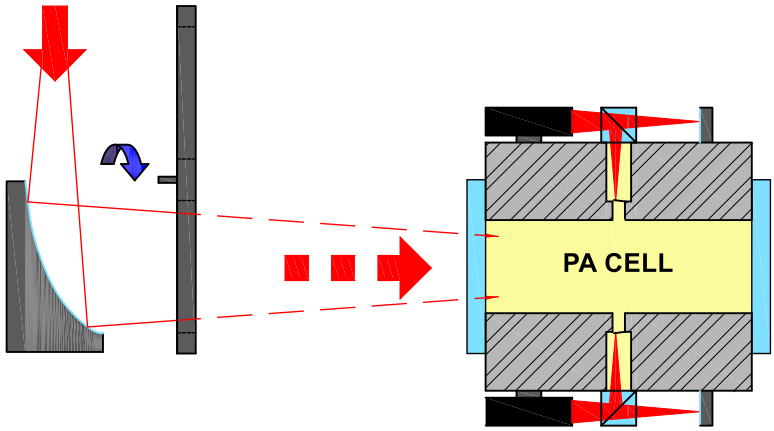

Figure 20. The use of two identical cantilevers in compensation of the acceleration noise.

The corresponding SNR at the low frequency region is

$$\mathrm{SNR}_{\mathrm{acoust}}(\omega) \approx \frac{(\varkappa - 1)\alpha_x c_x L P}{\omega V \Delta p}, \tag{67}$$

which is very similar to $\mathrm{SNR}_{\mathrm{accel}}$ in Eg. 61. [56]

3.3.5 Brownian Noise

The movement of the cantilever due to molecular collisions from the surrounding gas is called Brownian or thermal noise. [67; 68] Its magnitude can be estimated by adding a random force $F_{\text{th}}(t)$ due to thermal fluctuations to the external force $F_{\text{ext}}(t)$ [69] in the equation of motion (29) i.e.

$$m\ddot{x} + \beta\dot{x} + kx = F_{\text{ext}}(t) + F_{\text{th}}(t). \tag{68}$$

The detailed analysis is presented in [56] resulting in SNR as

$$\text{SNR}_{\text{Brown}}(\omega) = \frac{A_c(\varkappa - 1)\alpha_x c_x LP}{\omega V\sqrt{2k_B T k/\omega_0 Q t_m}} = \frac{A_c(\varkappa - 1)\alpha_x c_x LP}{\omega V\sqrt{2k_B T \beta/t_m}}. \tag{69}$$

As can be seen, the most effective ways to increase the SNR are to increase the Q-value of the resonance (or decrease the damping $\beta = \beta_c + \beta_g$) or to decrease the effective volume. The properties of the cantilever itself do not have remarkable effect on the SNR, since the increase of the cantilever area A_c will also increase the damping. In practise, the reduction of Brownian noise at the normal operation frequencies of the CEPAS can be made by using an external force to artificially increase the Q factor. The method has been used in AFM to increase the signal amplitude, but in this case it accumulates the thermal noise to the resonance peak. [56]

4 Main Results

The most straightforward measure of the results achieved in early years of CEPAS is the achieved normalized sensitivity NNEA in Paper IV. However, more important is all the work done to understand the physics of the system that enabled this result. As will be shown in Chapter 5, the developed model has proven to be precise and it continues to form the basis for future development work. This modelling of the system has already been described in Section 3.2 with the reported measurements confirming the model. In addition to sensitivity, also the noise and its compensation as well as the wide dynamic range have been shown to be crucial for the future applications. The demonstrated different measurement schemes showed the potential of the CEPAS in many fields of applications.

4.1 The Sensitivity of the CEPAS

4.1.1 Results with the First Prototype

The sensitivity of cantilever detection in trace gas PAS was at first time demonstrated in Paper I (Figure 21) by using the very first prototype of the detector shown in Figure 22. In those measurements, the PA cell was quite large and designed for broadband IR sources. The interferometer was located in a larger cell, separated from the PA cell by the cantilever. A self-made mechanical chopper was used to modulate the IR radiation from a relatively weak broadband black body source and a band-pass filter was used for the selectivity. As a preliminary result, a sub-ppb detection limit for methane was very promising.

A much more comparable result in contrast to other PA detection methods was achieved in Paper II by replacing the broadband IR source with a tunable diode laser (TDL). The fairly weak absorption line of carbon dioxide (CO_2) was selected for the experiment on the basis of laser availability and the same detector as in Paper I was used even though it was not optimized for the laser source. The achieved NNEA $4.6 \times 10^{-9}\mathrm{cm}^{-1}\mathrm{W}/\sqrt{\mathrm{Hz}}$ was among the best ever achieved in TDLPAS. In addition, the linearity of the detector in relation to the concentration of the sample gas and laser power was demonstrated. The further improvements achievable by optimizing the system for a laser source were discussed.

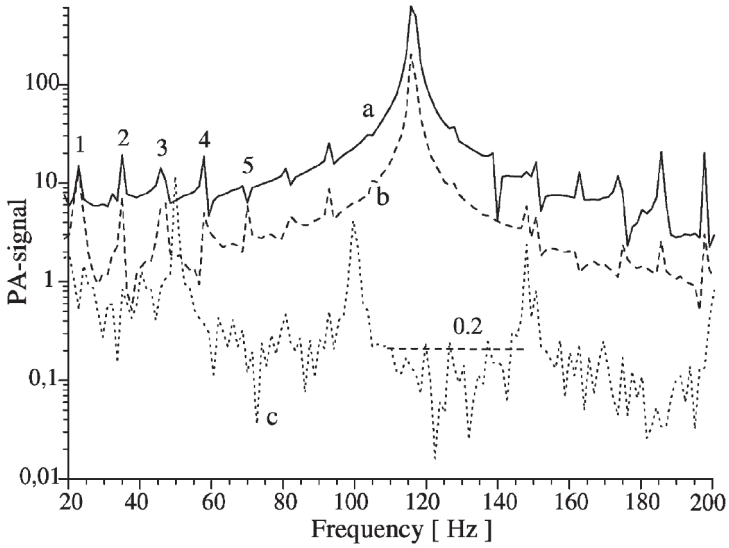

Figure 21. The amplitude of PA signal due to 10 ppm of methane at 118 Hz modulation frequency and the noise level presented in Paper I.

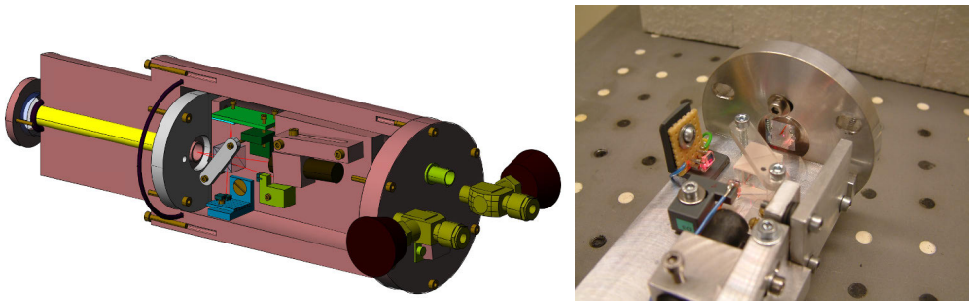

Figure 22. A 3D model and a photo of the first CEPAS prototype.

4.1.2 Setup for Laser Sources

The improvements proposed in Paper II were carried out in Paper IV by using a new detector optimized for laser sources (Fig. 24). The diameter of the PA cell was reduced from 10 to 3 mm increasing the average intensity entering the by factor 11. A new cantilever, allowing the use of lower modulation frequency, was located on the side of the PA cell, which was connected to a larger balance cell through the frame gap. These cells were sealed with the beamsplitter, which allowed the interferometer to be operated outside the gas cells. As a result of these optimizations, an improvement by factor 27 was achieved in comparison to previous results. The achieved NNEA of $1.7 \times 10^{-10}\mathrm{cm}^{-1}\mathrm{W}/\sqrt{\mathrm{Hz}}$ was the best ever reported in 2007 and after 16 years in 2023 still among the very best ones.

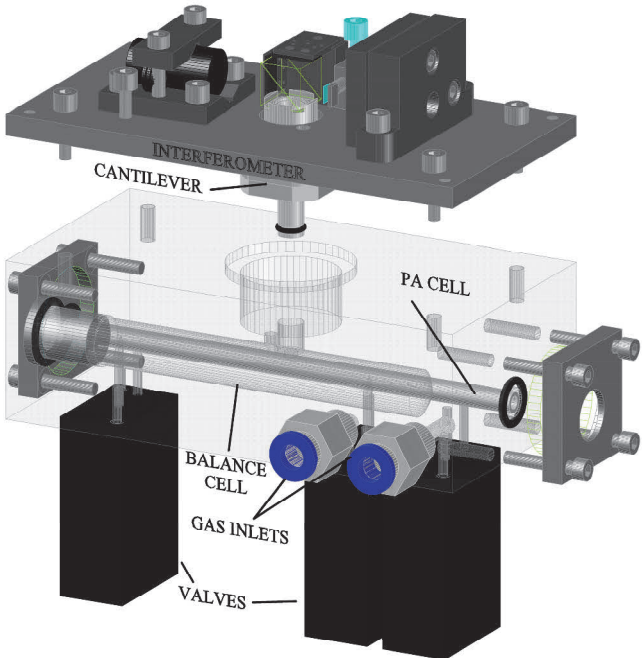

Figure 23. The first PA cell designed for laser sources (Paper V).

In certain applications, the high sensitivity of the CEPAS enables adequate detection limits even when using a very weak IR source as in Paper VI. A relatively low cost electrically modulated broadband infrared (EMBIR) source, having an emission spectrum close to a black body, was used with a dual cantilever detector shown in Figure 24.

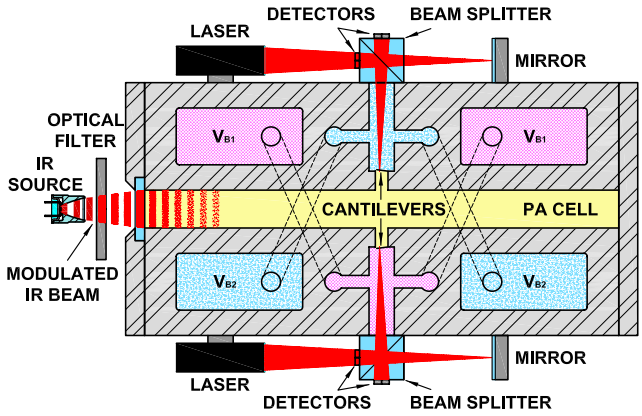

Figure 24. A dual cantilever detector used in Paper VI.

4.2 The Dynamic Range

The wide dynamic range of the system is based on the wide linear ranges of the cantilever movement and the Beer's law in interesting sample concentrations as well as the use of the interferometer as a counter-type detector of the cantilever displacement. The linearity of the PA signal as a function of the sample concentration and laser power has been shown in Papers II and III, depicted here in Figure 25.

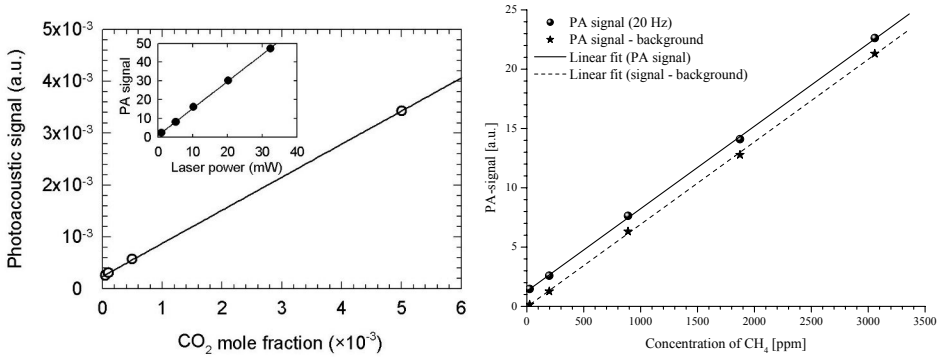

Figure 25. The linearity of the PA signal as a function of concentration and IR source power demonstrated in Papers II and III.

4.3 Measurement Schemes

The main results presented in this thesis are obtained by using either a broadband black-body radiator with a mechanical chopper and optical filter (Paper I) or a wavelength modulated laser source (Papers II and III). However, the non-resonant operation mode enables the use of CEPAS to gain the advances of the PA detection also in FTIR-devices, as shown in Paper V (Figure 26). Further on, due to the sensitivity of CEPAS, not only solid and liquid but also gas phase samples can be measured with enhanced sensitivity compared with the conventional PA-detectors. [70]

The differential method (Figure 27), that can be used to measure the trace gas level concentrations of the sample gas from open or flowing air has been demonstrated in Paper III. The main difference from other setups is that, the cantilever chamber is filled up with a gas to be detected. In case the sample gas does not contain the gas of interests, the PA signals from both sides of the cantilever are similar and cancel each other out. Whenever there is a gas of interest in the sample cell, part of incident IR radiation is absorbed in it resulting in the imbalance of PA signals in the cantilever chamber. The method is described in detail by Uotila [2] and as updated versions in Ref. [71; 72; 73].

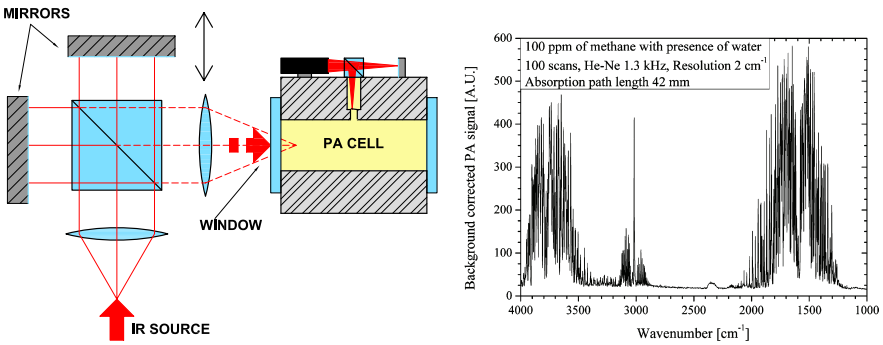

Figure 26. A schematic presentation for FTIR-CEPAS measurements and an example of a measured PA spectrum.

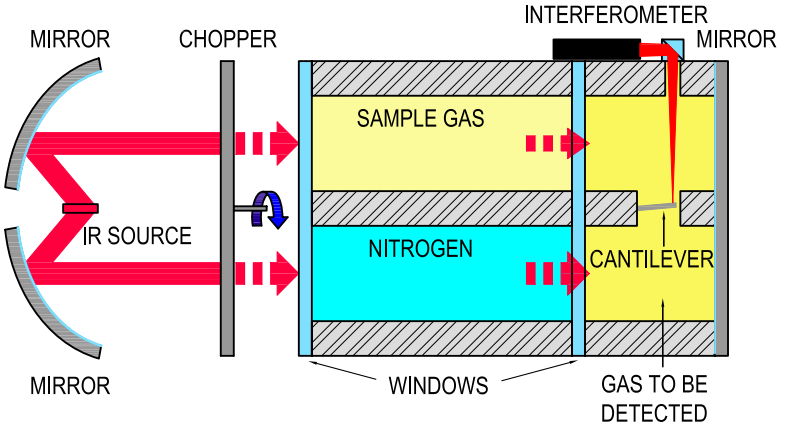

Figure 27. Setup for differential method (Paper III).

5 The Impact of CEPAS on Scientific Research

The impact of the presented work on scientific research is assessed through a retrospective study based on international scientific publications from the years 2007 to 2023. At first, the scientific citation databases are examined. The number of citations will be assessed in relation to other CEPAS publications, as these will strongly depend on the field of research. However, as a result of the commercialization of the CEPAS instruments, the direct references to the original publications do not give a complete picture of the impact. Since the commercialization has made it possible to use CEPAS in several research institutes and applications worldwide, these studies have also been considered in the impact assessment. As an essential part of the assessment, factors that have limited the use of technology in different applications have been identified.

In addition to the numbers of citations, the validity and usefulness of the results achieved by 2008 are also analysed. This bases partly on a qualitative evaluation on how the original publications have been referred to and how their results have been used further. An essential condition for an improvement of a technical device is to understand the physics behind it. Therefore, the achieved sensitivity has been used as a more exact measure of the accuracy of the developed physical model, which is the most significant result of this thesis. The results and success of subsequent efforts to improve sensitivity have also been assessed on the basis of a model developed.

The literature review, presented in the following paragraphs, is not complete but aims to be as comprehensive as possible. The publications set out in this chapter deal either directly with the method or have used a measuring instrument based on it.

5.1 Citation Analysis

5.1.1 The Number of Citations

To analyse the impact of a research, the number and type of citations to the Papers I – VI are studied at first by using two scientific citation databases (Table 1): ISI Web of Sciense (ISI-WoS) [74] and Elsevier API Scopus (Scopus)[75]. In evaluation of the total number of citations, also Google Scholar [76] and Research Gate [77] has been used. The values were retrieved from the databases on 12 April 2023.

Table 1. Total numbers of citations based on four citation databases (retrieved on 12 April 2023). The self-citations has been excluded from the ISI values and the Scopus values presented in brackets.

Publication	ISI Web of Science	Elsevier API Scopus	ResearchGate	Google Scholar
Paper I	106	121 (107)	130	165
Paper II	56	60 (50)	65	74
Paper III	73	70 (65)	77	100
Paper IV	77	68 (64)	73	100
Paper V	94	105 (104)	99	133
Paper VI	32	33 (33)	34	44
Total	438	457 (423)	478	616

The annual numbers of citations (retrieved from Scopus on 12 April 2023, self-citations of all authors excluded) by publication are presented graphically in Fig. 28. Since the availability of commercial analysers have a major influence on the amount of citations, a simple timeline of the CEPAS development and commercial product releases (Section 5.2.2) is given in Fig. 29. The total number of citations is 423, and they are distributed fairly evenly after 2013 (about 30 citations per year). From year to year, Papers I and V have been the most cited ones. The number of references to Paper I is understandable since it is the first publication describing the whole CEPAS method. Paper V outlined the physical model of the method and it has been annually cited more than Paper IV which demonstrated the extreme sensitivity of CEPAS. The reason for fewer citations of Paper IV might be that in spite of superior NNEA, the detection limit that was achieved was not that impressive, due to the quite weak absorption line that was used. For the wider public, the detection limit seems to be a clearer concept than the NNEA value. This is also reflected in studies by Tomberg et al. The sub-part-per-trillion level sensitivity achieved in Ref. [15] has gained

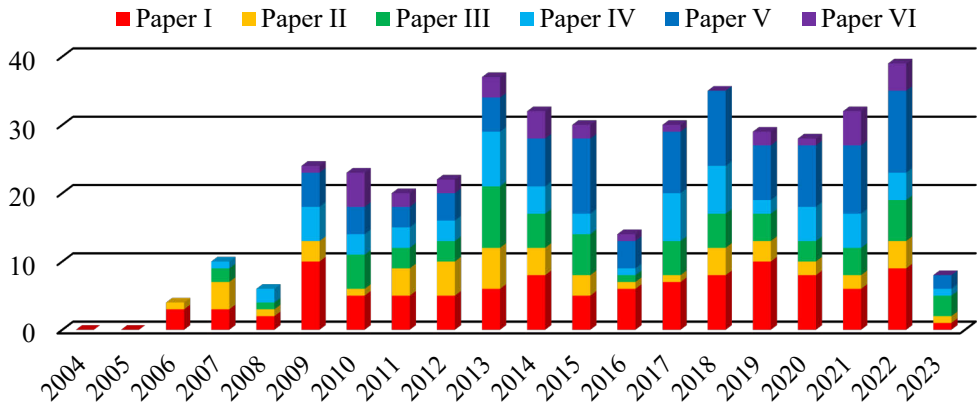

Figure 28. The number of annual citations to publications I – VI by Elsevier Scopus (12 April, 2023). The self-citations of all authors are excluded.

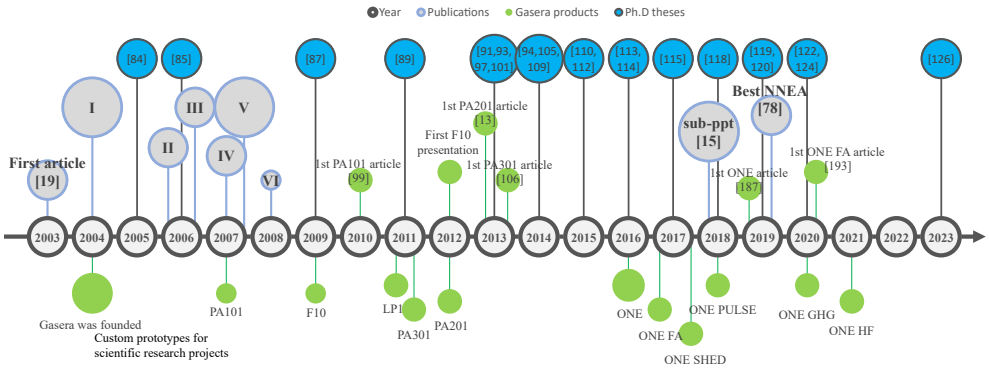

Figure 29. The CEPAS timeline with major publications including Papers I to VI, CEPAS related Ph.D theses and commercial product releases.

over four times more citations than the Ref. [78], where the normalized sensitivity (NNEA) is actually two orders of magnitude better but the detection limit is only at the sub-part-per-billion level.

As a comparison, the introduction of QEPAS in Ref. [43] has gained about three times (466 citations, Scopus) and the introduction of an all-optical PA spectrometer (AOPAS) in Ref. [79] about one third (42 citations) of the number of citations to the introduction of CEPAS in Paper I (107 citations). However, in such a small field of research, the size of the research group and its self-citations are also of great importance. For example, from the total of 629 references to the QEPAS[43], as much as 163 (26 %) were self-citations. The corresponding figures for CEPAS (Paper I) are 14/121 (12 %) and for AOPAS[79] 13/55 (24 %).

5.1.2 Citations in Relation to Other CEPAS Publications

For a comparison of the number of citations between different CEPAS related publications, they are presented in a citation or publication spiral in Fig. 30. The time from 2000 to 2023 is presented as increasing from the centre of the circle to its outer edge. The size of the circles describing individual publications depends on the number of citations. For the publications with over 30 citations, the number of citations is also shown together with the reference number. The different colours describe the four series of publications: blue circles represent the Papers I to VI, red ones the publications related to this thesis (author has contributed to them), green ones are publications where the CEPAS method itself was under study or development and finally, orange ones represent applications where CEPAS has been utilized. The number of citations were retrieved from ISI-WoS.

As shown, Papers I - VI are among the most cited CEPAS publications. However, the research field has an effect on the number of citations. Therefore, among the most

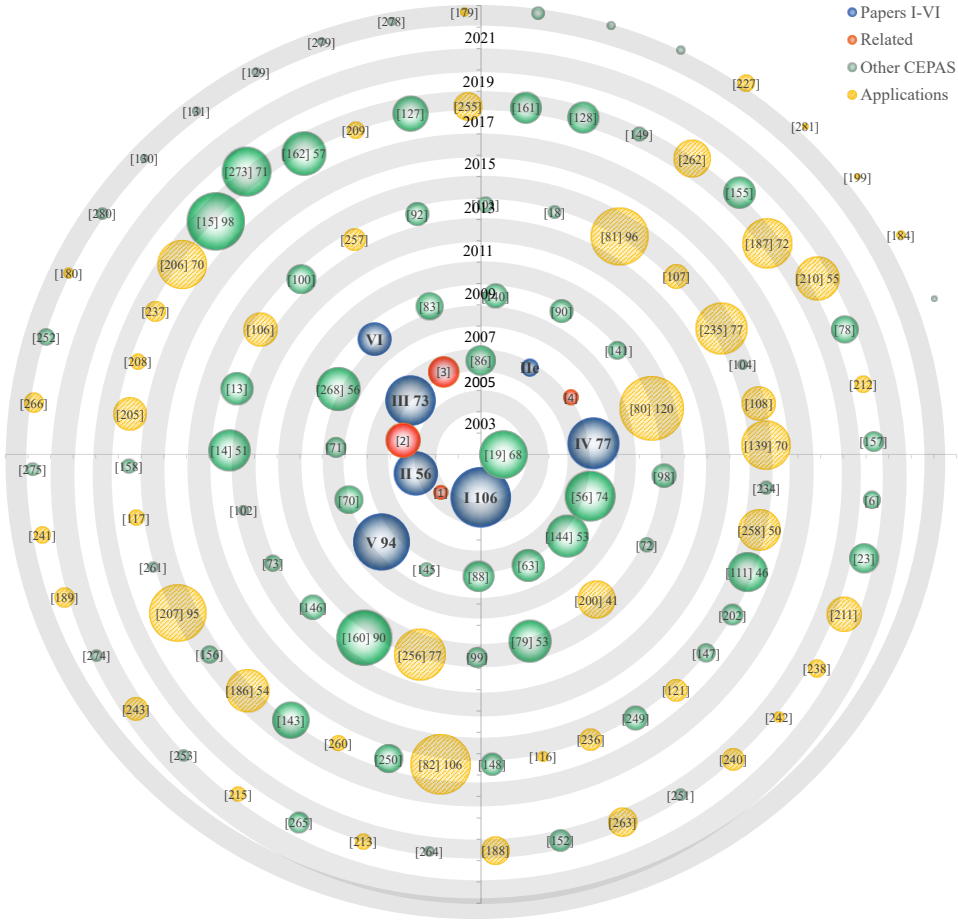

Figure 30. A citation spiral of the CEPAS-based publications from 2003 to 2023. The size of the circles describing individual publications are related to the number of citations (retrieved from ISI Wos on 12 April 2023).

cited publications in Fig. 30 there are applications utilizing CEPAS in another fields of research such as food quality assurance [80], detecting ethylene in plants [81] or carbon sequestration [82].

Actually, the publications citing the original papers I to VI can roughly be divided into three classes. The most interesting ones are those presented already in Fig. 30, where CEPAS is either used in a new application or in validating the previous results and those, where some properties of CEPAS are further developed [83]. After their publication, a great deal of these studies has been combined into Ph.D theses as shown in Table 2. Presented list is certainly incomplete, but it shows the change in the doctoral dissertations from the technical development of CEPAS to its use in applications in different fields. The subject matter of the dissertations will be

discussed in the following paragraphs.

Table 2. A list of CEPAS based Ph.D theses and related publications, known to author.

Year	Author	University	Ref.	Articles
2005	Laurila, T.	Tampere Univ. of Technology, Finland	[84]	Paper II, [3; 4]
Advances in Optical Diagnostic Based on Tunable Diode Laser Spectroscopy				
2006	Cattaneo, H.	Tampere Univ. of Technology, Finland	[85]	Paper II, [86]
Applications of Tunable Diode Lasers in Transmission and PAS				
2009	Uotila, J.	Univ. of Turku, Finland	[87]	[1; 2; 88; 71; 70]
Use of the Optical Cantilever Microphone in PAS				
2011	Saarela, J.	Tampere Univ. of Technology, Finland	[89]	[90]
Gas-Phase PAS, Advanced methods for PA Detection and Signal Processing				
2013	Sievilä, P.	Aalto Univ. Finland	[91]	[63; 92]
MEMS Cantilever Sensor for THz PA Chemical Sensing and Spectroscopy				
2013	Glauvitz, N. E.	Air Force Institute of Technology, USA	[93]	
Microfabrication technologies for single-crystal silicon sensors				
2014	Välikylä, T.	Univ. of Turku, Finland	[94]	[95; 96]
Michelson Interferometer With Porch Swing Bearing For Portable FTIR Spectrometer				
2013	Hirschmann, C.	Univ. of Oulu, Finland	[97]	[98; 99; 13; 100]
Cantilever-Enhanced PAS in the Analysis of Volatile Organic Compounds				
2013	Lehtinen, J.	Univ. of Turku, Finland	[101]	[102; 13; 103]
Detection of Illicit Drugs and Drug Precursors with Cantilever-Enhanced PAS				[18; 104]
2014	Pönni, R.	Aalto Univ., Finland	[105]	[106; 107; 108]
Changes in accessibility of cellulose for kraft pulps measured by deuterium exchange				
2014	Loria, M.	Univ. Degli Studi Di Palermom Italy	[109]	
Transport properties of drug precursor molecules in nanoporous polymers				
2015	Peltola, J.	Univ. of Helsinki, Finland	[110]	[14; 111]
Trace gas detection and high-precision spectroscopy in the mid-IR and visible wavelength regions				
2015	Rouxel, J.	Univ. de Reims Champagne-Ardenne	[112]	
Design and realization of miniaturized PA cells for trace gas detection				
2016	Aoust, G.	Univ. Paris Saclay, France	[113]	
Development of infrared sources and quartz resonators for PAS				
2016	Niinivaara, E.	Aalto Univ. Finland	[114]	
2-Dimensional Assembly of Cellulose-Based Materials				
2017	Brangule, A.	Riga Technical Univ. Latvia	[115]	[116; 117]
Application of FTIR Spectroscopy in Analysis of Synthesized and Natural Calcium Phosphate				
2018	Eduah, J. O.	Univ. of Ghana	[118]	
Phosphorus Reactions in Three Contrasting Soils Amended with Biochar				
2019	Karhu, J.	Univ. of Helsinki, Finland	[119]	[23]
Applications of Mid-infrared Frequency Combs for Linear and Nonlinear Vibrational Spectroscopy				
2019	Mikkonen, J.	Univ. Eastern Finland	[120]	[121]
Infrared Nuclear Magnetic Resonance Spectroscopic Methods for Salivary Analysis				
2020	Tomberg , T.	Univ. of Helsinki, Finland	[122]	[15; 78; 123]
Application of interferometry and CEPAS to background-free trace gas detection				
2020	Wikström, H.	Åbo Akademi Univ. Finland	[124]	[125]
Exploring Printed Drug Formulations for Inkjet and Stencil Printing: Pharmaceutical Sciences				
2023	Mikkonen, T.	Tampere Univ. Finland	[126]	[127; 128; 129]
Fourier Transform Photoacoustic Spectroscopy with Broadband lasers				[130; 131]

Another class of the publications consists of review papers, such as references

[42; 132; 133; 134; 135], or the literature studies, where the applicability of CEPAS to a certain application is considered or compared with a competing technique [136; 81; 137; 138]. Several of these literature assessments have later led to the realization of the technique for the application, sometimes even if the original evaluation was somewhat negative. [137; 139]

The third class of the referring publications are formed of those, where CEPAS is only mentioned [140; 141]. Most of those papers concerned a competing technique or presented PAS in a more generalized manner. [8; 142; 143]

5.2 The Validity of the Presented Results

To analyse the validity of the technology, a reliable measure for that is needed. Since an essential condition for an improvement of a technical device is to understand the physics behind it, the achieved sensitivity of the sensor is a good indicator of the accuracy of the developed physical model of the whole measurement system.

5.2.1 The Sensitivity of CEPAS

Before the introduction of CEPAS in 2004, the normalized sensitivities (NNEA) in conventional PAS were in order of 10^{-8} – 10^{-9}cm^{-1}W/$\sqrt{\text{Hz}}$. [60; 61] Typical values from several studies using conventional PAS are presented in Ref. [59]. At the best, the sub-ppb detection limits (or noise equivalent concentration, NEC) for individual gases had already been reached and they had been achieved by utilizing the acoustical resonances of the PA cells and using very high power lasers. The novel QEPAS-method presented at the beginning of the 21$^{\text{st}}$ century was at the same level of sensitivity as conventional PA methods, the best NNEA value was 7.2×10^{-9}cm^{-1}W/$\sqrt{\text{Hz}}$ [62].

CEPAS was introduced as using broadband IR source and the first NNEA value was achieved in 2006 by using a diode laser with PA cell not optimized for laser setup. However, it was already of the same magnitude as in the best previous studies (Paper II), as shown in Table 3. Another summary of sensitivities achieved in CEPAS in the detection of different gases is presented in a review by Fathy et al. [134]

After the commercialization of CEPAS detectors by Gasera Ltd. in 2005, the studies by several research groups around the world have proven the achieved results described in Chapter 4. In a study by Lindley et al. [144], the sensitivities of three PA setups were compared. With a non-optimized PA cell, the normalized sensitivity of the cantilever sensor was $\sim$100 $\times$ better than either the differential or single microphone cells. The NNEA of 2.2×10^{-9}cm^{-1}W/$\sqrt{\text{Hz}}$ (2σ noise) was in good agreement with the values reported by Laurila [3; 4] (1σ noise). In these studies, the results were obtained also by using an erbium-dobed fibre amplifiers (EDFA) to improve the detection limit (NEC) in TDLPAS. The results clearly demonstrate that

Table 3. A summary of the achieved sensitivities using CEPAS: NNEA (in $\times 10^{-9}$cm^{-1}W/$\sqrt{\text{Hz}}$), noise-equivalent concentrations (NEC) i.e. detection limits and the used laser power.

Year	Gas	NNEA	NEC [ppb]	Power [mW]	References
2006	carbon dioxide CO_2	4.6	7200	33	**Paper II**
2006	oxygen O_2	4.8	7200	30	[86]
2006	carbon dioxide CO_2	2.2	4600	30	[3; 4]
2006	carbon dioxide CO_2	2.2	230	600	[3; 4]
2007	ethylene C_2H_4	1.1	76000	0.01	[144]
2007	ethylene C_2H_4	2.3	1100	1.53	[144]
2007	carbon dioxide CO_2	0.17	1900	30	**Paper IV**
2007	carbon dioxide CO_2	0.11		2.1	[145]
2009	carbon dioxide CO_2	8.5	57000	30	[90]
2012	carbon monoxide CO	2.4	177000	2.93	[146]
2012	acetylene C_2H_2	4.1	1720	1.71	[146]
2012	methane CH_4	1.0	214300	0.81	[146]
2013	formaldehyde CH_2O	0.24	0.53	47	[13]
2013	formaldehyde CH_2O	0.20	0.43	47	[13]
2013	hydrogen cyanide HCN	1.8	0.190	500	[14]
2013	methane CH_4	1.8	0.065	600	[14]
2015	nitrogen dioxide NO_2	0.26	0.05	4700	[111]
2016	methyl cyanide CH_3CN	1.39		0.025	[147]
2016	methyl cyanide CH_3CN	0.43		0.025	[148]
2017	acetylene C_2H_2	0.77	15	23	[143]
2018	hydrogen fluoride HF	0.27	0.00065	950	[15]
2018	methanol CH_3OH	1.3	8.7	50	[149]
2018	methyl cyanide CH_3CN	1.7	1470	50	[149]
2018	formic acid CHOOH	6.0	620	50	[149]
2018	carbon dioxide CO_2	1.6	9300	50	[149]
2019	ammonia NH_3	2.6	3.2	1000	[6]
2019	acetylene C_2H_2	0.00175	0.24	7,5	[78]
2019	acetylene C_2H_2	1.3	24	12	[150]
2020	acetyleneC_2H_2	0.42	0.027	1000	[151]
2020	benzene C_6H_6	2.8	1	2.4	[152]
2022	methane CH_4	1.2	112	14.7	[153]
2023	tritiated water ^3H_2O	6.15	0.88	125	[154]

the reported NECs in Table 3 depend much more on available laser power than on the NNEA values. However, the NNEA values can be used to estimate the detection limits as the laser selection grows. An ultimate example of the linear relation of the PA signal to the incident laser power was demonstrated by Tomberg et al. in Ref. [15]. By utilizing a high power OPO, a strong absorption cross-section of hydrogen fluoride (HF), and high stability of experimental setup sub-ppt level sensitivity was achieved.

The theoretical model of the method was first used in practical implementation in 2007 (Paper IV). By optimizing the PA cell for laser sources an order of magnitude improvement in sensitivity was reached. This optimization included the reduction of sample cell size and the use of a cantilever that allowed lower modulation

frequency (compare with SNR equations 62 and 69 in Chapter 3.3). The achieved NNEA of $1.7 \times 10^{-10}\text{cm}^{-1}\text{W}/\sqrt{\text{Hz}}$ is still in 2023 one of the best ever reached, even though the guidelines for the further improvements were also given: the optimization of the pressure in the PA cell together with the properties of the laser wavelength modulation, reduction of the noise at low frequencies, and increasing the absorption path length by using mirrors, for instance. A well-consistent result was achieved by Parkes et al. [145] right after. Another indication of the accuracy of the model was found in a study [146] where three different gases were measured at the same time. The measurement was carried out using three different lasers simultaneously, each modulated at a different frequency, yielding to slightly different NNEA values.

Since 2007, several proposals have been presented to improve the sensitivity. The impact of different wavelength modulation waveforms on PA signal was demonstrated by Saarela et al. [90]. Compared with the conventionally used sinusoidal modulation, the triangular, shaped and quasi-square waves enhanced the PA signal by the factors of 1.12, 1.42 and 1.57. In studies [13] and [149] the wavelength modulation (WM) turned out to be slightly better than amplitude modulation (AM) and a new fabrication process for the cantilever presented in [92] was shown to improve the signal-to-noise ratio over 20 %. However, different materials for the cantilever, such as stainless steel [155], multilayer graphene [156; 157], mica [158; 157], silicon with piezoelectric coatings [159; 160] and piezoelectric polyvinylidene fluoride [161], were usually utilized for some other reason such as the low cost, chemical resistance and ease of the fabrication or miniaturization.

Instead of the interferometrical readout of the cantilever displacement, also optical beam deflection (OBM) in very low vacuum conditions is used [147]. In a miniaturized measurement setup, the cantilever was replaced with a micromirror attached to a free end of a cantilever beam and the deflection of the cantilever was detected via optical fibre interferometry [143]. However, these alterations as well as the utilization of the acoustical resonances of the PA cell [6] and together with the resonance of the cantilever [162; 151] did not lead to improvement of sensitivity. An up to date review of displacement detection methods used in CEPAS is presented in [133].

Finally in 2019, the sensitivity of CEPAS was remarkably improved by increasing the optical path length without increasing the size of the PA cell, as predicted by the model and presented in Paper IV. By using an optical power build-up cavity, Tomberg et al. [78] reported NNEA value of $1.75 \times 10^{-12}\text{cm}^{-1}\text{W}/\sqrt{\text{Hz}}$, that was two order of magnitude better than previous record in CEPAS as well as the best ever reported in PAS. The technique was named as cavity enhanced CEPAS, i.e. CE-CEPAS.

5.2.2 Development of CEPAS and Commercial Products

In several literature comparisons based mainly on original publications I – VI, repeated concern was expressed about the difficult adjustment, robustness and thermal stability of the displacement measurement based on Michelsson interferometer. [42; 161] Based on technical documents by Gasera Ltd.[163] and Ref. [12] the original Michelson type interferometer has been replaced by a more robust implication of the readout interferometer. As a major improvement to thermal stability, the light beam of the other arm of the interferometer is now reflected from the cantilever frame instead of a mirror located outside the balance cell. After the commercialization of the technology, its development is closely linked to the products released by Gasera Ltd. The release dates of the new measuring devices are already shown in Fig. 29 and their features will be briefly discussed next.

Accessories for FTIR spectrometers

The basis for the use of CEPAS as an FTIR accessory had already been presented in [70] and the first commercial product released by Gasera was the PA101 accessory to be installed on existing FTIR spectrometers for gas analysis. [164] It was intended to replace the conventional long path gas cell and the IR detector allowing low sample gas volumes (30 ml) and by its linearity the possibility to also measure wet gases. The product was promised a wide dynamic range and for most gases sub-ppm detection limits. The PA101 accessory was successfully used for example in analysis of volatile organic compounds (VOC) at elevated temperatures in [99].

The FTIR accessory PA301 for solid, liquid and semi-solid samples was introduced in 2011. [165] It can be used to measure samples with any shape or morphology with very minimal sample preparation. The sampling depth can also be varied in PAS and the measurement of dark samples such as bitumen and rubber are possible. PA301 has been widely utilized especially in environmental studies with soil samples, as presented later in section 5.3.3.

Early Products for Gas Analysis

In 2009 introduced multi-gas analyser F10 bases on the use of pulsed broadband IR sources and up to ten optical filters for target gases. [166] Selective, simultaneous measurements with sub-ppm detection limits up to nine gases were promised. More sensitive instruments for the gas analysis were the Analyser LP1 (2011) and the PA research gas cell PA201 (2012) designed for laboratory measurements. [167; 168] The simultaneous analysis of two gas components at Low-ppb level detection limit was enabled with LP1 by using two laser sources operating at different modulation frequencies. The stability of the device was improved by introducing the new readout

interferometer. The laboratory instrument PA201 can be tailored different types of light sources such as infrared distributed feedback laser (DFB), quantum cascade laser (QCL) and optical parametric oscillator (OPO).

Gasera One Platform

Together with PA201 and PA301, that are still on the market, the other currently available products are based on the Gasera ONE platform introduced in 2016. [169] The platform offers both single and multi-gas analysers [170; 171; 172; 173; 174] and it can be combined with different types of light sources.

5.3 Applications Utilizing CEPAS

5.3.1 Detection of Volatile Organic Compounds

One of the applications for trace gas analysis is the detection of VOCs, that could be dangerous to human health or the environment. Several VOCs usually exist at trace level concentrations in indoor air and at even lower concentrations in outdoor air. Thus, both the excellent sensitivity and selectivity are needed to detect and identify them. The higher concentrations may occur in industry.

In studies [98; 99; 13; 100] yielding to a Ph.D thesis by Hirschmann [97] several advantages of the CEPAS were utilized in the investigations of VOCs. The operation in the non-resonant mode was recognized as the most important feature in this application, since it enabled the use of several measurement setups and IR sources, including FTIR-PAS, OPO and QCL. The thermal stability of the cantilever, mentioned already in Paper I, enabled the measurements at gas temperatures up to 180 °C. In these studies the linearity of the CEPAS was successfully tested up to concentrations of 3 500 ppm (CH_4) and 17 500 ppm (CO_2). A total of 20 VOCs were analysed at ppm level using FTIR; benzene, toluene and xylene at ppb level using an OPO as a source and formaldehyde at sub-ppb level using QCL. The best NNEA achieved in these studies were $6.04 \times 10^{-10}\mathrm{cm}^{-1}\mathrm{W}/\sqrt{\mathrm{Hz}}$.

In some cases the selectivity of the CEPAS alone is not adequate. If there is a complex mixture of large VOC molecules, such as 2-ethylhexanol $C_8H_{18}O$, their spectra can be too complicated due to significant overlapping. However, the possibility to use very small sample volumes (sub-millilitres or even microlitres), enables the coupling of CEPAS with a gas chromatography (GC) capillary. Even though this has been successfully demonstrated by Tomberg et al. [123], they recognized the slow gas exchange and the static measurement problematic for adsorptive molecules.

In addition to the detection of the impurities in indoor air, the high sensitivity of CEPAS has been utilized to an increasing extent in the quality assurance measurements of photocatalytic degradation of formaldehyde and other VOCs. The aim is to

mineralize VOCs into non-toxic water (H_2O) and carbon dioxide (CO_2) using solar energy and different photocatalytic materials. In these studies, CEPAS has been used to estimate the oxidation rate by measuring in real time both the original VOC, such as benzene (C_6H_6) [175; 176], formaldehyde HCHO [177; 178; 179; 180; 181], acetaldehyde (C_2H_4O) [182], acetone (C_3H_6O) [183], or toluene $C_6H_5CH_3$ [184] and their end-products. Actually, at the moment this has shown to be the most active field of study utilizing the commercially available CEPAS detectors and only a small proportion of the related studies are presented as an example in the Table 4.

Table 4. Studies utilizing CEPAS in detection or photocatalytic degradation of VOCs. The used Gasera analyser is presented if known.

Year	Study	Analyser	Ref.
2011	Elevated temperature samples, detection of 18 VOCs	PA101	[99]
2013	Detection benzene, toluene and xylenes	PA201	[100]
2016	Sub-ppb detection of formaldehyde	PA201	[13]
2017	Multicomponent ppb-level air quality monitoring, several VOCs	PA201	[185]
2017	Methane catalytic combustion over Co, Ce, and Pd mixed oxides	PA101	[186]
2019	Catalytic oxidation of formaldehyde at room temperature	ONE	[187]
2020	Sub-ppb detection of benzene	PA201	[152]
2020	Oxidation of indoor formaldehyde at room temperature	ONE	[188]
2020	Broadband laser-based IR Detector for gas chromatography	PA201	[123]
2021	Structural differences in photocatalytic efficiency	ONE	[189]
2021	Photocatalytic minerazation of indoor VOCs CH_2O and C_7H_8	ONE	[190]
2021	Photocatalytic degradation of Acetone	ONE	[183]
2022	Catalytic oxidation of toluene	ONE	[191]
2022	Catalytic degradation of high concentration VOCs	ONE	[182]
2022	Oxidation process of VOC, formaldehyde	ONE	[178]
2022	Visible light photocatalysis of formaldehyde	ONE	[180]
2022	Visible light photocatalysis of formaldehyde	ONE	[181]
2022	Photodegration of formaldehyde	ONE	[179]
2023	Catalytic oxidation of formaldehyde	ONE	[177]
2023	Photocatalysis of toluene	ONE	[184]
2023	Photocatalytic process in removal of benzene series VOCs	ONE	[175]
2023	Benzene purification	ONE	[176]

5.3.2 Indoor Air Quality

Beside VOCs also other impurities can be real-time monitored from the indoor air. Several studies describing the measurements of impurities related to indoor air quality (IAQ) with CEPAS are presented in Table 5. In addition, several of the studies already presented in previous table are related to IAQ.

As shown in the Table 5 CEPAS has also been used to study ventilation performance and the transmission on airborne infections. Carbon dioxide CO_2, for instance, is a typical human based marker gas for the ventilation performance. Its concentration can therefore be used in evaluating as well as automatically adjusting

Table 5. Indoor air quality-related studies utilizing CEPAS.

Year	Study	Analyser	Ref.
2019	Airborne isolation Rooms to reduce infection rate	ONE	[192]
2020	Formaldehyde concentrations at university hospital	ONE FA	[193]
2020	Hospital-acquired infection risk, aerosol-transmissible pathogens	ONE Pulse	[194]
2022	Airborne infections, room air distribution	ONE	[195]
2022	Airborne infections, ventilated office rooms	ONE	[196]
2022	Pollutants from buildings through their ventilation system	ONE	[197]
2023	Calibration standard for CO_2 sensors at metro station	ONE	[198]
2023	Ventilation performance, SF_6 as tracer gas	ONE	[199]

the appropriate ventilation rate in dwellings, offices, schools and other occupied areas, such as metro stations as described in [198]. In turn, the occurrence of toxic carbon monoxide (CO) resulting from the combustion of imperfect substances may indicate a smouldering fire. Although simple and inexpensive meters are available for measuring these individual gases, the possibility of measuring them together with e.g. VOCs, particulate matter and aerosols may provide a better overall picture of indoor air pollution. A non-standard approach is presented in an ongoing project [197], where the ability of multi-component measurement of CEPAS is used to characterize and quantify pollutants leaving residential buildings through their ventilation systems.

As a result of the Covid-19 pandemic, there has been a significant increase in the study of airborne pathogens. In these studies, tracer gas measurements play a major role. For typical measurement, one or more breathable thermal manikins are placed in a laboratory room with controllable conditions and air ventilation. The transmission of the respiratory-generated airborne pathogens can be simulated by dosing a tracer gas, such as nitrous oxide (N_2O) or sulphur hexafluoride (SF_6), in the exhaled air of one of the manikins. In such a setup, not only the ventilation rate but also the room air distribution, were proven to be of major importance in cross-infection control. [195; 196]. In another study, tracer gas measurements have been used to assess the safety of isolation rooms. [192] However, in analysing the ventilation performance, air distribution and thermal comfort, tracer gas measurements such in Ref. [199] are commonly used.

5.3.3 Environmental Monitoring and Greenhouse Gases

Environmental studies, such as greenhouse gas (GHG) measurements, are another self-evident application of CEPAS. In these environmental applications both laser-based CEPAS and FTIR-CEPAS has been widely used in investigating samples in all phases: solid, liquid and gas. The majority of the studies have related either to the ability of soil and water to bind carbon or to the conditions under which GHGs are

released from them, as shown in Table 6.

The possibility of the in situ measurements of emissions from agricultural and animal feeding operations was questioned in the literature review in 2014. [137] However, already in the same year, the first such a measurement using FTIR-CEPAS was reported. [139] Actually since then, the improved sensitivity offered by the

Table 6. Studies related to environmental research.

Year	Study	Analyser	Ref.
2010	Nitrogen and carbon losses from dung storage		[200]
2011	Methods for detecting ethylene in plants		[81]
2014	Determination of soil organic carbon by FTIR-CEPAS	PA301	[139]
2015	Chemical composition of various organic waste products	PA301	[201]
2015	In situ Ammonia Concentration in Soil Headspace	PA101	[202]
2015	Biochemical methane potential of plant biomasses	PA301	[203]
2016	Straw and wood gasification biochar	PA301	[82]
2016	Changes in soil organic matter	PA301	[204]
2017	Non-invasive individual methane measurement in dairy cows	F10	[205]
2017	Amino sugars and lignin biomarkers in soil organic matter	PA301	[206]
2017	Soil organic carbon	PA301	[207]
2017	GHG emissions from soil, water filtration	PA301	[208]
2018	Retention of phosphorus in soil		[118]
2018	Emission from biomass burning	PA201	[149]
2018	Penicillium bilaiae to improve phosphorus bioavailability	PA301	[209]
2019	Soil organic matter in soil structural stability	PA301	[210]
2019	Methane measuerement methods in genetic evaluation of dairy Cattle	F10	[211]
2019	Ammonia emissions from dairy cow	F10	[212]
2020	Corn diet alteration on dairy cows manure and its emissions	ONE	[213]
2020	FTIR-PAS in characterization of environmental samples	PA301	[214]
2021	Prediction of Permanganate oxidizable carbon from soil samples	PA301	[215]
2021	CEPAS as a calibration standard in methane measurement	One Pulse	[216]
2021	Biochemical methane potential of urban organic waste	PA301	[217]
2022	GHG emissions from a sandy loam soil	ONE	[218]
2022	GHG emissions of the Bio-base fertilizers	ONE	[219]
2022	Methane emissions from beverage industry wastes	PA301	[220]
2022	Ammonia NH_3 emissions from dairy cow manure	ONE	[221]
2022	Dietary effects on manure gas emissions	ONE	[222]
2022	Phosporus availability on digestates	PA301	[223]
2022	Methane emission of dairy cow production	F10	[224]
2022	Soil chemistry, radon and other pollutants	PA301	[225]
2022	Pollutants from buildings through their ventilation system	ONE	[197]
2022	Sub-ppb detection of enriched benzene samples	PA201	[226]
2022	Electrocatalytic nitrate reduction from wastewater	ONE	[227]
2022	Effect of alley cropping on soil CO_2 and N_2O emissions	ONE	[228]
2023	Ammonia NH_3 emissions during manure storage	F10	[229]
2023	Emissions (N_2O, CH_4, CO_2, NH_3) from bioreactors	ONE	[230]
2023	Soil CO_2 and N_2O emission	ONE	[231]
2023	Seasonal variation of CO_2 in tropical lakes	ONE Pulse	[232]

CEPAS technology, has enabled the utilization of several advantages of FTIR-PAS in soil-related measurements, for instance. Some of these advantages are robustness, small sample size, easy sample preparation, and possibility of the depth profiling of the sample surface. In several applications, where solid samples have measured, the elimination of scattering effects and reflection issues by using PA approach has shown to be of importance. [201; 139] Further on, in a comparison of the three most widespread environmental FTIR techniques using solid and liquid samples, the FTIR-PAS provided more information than attenuated total reflectance (ATR-FTIR) and diffuse reflectance (DR-FTIR) FTIR-methods. FTIR-PAS also proved to be the most versatile technique, performing well for all material, and especially for dark and opaque samples (i.e. organic waste, biochar, and soil). [214] CEPAS has also shown to be reliable and practical in the studies of emissions from dairy cattle and their manure. [211; 212; 213; 221; 224]

Besides water, some of the most important greenhouse gases (GHG) are carbon dioxide (CO_2), methane (CH_4), and nitrous oxide (N_2O). As early as 2007, their emissions during the storage of animal manure in vegetable gardens were simultaneously measured by CEPAS. [200] For all of these GHGs, the detection limits achieved by CEPAS are small fractions of their atmospheric concentrations.

5.3.4 Pharmaceutics, Drugs and Medical Applications

The use of CEPAS in pharmaceutical sciences and industry has been considered quite soon after its introduction. Already in 2006, CEPAS were considered as a possible monitoring method for analysing the volatile products developed in fermentation processes in pharmaceutical industry. [233] The pharmaceutical and medical applications known to author, where CEPAS has been used, are presented in Table 7.

Starting from 2012, CEPAS-based trace gas and hair analysis has been used in the detection of illegal substances i.e. drugs and drug precursors. [101; 102; 103; 18] In gas-phase studies, ppb level detection limits were achieved for methyl benzoate, a hydrolysis product of cocaine hydrochloride, and benzyl methyl ketone, a precursor of amphetamine and methamphetamine. In pharmaceutics, solid-based CEPAS has also been used in the permeation studies of emulgels to skin layers [245; 246], drug diffusion and interaction with the skin tissues [244] as well as adsorption studies of medicinal substances to mesoporous micro and nanoparticles [235; 236; 239].

In medical diagnostics, the trace gas analysis of exhaled breath as a non-invasive and rapid technique started to show great potential in 1971, when gas chromatography was used to detect over 200 VOCs in human breath. [247] The main components in the mixture are nitrogen, oxygen, carbon dioxide, inert gases and water vapour. Beside them there are also thousands of VOCs, many of them relevant biomarkers for various diseases. [10] Detection limit of 100 ppt can be considered sufficient for almost any breath analysis application and ppb level for many of them [248; 9]. Sev-

Table 7. Pharmaceutics and Medical Applications.

Year	Study	Analyser	Ref.
2012	Drug detection	PA201	[102]
2013	Spectrosopic studies of Human hair, Nail and Saliva	PA301	[103]
2013	Cocaine Abuse identification from human hair samples	PA301	[18]
2014	Simulated IR spectra of drug precursors	Other	[234]
2014	Characterization of nanoparticles targeting breast cancer tumours	PA301	[235]
2016	Ibuprofen adsorption in mesoporous silicon microparticles	PA301	[236]
2016	Saliva biomarkers	PA301	[121]
2016	Simeltaneously identification of biomaterial surface and bacteria	PA301	[116]
2017	Identification of bacteria using FTIR-PAS	PA301	[117]
2017	Removal of *Escherichia coli* by hydrothermal zarbonization	PA301	[237]
2019	The characteristic features of the thermally hydrocarbonized surface of porous silicon	PA301	[238]
2019	Loading and release of anticancer drugs to silicon nanoparticles	PA301	[239]
2020	Characteristics of herbal medicin	PA301	[240]
2020	Stencil printing of orodispersible discs	PA301	[125]
2021	Silicon nanoparticles for applications in therapy and diagnostics	PA301	[241]
2021	Formalin safety in anatomic pathology	ONE FA	[242]
2021	Permetation studies in Photodynamic therapy of dermatological infections	PA301	[243]
2022	Drug diffusion and interaction with the skin tissues	PA301	[244]
2022	Emulgel permeation to human skin	PA301	[245]
2023	Emulgel permeation to deep skin layers of dairy cows	PA301	[246]

eral of these trace gases have already been measured by using conventional PAS [10] and the needed detection limits are well in the reach of CEPAS, where single breath collection to a small sampling volume is enabled and no pre-concentration steps in sample preparation are needed. Thus, exhaled breath analysis might be one of the most interesting and important future applications for CEPAS.

Biomarkers in saliva present another diagnostic tool and were studied in Ref. [121]. According to the related literature review in this study, FTIR spectroscopy has already been utilized in the saliva analysis of diabetes, physiological stress, and drug detection. Further on, FTIR methods have been utilized in plasma and serum analysis to classify or diagnose, for example, myocardial infarction, rheumatoid arthritis, Alzheimer's disease, dyslipidemia, leukaemia, bladder cancer, and ovarian cancer. Different components, such as glucose, lactate, protein, lipoproteins, and cholesterol, can also be determined from serum with FTIR. The ability of depth profiling has also been utilized in medical photoacoustic imaging (PAI). [22] Thus, medical diagnostics has huge potential for future applications of CEPAS.

5.3.5 Radioactive and Toxic Materials

When comparing different measurement methods, the concept of normalized sensitivity is important. Sometimes its significance may even be overemphasized, es-

pecially when developing a new method. In practical applications, however, the achieved detection limit is often more important. This is especially crucial when it comes to detecting toxic gases as in studies listed on Table 8.

Table 8. Studies related to radioactive and toxic materials.

Year	Study	Analyser	Ref.
2013	Detection of hydrogen cyanide (HCN), OPO source	beta	[14]
2015	Detection methyl cyanide	Other	[147]
2016	Detection of hydrogen sulfide (H_2S)	PA201	[249]
2016	Trace H_2S produced by SF_6 decomposition	PA201	[250]
2017	Detection of corrosive HCl and HBr gases using mica cantilever and OBD	Other	[158]
2019	FTIR-spectra of radiocarbon methane $^{14}CH_4$	PA201	[23]
2020	High resolution measurement of $^{14}CH_4$	PA201	[251]
2021	Radiocarbon dioxide detection	PA201	[252]
2022	Radon ^{226}Ra	PA301	[225]
2022	Detection of gaseous nerve agent simulants	PA201	[131]
2023	Detection of tritiated water (HTO)	PA201	[154]

In PAS, the low detection limits are not achievable only by using a sensitive PA sensor. The selection of the light source in relation to the absorption line strengths of the gas of interest, has also to be considered. For example, the use of a continuous-wave OPO operating in the mid-IR wavelength region that is optimal for molecular spectroscopy, enabled the detection of hydrogen cyanide (HCN) at the noise equivalent detection limit of 190 ppt in a 1 s measurement. [14] In Ref. [147] terahertz radiation was used to record the spectral data of methyl cyanide (CH_3CN) under very low vacuum conditions. The detection of highly corrosive gases might also require high chemical resistance from the detector as in Ref. [158], where mica cantilevers were utilized in the detection of hydrogen chloride (HCl) and hydrogen bromide (HBr). Besides other toxic gases, extremely high sensitivity and real-time measurements from limited samples is needed in the detection of chemical warfare agents (CWA) such as nerve agents. This can be achieved for example by combining FTIR-CEPAS with supercontinuum light source and multipass PA cell as shown in Refs. [131; 130].

Besides high sensitivity, suitability for measurements with limited sample volume is needed in the detection of radioactive samples such as radiocarbon methane $^{14}CH_4$ and dioxide $^{14}CO_2$. [23; 252] The possibility of the field measurements of the radiocarbon compounds is of interest due its important application in detecting emissions from nuclear sites, for instance. [152; 251] Its measurement has also applications in carbon dating. [23] Another major contributor to the total radioactive release in gaseous and liquid emissions from nuclear facilities is Tritium, denoted as ^3H or T. A CEPAS-based detector for gaseous tritiated water was presented in Ref. [154]

5.3.6 Industrial and Other Applications

Some uses of CEPAS based measurements in industrial and other applications, not mentioned in the previous chapters are listed on Tables 9 and 10. These applications range from clean room measurement [253] to climatisation of museum display cases [254] and from food chemistry [80; 255] to the detection of light absorbing particles [154].

Table 9. Examples of Industrial Applications of CEPAS.

Year	Study	Analyser	Ref.
2011	PA FTIR spectra of Au_{102}(*p*-MBA)$_{44}$	PA301	[256]
2013	Structural changes of cellulose in aqueous media	PA301	[106]
2013	Structural study of unsolvated [Cu(acac)$_2$]	PA301	[257]
2014	Ethylene detection in fruit supply chains	F10	[258]
2014	Manufacturing cellulosic products	PA301	[107]
2014	Accessibility of hydroxyl groups in birch kraft pulps	PA301	[108]
2015	Characterization of Cu_2O thin films	PA301	[259]
2015	Detection of nitrogen oxide NO_2	PA201	[111]
2016	Cellulose based materials, trimethylsilyl cellulose TMSC		[114]
2016	Hydrogen production from ammonia using plasma membrane reactor	F10	[260]
2017	Characterization of Amino/Azido Mixed-Linker Metal–Organic Frameworks	PA301	[261]
2018	Nickel catalyst for CO_2 methanation	PA301	[262]
2020	Crystalline phases of PVDF - poly(vinylidene fluoride)	PA301	[263]
2020	Trace CO detection	PA201	[264]
2021	Measurement of C_2H_2 to detect discharge faults of oil-immersed transformers	PA201	[265]
2021	Condition monitoring of transformers	ONE PULSE	[266]
2021	Real-time HCl measurements in cleanrooms	PA201	[253]
2023	Factors governing graphitization, FTIR-CEPAS	PA301	[267]

In several studies, the ability of measure solid samples without any preparation proved to be one of the main benefits in using CEPAS. [108; 107; 114] The surface characterization and depth profile measurements of transparent materials that were not possible with transmittance measurements could be easily investigated using PAS. [256; 259] The use of light absorbing material has also enabled the detection of electromagnetic radiation [277], and optical power [279].

5.4 Summary

Based on the analysis of the published attempts to further improve the CEPAS technique and its sensitivity, the model developed by 2008 has proved to be very accurate and actually all the successful improvements to the sensitivity of the method have been based on the principles set out in the model. Also, the sensitivity achieved in 2007 (Paper IV) is still among the very best ever reported. The number of annual

Table 10. Other CEPAS related Applications.

Year	Study	Analyser	Ref.
2009	Pig meat quality, boar taint detection		[80]
2009	Mid-IR LED with PA gas detection	beta	[268]
2011	Methane pipeline leakages		[136]
2012	Ageing of polymeric/energetic materials	beta	[146]
2014	EC-QCL in CEPAS of solids	beta	[104]
2015	MEMS cantilever system for terahertz radiation detection		[147]
2016	Terahertz radiation detection		[148]
2016	PA response of gases to terahertz radiation		[269]
2017	All-optical detecting sensor		[143]
2017	Drying conditions on amorphous $Ca_3(PO_4)_2$	PA301	[270]
2018	Assessment of specific defects in roasted coffee	PA301	[255]
2018	Assessment of specific defects in roasted coffee	PA301	[271]
2018	Optical frequency comb PAS	PA201	[128]
2018	CEPAS in mid-IR using supercontinuum	PA201	[127]
2018	Characterization of nanowire for mid-IR plasmonics	PA301	[272]
2018	Fiber-optic Fabry-Perot interferometer based cantilever microphone		[155]
2018	White-light Fabry-Perot cantilever microphone		[273]
2019	Cavity-enhanced CEPAS, CE-CEPAS		[78]
2021	Two channel LED-based sub-ppb detection limit for NO_2		[274]
2021	PA characteristics of carbon-based IR absorbers	PA301	[275]
2021	Obsidian hydration dating	PA301	[276]
2021	Detection of electromagnetic radiation		[277]
2022	Detection of light absorbing particles	PA201	[7]
2022	Terahertz radiation detection		[278]
2022	Optical power detection with broad spectral coverage		[279]
2022	Enriched gaseous samples in CEPAS	PA201	[226]
2022	Characterization of nanostructured materials		[280]
2022	Noise coupling in FT photoacoustic spectrosopy	PA201	[129]
2022	Miniature multipass cell in supercontinuum based FTIR-CEPAS	PA201	[130]
2022	PA phase-controlled FTIR spectroscopy	PA201	[281]
2022	Passive climatisation of display cases using saturated salt solutions	ONE FA	[254]

references to original publications, in particular to paper V, has remained constant or even slightly increased, indicating that their content is still considered relevant.

As predicted in the early 2000s, rapidly developing laser technology has enabled both the use of more powerful lasers and the utilization of stronger absorption lines. This has lead to a significant reduction in the detection limits for different compounds and therefore enabled a wide range of new applications in several research fields from safety issues to indoor air quality, for instance. The high sensitivity, good thermal stability, the operation in non-resonant mode, small sample volume and the possibility to measure gas, liquid and solid samples without preparation have shown to be the key factors in various environmental, pharmaceutical and industrial applications.

Besides the cost of the detector, the most common limiting factors in the utilization of CEPAS have been the concerns about the complexity and thermal stability of the interferometric displacement measurement and the robustness of the whole detec-

tor. In some, usually literature based, studies the sensitivity of CEPAS has also been assessed as insufficient. However, part of these doubts have been due to a misunderstanding, where the effect of the incident laser power and the utilized absorption line strength on the published detection limit has not been considered.

In particular, after 2017, there is a clear change in the literature, where the focus was shifted from researching the technology itself to its applications. This strongly suggests that the once new and experimental method has been accepted as a functional and sensitive tool over the last two decades. However, there are research areas where traditional photoacoustic spectroscopy is widely used, but CEPAS is not commonly known. For example, in medicine the method is still in its infancy.

6 Conclusions

The introduction of the cantilever enhanced photoacoustic spectroscopy (CEPAS) and the development of its physical model during 2003 and 2008 has been presented in this thesis. On the basis of a retrospective literature analysis covering the first two decades of CEPAS, the achieved high sensitivity and the accuracy of the presented model has been proven by several research groups around the world. These results are still valid and relevant in further development of the method. During these years CEPAS has been an inspiration to numerous research projects, theses and new sensitive detection methods. It has also been successfully used in numerous applications in several fields of research.

As a non-invasive and zero background technique, PAS has several advantages over other spectroscopic methods. It can be used to measure limited volume samples in all phases without preparation and the signal is directly proportional to the incident power. Therefore, it has and will get the full benefit of the rapidly developing laser technology. Further on, the improved sensitivity achieved by the interferometrical cantilever microphone, has lead to the utilization of these advantages in several new fields of research. Especially, in FTIR-PAS the improved sensitivity despite the short optical path length has been used to overcome the linearity problems, for instance. Based on the literature, FTIR-CEPAS has been widely adapted as a functional technique in several environmental applications and in the characterization of surfaces in pharmaceutical and industrial applications.

In applications where the aim is to measure only one or a few previously known gases, laser-based PAS is a straightforward solution. Most actively it has been utilized in the IAQ related measurements of individual VOCs and in studies related to photocatalytic degradation of the harmful VOCs. However, multi-compound analysis or the entire FTIR spectrum with sufficient sensitivity, for example in buildings with indoor air problems, could provide valuable and comprehensive information in the future to detect and solve these problems. Another future area of interest could be medical applications, such as exhaled breath or saliva diagnostics as well as photoacoustic imaging, where conventional photoacoustics has already been used, but CEPAS technology has hardly even been tested.

Based on the retrospective part of this thesis it is legitimate to claim that the CEPAS method introduced almost two decades ago has already had and still has impact on a number of scientific fields worldwide. The method has already been

successfully used in numerous applications and has proved suitable for several new ones. However, the future importance of this method for both the scientific research and the society as a whole depends on applications where its use will become more widespread.

List of References

[1] J. Kauppinen, V. Koskinen, I. Kauppinen, and J. Uotila. Extremely sensitive CWA analyzer based on a novel optical pressure sensor in photoacoustic gas analysis. *Proc. SPIE*, 5617:115–127, 2004. ⟨https://doi.org/10.1117/12.578535⟩.

[2] J. Uotila, V. Koskinen, and J. Kauppinen. Selective differential photoacoustic method for trace gas analysis. *Vib. Spectrosc.*, 38(1-2):3–9, 2005. ⟨https://doi.org/10.1016/j.vibspec.2005.02.002⟩.

[3] T. Laurila, H. Cattaneo, T. Pöyhönen, V. Koskinen, J. Kauppinen, and R. Hernberg. Cantilever-based photoacoustic detection of carbon dioxide using a fiber-amplified diode laser. *Appl. Phys. B*, 83(2):285–288, 2006. ⟨https://doi.org/10.1007/s00340-005-2106-9⟩.

[4] T. Laurila, H. Cattaneo, T. Pöyhönen, V. Koskinen, J. Kauppinen, and R. Hernberg. Cantilever-based photoacoustic detection of carbon dioxide using a fiber-amplified diode laser, erratum. *Appl. Phys. B*, 83(4):669, 2006. ⟨https://doi.org/10.1007/s00340-006-2208-z⟩.

[5] S. Schilt, L. Thévenaz, M. Nicklès, L. Emmenecker, and C. Hüglin. Ammonia monitoring at trace level using photoacoustic spectroscopy in industrial and environmental applications. *Spectrochim. Acta. Part A*, 60(14):3259 – 3268, 2004. ⟨https://doi.org/10.1016/j.saa.2003.11.032⟩.

[6] M. Guo, K. Cheng, Z. Gong, and Q. Yu. Trace ammonia detection based on near-infrared fiber-optic cantilever-enhanced photoacoustic spectroscopy. *Photonic Sensors*, 9(12), 2019. ⟨https://doi.org/10.1007/s13320-019-0545-x⟩.

[7] J. Karhu, J. Kuula, A. Virkkula, H. Timonen, M. Vainio, and T. Hieta. Cantilever-enhanced photoacoustic measurement of light-absorbing particles. *Aerosol Sci. Technol.*, 56(1):92–100, 2022. ⟨https://doi.org/10.1080/02786826.2021.1998338⟩.

[8] M. W. Sigrist, B. Bartlome, D. Marinov, J. M. Rey, D. E. Vogler, and H. Wächter. Trace gas monitoring with infrared laser-based detection schemes. *Appl. Phys. B*, 90:289–300, 2008. ⟨https://doi.org/10.1007/s00340-007-2875-4⟩.

[9] D. C. Dumitras, M. Petrus, A-M. Bratu, and C. Popa. Applications of near infrared photoacoustic spectroscopy for analysis of human respiration: a review. *Molecules*, 25(7):1728, 2020. ⟨https://doi.org/10.3390/molecules25071728⟩.

[10] R. Selvaraj, N. J. Vasa, S. M. S. Nagendra, and B. Mizaikoff. Advances in mid-infrared spectroscopy-based sensing techniques for exhaled breath diagnostics. *Molecules*, 25(9):2227, 2020. ⟨https://doi.org/10.3390/molecules25092227⟩.

[11] J. Wang, W. Zhang, L. Li, and Q. Yu. Breath ammonia detection based on tunable fiber laser photoacoustic spectroscopy. *Appl. Phys. B*, 103(2):263–269, 2011. ⟨https://doi.org/10.1007/s00340-011-4550-z⟩.

[12] J. Lehtinen, V.-M. Kittilä, A. Karimaa, and I. Kauppinen. Trace-gas analysis with cantilever-enhanced photoacoustic spectroscopy. *American Laboratory*, 48(6):18–20, 2016.

[13] C. B. Hirschmann, J. Lehtinen, J. Uotila, S. Ojala, and R. L. Keiski. Sub-ppb detection of formaldehyde with cantilever enhanced photoacoustic spectroscopy using quantum cascade laser source. *Appl. Phys. B*, 111(4):603–610, 2013. ⟨https://doi.org/10.1007/s00340-013-5379-4⟩.

[14] J. Peltola, M. Vainio, T. Hieta, J. Uotila, S. Sinisalo, M. Metsälä, M. Siltanen, and L. Halonen. High sensitivity trace gas detection by cantilever-enhanced photoacoustic spectroscopy using

a mid-infrared continuous-wave optical parametric oscillator. *Opt. Exp.*, 21(8), 2013. ⟨https://doi.org/10.1364/OE.21.010240⟩.

[15] T. Tomberg, M. Vainio, T. Hieta, and L. Halonen. Sub-parts-per-trillion level sensitivity in trace gas detection by cantilever-enhanced photoacoustic spectroscopy. *Sci. Rep.*, 8(1848), 2018. ⟨https://doi.org/10.1038/s41598-018-20087-9⟩.

[16] J. S. Li, B. Yu, H. Fischer, W. Chen, and A. P. Yalin. Contributed review: Quantum cascade laser based photoacoustic detection of explosives. *Rev. Sci. Instrum.*, 86(031501), 2015. ⟨https://doi.org/10.1063/1.4916105⟩.

[17] L. S. Marcus, E. L. Holthoff, and P. M. Pellegrino. Standoff photoacoustic spectroscopy of explosives. *Appl. Spectrosc.*, 71(5):833–838, 2017. ⟨https://doi.org/10.1177/0003702816654168⟩.

[18] J. Lehtinen, C. B. Hirschmann, R. L. Keiski, and T. Kuusela. Human hair in the identification of cocaine abuse with cantilever-enhanced photoacoustic spectroscopy and principal component analysis. *Appl. Spectrosc.*, 67(8):846–850, 2013. ⟨https://doi.org/10.1366/12-06904⟩.

[19] K. Wilcken and J. Kauppinen. Optimization of a microphone for photoacoustic spectroscopy. *Appl. Spectrosc.*, 57(9):1087–1092, 2003. ⟨https://doi.org/10.1366/00037020360695946⟩.

[20] J. F. McClelland, R. W. Jones, and S. Luo. Practical analysis of polymers with depth varying compositions using fourier transform infrared photoacoustic spectroscopy. *Rev. Sci. Instrum.*, 74 (1):285 – 290, 2003. ⟨https://doi.org/10.1063/1.1516244⟩.

[21] J. Yao and L. V. Wang. Sensitivity of photoacoustic microscopy. *Photoacoustics*, 2(2):87 – 101, 2014. ⟨https://doi.org/10.1016/j.pacs.2014.04.002⟩.

[22] I. Steinberg, D. M. Huland, O. Vermesh, H. E. Frostig, W. S. Tummers, and S. S. Gambhir. Photoacoustic clinical imaging. *Photoacoustics*, 14:77–98, 2019. ⟨https://doi.org/10.1016/j.pacs.2019.05.001⟩.

[23] J. Karhu, T. Tomberg, F. Senna Vieira, G. Genoud, V. Hänninen, M. Vainio, M. Metsälä, T. Hieta, S. Bell, and L. Halonen. Broadband photoacoustic spectroscopy of $^{14}CH_4$ with a high-power mid-infrared optical frequency comb. *Opt. Lett.*, 44(5):1142 – 1145, 2019. ⟨https://doi.org/10.1364/OL.44.001142⟩.

[24] A. Bell. On the production and reproduction of sound by light. *Am. J. Sci.*, (118):305–324, 1880. ⟨https://doi.org/10.2475/ajs.s3-20.118.305⟩.

[25] A. Bell. Upon the production of sound by radiant energy. *Philos. Mag.*, (71):510–528, 1881. ⟨https://doi.org/10.1080/14786448108627053⟩.

[26] J. Tyndal. Action of an intermittent beam of radiant heat upon gaseous matter. *Prog. R. Soc. Lond.*, 31(206):307–317, 1881. ⟨https://doi.org/10.1098/rspl.1880.0037⟩.

[27] W. C. Röntgen. On tones produced by the intermittent irradiation of a gas. *Philos. Mag.*, 11(71): 308, 1881. ⟨https://doi.org/10.1080/14786448108627021⟩.

[28] A. Rosencwaig. *Photoacoustics and Photoacoustic Spectroscopy*, volume 57 of *Chem. Anal.* John Wiley & Sons, 1980. ⟨https://doi.org/10.1002/ange.19820940341⟩.

[29] M. L. Viengerov. Eine neue methode der gasanalyse beruhend auf dem optisch-akustischen tyndall-röntgeneffekt. *Dokl. Akad. Nauk SSSR*, 19:687–688, 1938.

[30] K. F. Luft. Über eine neue methode der registrierenden gasanalyse mit hilfe der absorption ultraroter strahlen ohne spektrale zerlegung. *Z. Tech. Phys*, 24:97, 1943.

[31] F. J. M. Harren, G. Cotti, J. Oomens, and S. te Lintel Hekkert. *Photoacoustic Spectroscopy in Trace Gas Monitoring*. John Wiley & Sons Ltd., 2006. ISBN 9780470027318. ⟨https://doi.org/10.1002/9780470027318.a0718⟩.

[32] K. F. Luft, W. Schaefer, and G. Wiegleb. 50 jahre NDIR-gasanalyze. *TM. Tech. Mess.*, 60(10): 363–371, 1993. ⟨https://doi.org/10.1524/teme.1993.60.10.363⟩.

[33] G. A. West, J. J. Barret, D. R. Siebert, and K. V. Reddy. Photoacoustic spectroscopy. *Rev. Sci. Instrum.*, 54(7):797–817, 1983. ⟨https://doi.org/10.1063/1.1137483⟩.

[34] K. H. Michaelian. *Photoacoustic Infrared Spectroscopy*, volume 159 of *Chem. Anal.* John Wiley & Sons, Inc., 2003.

[35] G. Binnig, C. F. Quate, and Ch. Gerber. Atomic force microscopy. *Phys. Rev. Lett.*, 56(9): 930–940, 1986. ⟨https://doi.org/10.1103/PhysRevLett.56.930⟩.

[36] S. Alexander, L. Hellemans, O. Marti, J. Schneir, V. Elings, P. K. Hansma, M. Longmire, and J. Gurley. An atomic-resolution atomic-force microscope implemented using an optical lever. *J. Appl. Phys.*, 65(1):164–167, 1989. ⟨https://doi.org/10.1063/1.342563⟩.

[37] C. A. J. Putman, B. G. De Grooth, N. F. Van Hulst, and J. Greve. A detailed analysis of the optical beam deflection technique for use in atomic force microscopy. *J. Appl. Phys.*, 72(1): 6–12, 1992. ⟨https://doi.org/10.1063/1.352149⟩.

[38] G. Benedetto, R. Gavioso, and R. Spagnolo. Measurement of microphone membrane displacement with an optical beam deflection technique. *Rev. Sci. Instrum.*, 66(12):5563–5566, 1995. ⟨https://doi.org/10.1063/1.1146085⟩.

[39] M. H. de Paula, A. A. de Carvalho, C. A. Vinha, N. Cella, and H. Vargas. Optical microphone for photoacoustic spectroscopy. *J. Appl. Phys.*, 64(7):3722–3724, 1988. ⟨https://doi.org/10.1063/1.341416⟩.

[40] M. H. de Paula, C. A. Vinha, and R. G. Badini. High-sensitivity optical microphone for photoacoustics. *Rev. Sci. Instrum.*, 63(6):3487–3491, 1992. ⟨https://doi.org/10.1063/1.1143753⟩.

[41] S. M. Park and G. J. Diebold. Interferometric microphone for optoacoustic spectroscopy. *Rev. Sci. Instrum.*, 58(5):772–775, 1987. ⟨https://doi.org/10.1063/1.1139630⟩.

[42] J. Li, W. Chen, and B. Yu. Recent progress on infrared photoacoustic spectroscopy techniques. *Appl. Spectrosc. Rev.*, 46(6):440–471, 2011. ⟨https://doi.org/10.1080/05704928.2011.570835⟩.

[43] A. A. Kosterev, Y. A. Bakhirkin, R. F. Curl, and F. K. Tittel. Quartz-enhanced photoacoustic spectroscopy. *Opt. Lett.*, 27(21):1902 – 1904, 2002. ⟨https://doi.org/10.1364/OL.27.001902⟩.

[44] J. K. Kauppinen and M. R. Hollberg. *Spectrometers, Infrared*, volume 19. VCH Publishers, Inc., 1997.

[45] M. Šimečková, D. Jacquemart, L. S. Rothman, R. R. Gamache, and A. Goldman. Einstein A-coefficients and statistical weigths for molecular absorption transitions in the HITRAN database. *J. Quant. Spectrosc. Radiat. Transf.*, 98(1):130–155, 2006. ⟨https://doi.org/10.1016/j.jqsrt.2005.07.003⟩.

[46] L. S. Rothman, C. P. Rinsland, A. Goldman, S. T. Massie, D. P. Edwards, J.-M. Flaud, A. Perrin, C. Camy-Peyret, V. Dana, J.-Y. Mandin, J. Schroeder, A. McCann, R. R. Gamache, R. B. Wattson, K. Yoshino, K. V. Chance, K. W. Jucks, L. R. Brown, V. Nemtchinov, and P. Varanasi. The HITRAN molecular spectroscopic database and HAWKS (hitran atmosperic workstation): 1996 edition. *J. Quant. Spectrosc. Radiat. Transf.*, 60(5):665–710, 1998. ⟨https://doi.org/10.1016/S0022-4073(98)00078-8⟩.

[47] L. S. Rothman, D. Jacquemart, A. Barbe, D. Chris Benner, M. Birk, L. R. Brown, M. R. Carleer, C. Chackerian Jr., K. Chance, L. H. Coudert, V. Dana, V. M. Devi, J.-M. Flaud, R. R. Gamache, A. Goldman, J.-M. Hartmann, K. W. Jucks, A. G. Maki, J.-Y. Mandin, S. T. Massie, J. Orphal, A. Perrin, C. P. Rinsland, M. A. H. Smith, J. Tennyson, R. N. Tolchenov, R. A. Toth, J. Vander Auwera, P. Varanasi, and G. Wagner. The HITRAN 2004 molecular spectroscopic database. *J. Quant. Spectrosc. Radiat. Transf.*, 96(2):139–204, 2005. ⟨https://doi.org/10.1016/j.jqsrt.2004.10.008⟩.

[48] H. Margenau and W. W. Watson. Pressure effects on spectral lines. *Rev. Mod. Phys.*, 8(1):22 – 153, 1936. ⟨https://doi.org/10.1103/RevModPhys.8.22⟩.

[49] A. A. Michelson. On the broadening of spectral lines. *Astrophys. J.*, 2(4):251–263, 1895. ⟨https://doi.org/10.1086/140143⟩.

[50] G. Peach. Theory of the pressure broadening and shift of spectral lines. *Adv. Phys.*, 30(3): 367–474, 1981. ⟨https://doi.org/10.1080/00018738100101467⟩.

[51] M. D. Di Rosa and R. K. Hanson. Collision broadening and shift of NO $\gamma(0,0)$ absorption lines by O_2 and H_2O at high temperatures. *J. Quant. Spectrosc. Radiat. Transf.*, 52(5):515–529, 1994. ⟨https://doi.org/10.1016/0022-4073(94)90021-3⟩.

[52] C. Young. Calculation of the absorption coefficient for lines with combined Doppler and Lorentz broadening. *J. Quant. Spectrosc. Radiat. Transf.*, 5(3):549–552, 1965. ⟨https://doi.org/10.1016/0022-4073(65)90087-7⟩.

[53] B. H. Armstrong. Spectrum line profiles: the Voigt function. *J. Quant. Spectrosc. Radiat. Transf.*, 7:61–88, 1967. ⟨https://doi.org/10.1016/0022-4073(67)90057-X⟩.

[54] A. Miklós, P. Hess, and Z. Bozóki. Application of acoustic resonators in photoacoustic trace gas analysis and metrology. *Rev. Sci. Instrum.*, 72(4):1937–1955, 2001. ⟨https://doi.org/10.1063/1.1353198⟩.

[55] F. C. G. Bijnen, J. Reus, and F. J. M. Harren. Geometrical optimization of a longitudinal resonant photoacoustic cell for sensitive and fast trace gas detection. *Rev. Sci. Instrum.*, 67(8):2914–2923, 1995. ⟨https://doi.org/10.1063/1.1147072⟩.

[56] T. Kuusela and J. Kauppinen. Photoacoustic gas analysis using interferometric cantilever microphone. *Appl. Spectrosc. Rev.*, 42(5):443–474, 2007. ⟨https://doi.org/10.1080/00102200701421755⟩.

[57] I. G. Calasso and M. W. Sigrist. Selection criteria for microphones used in pulsed nonresonant gas-phase photoacoustics. *Rev. Sci. Instrum.*, 70(12):4569–4578, 1999. ⟨https://doi.org/10.1063/1.1150114⟩.

[58] N. Bilaniuk. Optical microphone transduction techniques. *Appl. Acoust.*, 50(1):35–63, 1997. ⟨https://doi.org/10.1016/S0003-682X(96)00034-5⟩.

[59] A. A. Kosterev, F. K. Tittel, D. V. Serebryakov, A. L. Malinovsky, and I. V. Morozov. Applications of quartz tuning forks in spectroscopic gas sensing. *Rev. Sci. Instrum.*, 76(4):043105, 2005. ⟨https://doi.org/10.1063/1.1884196⟩.

[60] M. E. Webber, M. Pushkarsky, and C.K.N. Patel. Fiber-amplifier-enhanced photoacoustic spectroscopy with near-infrared tunable diode lasers. *Appl. Opt.*, 42(12):2119–2126, 2003. ⟨https://doi.org/10.1364/AO.42.002119⟩.

[61] M. B. Pushkarsky, M. E. Webber, and C. K. N. Patel. Ultra-sensitive ambient ammonia detection using CO_2-laser-based photoacoustic spectroscopy. *Appl. Phys. B*, 77(4):381–385, 2003. ⟨https://doi.org/10.1007/s00340-003-1266-8⟩.

[62] A. A. Kosterev and F. K. Tittel. Ammonia detection by use of quartz-enhanced photoacoustic spectroscopy with a near-IR telecommunication diode laser. *Appl. Opt.*, 43(33):6213–6217, 2004. ⟨https://doi.org/10.1364/ao.43.006213⟩.

[63] P. Sievilä, V.-P. Rytkönen, O. Hahtela, N. Chekurov, J. Kauppinen, and I. Tittonen. Fabrication and characterization of an ultrasensitive acousto-optical cantilever. *J. Micromech. Microeng.*, 17(5):852–859, 2007. ⟨https://doi.org/10.1088/0960-1317/17/5/002⟩.

[64] U. Rabe, K. Janser, and W. Arnold. Vibrations of free and surface-coupled atomic force microscope cantilevers: Theory and experiment. *Rev. Sci. Instrum.*, 67(9):3281–3293, 1996. ⟨https://doi.org/10.1063/1.1147409⟩.

[65] P. M. Morse and K. U. Ingard. *Theoretical Acoustics*. Princeton University Press, 1986. ISBN 9780691024011.

[66] R. J. Stephenson. *Mechanics and Properties of Matter*. John Wiley & Sons, Inc., 1961.

[67] M. V. Salapaka, H. S. Berg, J. Lai, A. Majumbar, and E. McFarland. Multi-mode noise analysis of cantilevers for scanning probe microscopy. *J. Appl. Phys.*, 81(6):2480–2487, 1997. ⟨https://doi.org/10.1063/1.363955⟩.

[68] F. Gittes and C. F. Schmidt. Thermal noise limitations on micromechanical experiments. *Eur. Biophys. J*, 27(1):75–81, 1998. ⟨https://doi.org/10.1007/s002490050113⟩.

[69] S. Liang, D. Medich, D. M Czajkowsky, S. Sheng, J.-Y. Yuan, and Z. Shao. Thermal noise reduction of mechanical oscillators by actively controlled external dissipative forces. *Ultramicrosc.*, 84(1-2):119–125, 2000. ⟨https://doi.org/10.1016/S0304-3991(00)00039-5⟩.

[70] J. Uotila and J. Kauppinen. Fourier transform infrared measurement of solid-, liquid-, and gas-phase sample with a single photoacoustic cell. *Appl. Spectrosc.*, 62(6):655–660, 2008. ⟨https://doi.org/10.1366/000370208784658048⟩.

[71] J. Uotila. A new design of the differential photoacoustic gas detector combined with a cantilever microphone. *Eur. Phys. J. Special Topics*, 153(1):401–404, 2008. ⟨https://doi.org/10.1140/epjst/e2008-00471-y⟩.

[72] P. Karioja, K. Keränen, K. Kautio, J. Ollila, M. Heikkinen, I. Kauppinen, T. Kuusela, B. Matveev, M. E. McNie, R. M. Jenkins, and J. Palve. LTCC based differential photo acoustic gas cell for ppm gas sensing. *Proc. SPIE*, 7726, 2010. ⟨https://doi.org/10.1117/12.851854⟩.

[73] K. Keränen, J. Ollila, H. Saloniemi, B. Matveev, J. Raittila, A. Helle, I. Kauppinen, T. Kuusela, L. Pierno, P. Karioja, and M. Karppinen. Portable methane sensor demonstrator based on LTCC differential photo acoustic cell and silicon cantilever. *Procedia Eng.*, 47:1438–1441, 2012. ⟨https://doi.org/10.1016/j.proeng.2012.09.428⟩.

[74] Clarivate Analytics Institute for Scientific Information ISI. ISI Web of Science. ⟨https://clarivate.com/webofsciencegroup/solutions/web-of-science⟩, accessed April 12, 2023.

[75] Elsevier B.V. Scopus. ⟨https://www.scopus.com⟩, accessed April 12, 2023.

[76] Google. Google scholar. ⟨https://scholar.google.com⟩, accessed April 12, 2023.

[77] ResearchGate GmbH. Research gate. ⟨https://www.researchgate.net⟩, accessed April 12, 2023.

[78] T. Tomberg, T. Hieta, M. Vainio, and L. Halonen. Cavity-enhanced cantilever-enhanced photoacoustic spectroscopy. *Analyst*, 144(7):2291–2296, 2019. ⟨https://doi.org/10.1039/C9AN00058E⟩.

[79] Q. Wang, J. Wang, L. Li, and Q. Yu. An all-optical photoacoustic spectrometer for trace gas detection. *Sens. Actuators B Chem.*, 153(1):214–218, 2011. ⟨https://doi.org/10.1016/j.snb.2010.10.035⟩.

[80] K. Lundström, K. R. Matthews, and J.-E. Haugen. Pig meat quality from entire males. *Animals*, 3(11):1497–1507, 2009. ⟨https://dx.doi.org/10.1017/S1751731109990693⟩.

[81] S. M. Cristescu, J. Mandon, D. Arslanov, J. De Pessemier, C. Hermans, and F. J. M. Harren. Current methods for detecting ethylene in plants. *Ann. Botany*, 111(3):347–360, 2013. ⟨https://doi.org/10.1093/aob/mcs259⟩.

[82] V. Hansen, D. Müller-Stöver, L. J. Munkholm, C. Peltre, H. Hauggaard-Nielsen, and L. S. Jensen. The effect of straw and wood gasification biochar on carbon sequestration, selected soil fertility indicators and functional groups in soil: An incubation study. *Geoderma*, 269:99–107, 2016. ⟨https://doi.org/10.1016/j.geoderma.2016.01.033⟩.

[83] B. D. Adamson, J. E. Sader, and A. J. Bieske. Photoacoustic detection of gases using microcantilevers. *J. Appl. Phys.*, 106(11):114510, 2009. ⟨https://doi.org/10.1063/1.3271157⟩.

[84] T. Laurila. *Advances in Optical Diagnostic Based on Tunable Diode Laser Spectroscopy*. ⟨https://trepo.tuni.fi/handle/10024/114747⟩, 2005. ISBN 952-15-1480-9. Ph.D Thesis.

[85] H. Cattaneo. *Applications of Tunable Diode Lasers in Transmission and Photoacoustic Spectroscopy*. ⟨https://trepo.tuni.fi//handle/10024/114599⟩, 2006. ISBN 952-15-1480-9. Ph.D Thesis.

[86] H. Cattaneo, T. Laurila, and R. Hernberg. Photoacoustic detection of oxygen using cantilever enhanced technique. *Appl. Phys. B*, 85(2-3):337–341, 2006. ⟨https://doi.org/10.1007/s00340-006-2336-5⟩.

[87] J. Uotila. *Use of the Optical Cantilever Microphone in Photoacoustic Spectroscopy*. ⟨https://urn.fi/URN:ISBN:978-951-29-3912-1⟩, 2009. ISBN 978-951-29-3912-1. Ph.D Thesis.

[88] J. Uotila. Comparison of infrared sources for a differential photoacoustic gas detection system. *Infrared Phys. Technol.*, 51(2):122–130, 2007. ⟨https://doi.org/10.1016/j.infrared.2007.05.001⟩.

[89] J. Saarela. *Gas-Phase Photoacoustic Spectroscopy, Advanced methods for Photoacoustic Detection and Signal Processing*. ⟨https://urn.fi/URN:NBN:fi:tty-2011121214927⟩, 2011. ISBN 978-952-15-2676-3. Ph.D Thesis.

[90] J. Saarela, J. Toivonen, A. Manninen, T. Sorvajärvi, and R. Hernberg. Wavelength modulation waveforms in laser photoacoustic spectroscopy. *Appl. Opt.*, 48(4):743–747, 2009. ⟨https://doi.org/10.1364/AO.48.000743⟩.

[91] P. Sievilä. *Microfabrication technologies for single-crystal silicon sensors*. ⟨http://urn.fi/URN:ISBN:978-952-60-5451-3⟩, 2013. ISBN 978-952-62-5450-6. Ph.D Thesis.

[92] P. Sievilä, N. Chekurov, J. Raittila, and I. Tittonen. Sensitivity-improved silicon cantilever microphone for acousto-optical detection. *Sens. Actuators A Phys.*, 190:90–95, 2013. ⟨https://doi.org/10.1016/j.sna.2012.11.020⟩.

[93] N. E. Glauvitz. *MEMS Cantilever Sensor for THz Photoacoustic Chemical Sensing and Spectroscopy*. 2013. Ph.D Thesis, ⟨https://scholar.afit.edu/etd/509⟩.

[94] T. Välikylä. *Michelson Interferometer With Porch Swing Bearing For Portable FTIR Spectrometer*. Ph.D Thesis, ⟨https://urn.fi/URN:ISBN:978-951-29-5725-5⟩, year = 2014, isbn = 978-951-29-5725-5, publisher = University of Turku, Deparment of Physics and Astronomy.

[95] T. Välikylä and J. Kauppinen. Modulation depth of Michelson interferometer with Gaussian beam. *Appl. Opt.*, 50(36):6671–6677, 2011. ⟨https://doi.org/10.1364/AO.50.006671⟩.

[96] T. Välikylä and J. Kauppinen. Experiments on the porch swing bearing of Michelson interferometer for low resolution FTIR. *Adv. Opt. Technol.*, 2013(34):6671–6677, 2013. ⟨https://doi.org/10.1155/2013/948638⟩.

[97] C. B. Hirschmann. *Cantilever-Enhanced Photoacoustic Spectroscopy in the Analysis of Volatile Organic Compounds*. University of Oulu, Faculty of Tehcnology, 2013. ISBN 978-951-38-8106-1. Ph.D Thesis, ⟨http://www.vtt.fi/publications/index.jsp⟩.

[98] C. B. Hirschmann, J. Uotila, S. Ojala, J. Tenhunen, and R. L. Keiski. Fourier transform infrared photoacoustic multicomponent gas spectroscopy with optical cantilever detection. *Appl. Spectrosc.*, 64(3):293–297, 2010. ⟨https://doi.org/10.1366/000370210790918490⟩.

[99] C. B. Hirschmann, N. S. Koivikko, J. Raittila, J. Tenhunen, S. Ojala, K. Rahkamaa-Tolonen, R. Marbach, S. Hirschmann, and R. L. Keiski. FT-IR-cPAS—new photoacoustic measurement technique for analysis of hot gases: A case study on VOCs. *Sensors*, 11:5270–5289, 2011. ⟨https://doi.org/10.3390/s110505270⟩.

[100] C. B. Hirschmann, S. Sinisalo.and J. Uotila, S. Ojala, and R. L. Keiski. Trace gas detection of benzene, toluene, *p*-, *m*- and *o*-xylene with a compact measurement system using cantilever enhanced photoacoustic spectroscopy and optical parametric oscillator. *Vib. Spectrosc.*, 68:170–176, 2013. ⟨https://doi.org/10.1016/j.vibspec.2013.07.004⟩.

[101] J. Lehtinen. *Detection of Illicit Drugs and Drug Precursors with Cantilever-Enhanced Photoacoustic Spectroscopy*. University of Turku, Deparment of Physics and Astronomy, 2013. ISBN 978-951-29-5631-9. Ph.D Thesis, ⟨http://urn.fi/URN:ISBN:978-951-51-1664-2⟩.

[102] J. Uotila, J. Lehtinen, T. Kuusela, S. Sinislao, G. Maisons, F. Terzi, and I. Tittonen. Drug precursor vapor phase sensing by cantilever enhanced photoacoustic spectroscopy and quantum cascade laser. *Proc. SPIE*, 854501, 2012. ⟨https://doi.org/10.1117/12.974508⟩.

[103] J. Lehtinen. Spectroscopic studies of human hair, nail, and saliva samples using a cantilever-based photoacoustic detection. *Int. J. Thermophys*, 34(8-9):1559–1568, 2013. ⟨https://doi.org/10.1007/s10765-013-1488-x⟩.

[104] J. Lehtinen and T. Kuusela. Broadly tunable quantum cascade laser in cantilever-enhanced photoacoustic infrared spectroscopy of solids. *Appl. Phys. B*, 115(3):413–418, 2014. ⟨https://doi.org/10.1007/s00340-013-5617-9⟩.

[105] R. Pönni. *Changes in accessibility of cellulose for kraft pulps measured by deuterium exchange*. Aalto University, Deparment of Forest Products Technology, 2014. ISBN 978-952-60-5686-9. Ph.D Thesis, ⟨http://urn.fi/URN:ISBN:978-952-60-5686-9⟩.

[106] R. Pönni, E. Kontturi, and T. Vuorinen. Accessibility of cellulose: Structural changes and their reversibility in aqueous media. *Carbohydr. Polym.*, 93:424–429, 2013. ⟨https://doi.org/10.1016/j.carbpol.2012.12.025⟩.

[107] R. Pönni, L. Galvis, and T. Vuorinen. Changes in accessibility of cellulose during kraft pulping of wood in deuterium oxide. *Carbohydr. Polym.*, 101:792–797, 2014. ⟨https://doi.org/10.1016/j.carbpol.2013.10.001⟩.

[108] R. Pönni, L. Rautkari, C. A. S. Hill, and T. Vuorinen. Accessibility of hydroxyl groups in birch kraft pulps quantified by deuterium exchange in D_2O vapor. *Cellulose*, 21:1217–1226, 2014. ⟨https://doi.org/10.1007/s10570-014-0166-x⟩.

[109] M. Loria. *Transport properties of drug precursor molecules in nanoporous polymers*. Universita Degli Studi Di Salermo, 2014. ISBN 978-951-29-5725-5. Ph.D Thesis, ⟨http://elea.unisa.it:8080/xmlui/handle/10556/1455⟩.

[110] J. Peltola. *Trace gas detection and high-precision spectroscopy in the mid-infrared and visible wavelength regions*. University of Helsinki, Faculty of Science, 2015. ISBN 978-951-51-1664-2. Ph.D Thesis, ⟨http://urn.fi/URN:ISBN:978-951-51-1664-2⟩.

[111] J. Peltola, T. Hieta, and M. Vainio. Parts-per-trillion-level detection of nitrogen dioxide by cantilever-enhanced photoacoustic spectroscopy. *Opt. Lett.*, 40(13):2933–2936, 2015. ⟨https://doi.org/10.1364/OL.40.002933⟩.

[112] J. Rouxel. *Design and realization of miniaturized photoacoustic cells for trace gas detection*. Univ. de Reims Champagne-Ardenne, 2015. Ph.D Thesis, ⟨https://hal.science/tel-01526825⟩.

[113] G. Aoust. *Development of infrared sources and quartz resonators for photoacoustic spectroscopy*. Université Paris Saclay (COmUE), 2016. Ph.D Thesis, ⟨https://hal.science/tel-01430306v2⟩.

[114] E. Niinivaara. *2-Dimensional Assembly of Cellulose-Based Materials*. Aalto University, Department of Forest Products Technology, 2016. ISBN 978-952-60-6674-5. Ph.D Thesis, ⟨http://urn.fi/URN:ISBN:978-952-60-6674-5⟩.

[115] A. Brangule. *Application of Fourier Transform Infrared Spectroscopy in Analysis of Synthesized and Natural Calcium Phosphate*. Riga Technical University, Latvia, 2017. ISBN 978-9934-22-028-9. Ph.D Thesis, ⟨https://ortus.rtu.lv/science/en/publications/26412/attachments/3708⟩.

[116] A. Brangule, K. A. Gross, I. Skadiņš, A. Reinis, and J. Kroiča. Simultaneous identification of amorphous calcium phosphate and *S.epidermidis* bacteria by photoacoustic spectroscopy. *Key Eng. mater.*, 720:125–129, 2016. ISSN 1662-9795. ⟨https://doi.org/10.4028/www.scientific.net/KEM.720.125⟩.

[117] A. Brangule, I. Skadiņš, A. Reinis, K. A. Gross, and J. Kroiča. In vitro characterization perspectives using fourier transform infrared photoacoustic spectroscopy (FTIR-PAS) and diffuse reflectance infrared spectroscopy (DRIFT). *Key Eng. mater.*, 758:273–277, 2017. ISSN 1662-9795. ⟨https://doi.org/10.4028/www.scientific.net/KEM.758.273⟩.

[118] J. O. Eduah. *Phosphorus Reactions in Three Contrasting Soils Amended with Biochar*. University of Ghana, Department of Soil Science, 2018. Ph.D Thesis, ⟨http://ugspace.ug.edu.gh/handle/123456789/27339⟩.

[119] J. Karhu. *Applications of Mid-infrared Frequency Combs for Linear and Nonlinear Vibrational Spectroscopy*. University of Helsinki, Faculty of Science, 2019. ISBN 978-951-51-5261-9. Ph.D Thesis, ⟨http://urn.fi/URN:ISBN:978-951-51-5261-9⟩.

[120] J. Mikkonen. *Infrared Nuclear Magnetic Resonance Spectroscopic Methods for Salivary Analysis*. University of Eastern Finland, 2019. ISBN 978-952-61-3052-1. Ph.D Thesis, ⟨http://urn.fi/URN:ISBN:978-952-61-3052-1⟩.

[121] J. J. W. Mikkonen, J. Raittila, L. Rieppo, R. Lappalainen, A. M. Kullaa, and S. Myllymaa. Fourier transform infrared spectroscopy and photoacoustic spectroscopy for saliva analysis. *Appl. Spectrosc.*, 70(9):1502–1510, 2016. ⟨https://doi.org/10.1177/0003702816654149⟩.

[122] T. Tomberg. *Application of interferometry and cantilever-enhanced photo-acoustic spectroscopy to background-free trace gas detection*. University of Helsinki, Faculty of Science, 2020. ISBN 978-951-51-6563-3. Ph.D Thesis, ⟨http://urn.fi/URN:ISBN:978-951-51-6563-3⟩.

[123] T. Tomberg, N. Vuorio, T. Hieta, M. Jussila, K. Hartonen, M. Vainio, T. Mikkonen, J. Toivanen, M.-L. Riekkola, L. Halonen, and M. Metsälä. Broadband laser-based infrared detector for gas chromatography. *Anal. Chem.*, 92(21):14582–14588, 2020. ⟨https://doi.org/10.1021/acs.analchem.0c02887⟩.

[124] H. Wikström. *Exploring Printed Drug Formulations for Inkjet and Stencil Printing : A study in Pharmaceutical Sciences*. Åbo Akademi University, Faculty of Science and Engineering, 2020. ISBN 978-952-12-4009-6. Ph.D Thesis, ⟨https://urn.fi/URN:ISBN:978-952-12-4009-6⟩.

[125] H. Wickström, R. Koppolu, E. Mäkilä, M. Toivakka, and N. Sandler. Stencil printing—a novel manufacturing platform for orodispersible discs. *Pharmaceutics*, 12(1):33, 2020. ⟨https://doi.org/10.3390/pharmaceutics12010033⟩.

[126] T. Mikkonen. *Fourier Transform Photoacoustic Spectroscopy with Broadband lasers*. Tampere University, Faculty of Engineering and Natural Sciences, 2023. ISBN 978-952-03-2845-0. Ph.D Thesis, ⟨http://urn.fi/URN:ISBN:978-952-03-2845-0⟩.

[127] T. Mikkonen, C. Amiot, A. Aalto, K. Patokoski, G. Goëry, and J. Toivonen. Broadband cantilever-enhanced photoacoustic spectroscopy in the mid-IR using a supercontinuum. *Opt. Lett.*, 43(20):5094, 2018. ⟨https://doi.org/10.1364/OL.43.005094⟩.

[128] I. Sadiek, T. Mikkonen, M. Vainio, J. Toivonen, and A. Foltynowicz. Optical frequency comb photoacoustic spectroscopy. *Phys. Chem. Chem. Phys.*, 20(44):27849–27855, 2018. ⟨https://doi.org/10.1039/c8cp05666h⟩.

[129] T. Mikkonen, Z. Eslami, G. Genty, and J. Toivonen. Supercontinuum intensity noise coupling in fourier transform photoacoustic spectroscopy. *Opt. Lett.*, 47(7):1713–1716, 2022. ⟨https://doi.org/10.1364/OL.454461⟩.

[130] T. Mikkonen, T. Hieta, G. Genty, P. Vanninen, and J. Toivonen. Sensitive multi-species photoacoustic gas detection based on mid-infrared supercontinuum source and miniature multipass cell. *Phys. Chem. Chem. Phys.*, 24:19481, 2022. ⟨https://doi.org/10.1039/d2cp01731h⟩.

[131] T. Mikkonen, D. Luoma, H. Hakulinen, G. Genty, P. Vanninen, and J. Toivonen. Detection of gaseous nerve agent simulants with broadband photoacoustic spectroscopy. *J. Haz. Mat.*, 440: 129851, 2022. ⟨https://doi.org/10.1016/j.jhazmat.2022.129851⟩.

[132] S. Palzer. Photoacoustic-based gas sensing: A review. *Sensors*, 20(9):2745, 2020. ⟨https://doi.org/10.3390/s20092745⟩.

[133] Y. Yin, D. Ren, C. Li, R. Chen, and J. Shi. Cantilever-enhanced photoacoustic spectroscopy for gas sensing: A comparison of different displacement detection methods. *Photoacoustics*, 28: 100423, 2022. ⟨https://doi.org/10.1016/j.pacs.2022.100423⟩.

[134] A. Fathy, Y. M. Sabry, I. W. Hunter, D. Khalil, and T. Bourouina. Direct absorption and photoacoustic spectroscopy for gas sensing and analysis: A critical review. *Laser Photonics Rev.*, 16 (8):2100556, 2022. ⟨https://doi.org/10.1002/lpor.202100556⟩.

[135] S. Wang, M. Hoffmann, A. K. Yetisen, K. Wang, F. Brändle, W. Kurz, M. Jakobi, and A. W. Koch. Optical interferometer-based methods for photoacoustic gas sensing:. *asr*, 2023. ⟨https://doi.org/10.1080/05704928.2023.2196729⟩.

[136] F. A. Batzias, C. G. Siontorou, and P.-M. p. Spanidis. Designing a reliable leak bio-detection system for natural gas pipelines. *J. Haz. Mat.*, 186(1):35–58, 2011. ⟨https://doi.org/10.1016/j.jhazmat.2010.09.115⟩.

[137] E. Hu, E. L. Babcock, S. E. Bialkowski, S. B. Jones, and M. Tuller. Methods and techniques for measuring gas emissions from agricultural and animal feeding operations. *Crit. Rev. Anal. Chem.*, 44:200–219, 2014. ISSN 1040-8347. ⟨https://doi.org/10.1080/10408347.2013.843055⟩.

[138] D. S. Volkov, O. B. Rogova, and M. A. Proskurnin. Photoacoustic and photothermal methods in spectroscopy and characterization of soils and soil organic matter. *Photoacoustics*, 17:100151, 2020. ⟨https://doi.org/10.1016/j.pacs.2019.100151⟩.

[139] C. Peltre, S. Bruun, C. Du, I. K. Thomsen, and L. S. Jensen. Assessing soil constituents and labile soil organic carbon by mid-infrared photoacoustic spectroscopy. *Soi. Biol. Biochem.*, 77 (4):41–50, 2014. ⟨https://doi.org/10.1016/j.soilbio.2014.06.022⟩.

[140] N. J. Vasa and M. Singaperumal. Gas sensors based on superluminescent diodes for combustion monitoring. *Appl. Opt.*, 48(1):G1–5, 2009. ⟨https://doi.org/10.1364/AO.48.0000G1⟩.

[141] T. Sorvajärvi, A. Manninen, J. Toivonen, J. Saarela, and R. Hernberg. Resonant photoacoustic cell for pulsed laser analysis of gases at high temperature. *Rev. Sci. Instrum.*, 80(12):123103, 2009. ⟨https://doi.org/10.1063/1.3266974⟩.

[142] S. Borri, P. Patimisco, A. Sampaolo, H. E. Beere, D. A. Ritchie, M. S. Vitiello, G. Scamarcio, and V. Spagnolo. Terahertz quartz enhanced photoacoustic sensor. *Appl. Phys. Lett.*, 103:021105, 2013. ⟨https://doi.org/10.1063/1.4812438⟩.

[143] S. Zhou, M. Slaman, and D. Iannuzzi. Demonstration of a highly sensitive photoacoustic spectrometer based on a miniaturized all-optical detecting sensor. *Opt. Exp.*, 25(15):17541–17548, 2017. ⟨https://doi.org/10.1364/OE.25.017541⟩.

[144] R. E. Lindley, A. M. Parkes, K. A. Keen, E. D. McNaghten, and A. J. Orr-Ewing. A sensitivity comparison of three photoacoustic cells containing a single microphone, a differential dual microphone or a cantilever pressure sensor. *Appl. Phys. B*, 86(4):707–713, 2007. ⟨https://doi.org/10.1007/s00340-006-2543-0⟩.

[145] A. M. Parkes, K. A. Keen, and E. D. McNaghten. Trace gas detection using a novel cantilever-based photoacoustic spectrometer with multiplexed optical fiber-coupled diode lasers and fiber-amplification. *Proc. SPIE*, 6770:66701C, 2007. ⟨https://doi.org/10.1117/12.736682⟩.

[146] E. D. McNaghten, K. A. Grant, A. M. Parkes, and P. A. Martin. Simultaneous detection of trace gases using multiplexed tunable diode lasers and a photoacoustic cell containing a cantilever microphone. *Appl. Phys. B*, 107(3):861–871, 2012. ⟨https://doi.org/10.1007/s00340-012-4980-2⟩.

[147] N. E. Glauvitz, R. A. Coutu Jr., I. R. Medvedev, and D. T. Petkie. Terahertz photoacoustic spectroscopy using an MEMS cantilever sensor. *J. Micromech. Systems*, 24(1):216–223, 2015. ⟨https://doi.org/10.1109/JMEMS.2014.2327916⟩.

[148] R. A. Coutu Jr., I. R. Medvedev, and D. T. Petkie. Improved sensitivity MEMS cantilever sensor for terahertz photoacoustic spectroscopy. *Sensors*, 16:251, 2016. ⟨https://doi.org/10.3390/s16020251⟩.

[149] M. Dostál, J. Suchánek, V. Válek, Z. Blatoňová, V. Nevrlý, P. Bitala, P. Kubát, and Z. Zelinger. Cantilever-enhanced photoacoustic detection and infrared spectroscopy of trace species produced by biomass burning. *Energy Fuels*, 32:10163–10168, 2018. ⟨https://doi.org/10.1021/acs.energyfuels.8b01021⟩.

[150] S. Zhou and D. Iannuzzi. A fiber-tip photoacoustic sensor for in situ trace gas detection. *Rev. Sci. Instrum.*, 90:023102, 2019. ⟨https://doi.org/10.1063/1.5082955⟩.

[151] K. Chen, H. Deng, M. Guo, C. Luo., S. Liu, B. Zhang, F. Ma, F. Zhu, S. Gong, W. Peng, and Q. Yu. Tube-cantilever double resonance enhanced fiber-optic photoacoustic spectrometer. *Opt. Laser Tech.*, 123:105894, 2020. ⟨https://doi.org/10.1016/j.optlastec.2019.105894⟩.

[152] J. Karhu, H. Philip, A. Baranov, R. Theissier, and T. Hieta. Sub-ppb detection of benzene using cantilever-enhanced photoacoustic spectroscopy with a long-wavelength infrared quantum cascade laser. *Opt. Lett.*, 45(21):5962, 2020. ⟨https://doi.org/10.1364/OL.405402⟩.

[153] L. Fu, P. Lu, C. Shima, J. Zhao, Y. Pan, T. Li, X. Zhang, and D. Liu. Small-volume highly-sensitive all-optical gas sensor using non-resonant photoacoustic spectroscopy with dual silicon cantilever optical microphones. *Photoacoustics*, 27:100382, 2022. ⟨https://doi.org/10.1016/j.pacs.2022.100382⟩.

[154] J. Karhu, M. Nyman, M. Siitari-Kauppi, and T. Hieta. Cantilever-enhanced photoacoustic measurement of HTO in water vapor. *Photoacoustics*, 29:100443, 2023. ⟨https://doi.org/10.1016/j.pacs.2022.100443⟩.

[155] K. Chen, Z. Gong, M. Guo, S. Yu, C. Qu, X. Zhou, and Q. Yu. Fiber-optic fabry-perot interferometer based high sensitive cantilever microphone. *Sens. Actuators A Phys.*, 279:107–112, 2018. ⟨https://doi.org/10.1016/j.sna.2018.06.010⟩.

[156] J. Suchánek, M. Dostál, T. Vlasáková, P. Janda, M. Klusáčková, P. Kubát, V. Nevrlý, P. Bitala, S. Civiš, and Z. Zelinger. First application of multilayer graphene cantilever for laser photoacoustic detection. *Measurement*, 101:9–14, 2017. ⟨https://dx.doi.org/10.1016/j.measurement.2017.01.011⟩.

[157] J. Suchánek, P. Janda, M. Dostál, A. Knížek, P. Kubát, P. Roupcová, P. Bitala, V. Nevrlý, and Z. Zelinger. Photoacoustic spectroscopy with mica and graphene micro-mechanical levers for multicomponent analysis of acetic acid, acetone and methanol mixture. *Microchem. J.*, 144:203–208, 2019. ⟨https://doi.org/10.1016/j.microc.2018.08.034⟩.

[158] J. Rakovsky and O. Votava. A simple photoacoustic detector for highly corrosive gases. *Rev. Sci. Instrum.*, 88:013103, 2017. ⟨https://doi.org/10.1063/1.4972584⟩.

[159] N. Ledermann, J. Baborowski, A. Seifert, B. Willing, S. Hiboux, p. Murault, N. Setter, and M. Forster. Piezoelectric cantilever microphone for photoacoustic gas detector. *Integrated Ferroelectrics*, 35:177–184, 2001. ⟨https://doi.org/10.1080/10584580108016899⟩.

[160] H. Takahashi, N. M. Dung, K. Matsumoto, and I. Shimoyama. Terahertz photoacoustic spectroscopy using an MEMS cantilever sensor. *Differential pressure sensor using a piezoresistive cantilever*, 22:055015, 2012. ⟨https://doi.org/10.1088/0960-1317/22/5/055015⟩.

[161] K. Liu, Y. Cao, G. Wanga, W. Zhang, W. Chen, and X. Gao. A novel photoacoustic spectroscopy gas sensor using a low cost polyvinylidene fluoride film. *Sens. Actuators B Chem.*, 277:571–575, 2018. ⟨https://doi.org/10.1016/j.snb.2018.09.037⟩.

[162] K. Chen, Q. Yu, Z. Gong, M. Guo, Z. Zhao, and C. Qu. Ultra-high sensitive fiber-optic fabry-perot cantilever enhanced resonant photoacoustic spectroscopy. *Sens. Actuators B Chem.*, 268 (1):205–209, 2018. ⟨https://doi.org/10.1016/j.snb.2018.04.123⟩.

[163] Gasera Ltd. Technical documents. ⟨https://www.gasera.fi⟩, accessed April 12, 2023.

[164] Gasera PA101. Technical documents, FTIR accessory PA101. ⟨https://d3pcsg2wjq9izr.cloudfront.net/files/49823/download/661239/0-6.pdf⟩, accessed December 18, 2023.

[165] Gasera PA301. Product presentation, FTIR accessory PA301. ⟨https://www.gasera.fi/wp-content/uploads/2015/12/PA301_Product_Presentation_22032011.pdf⟩, accessed December 18, 2023.

[166] Gasera F10. Technical documents, multi-gas analyzer F10. ⟨http://www.enviro-analytical.com/doc_bin/Gasera%20F10.pdf⟩, accessed December 18, 2023.

[167] Gasera LP1. Technical documents, laser PAS gas analyser LP1. ⟨https://www.sol-ma.net/wp-content/uploads/2015/05/gasera_brochure_LP1.pdf⟩, accessed December 18, 2023.

[168] Gasera PA201. Technical documents, photoacoustic detector PA201. ⟨https://www.gasera.fi/wp-content/uploads/2015/12/gasera_brochure_PA201_4page_18052012_web.pdf⟩, accessed December 18, 2023.

[169] Gasera ONE. Press release and technical documents, gasera ONE. ⟨https://pittcon.org/2016/exhibitor/pr/Gasera_Pittcon.pdf⟩, accessed December 18, 2023.

[170] Gasera ONE FA. Technical documents, gasera ONE FORMALDEHYDE. ⟨https://www.gasera.fi/wp-content/uploads/2017/02/gasera_brochure_ONE_FORMALDEHYDE_17022017_web.pdf⟩, accessed December 18, 2023.

[171] Gasera ONE SHED. Technical documents, gasera ONE SHED. ⟨https://www.gasera.fi/wp-content/uploads/2017/10/gasera_shed_brochure.pdf⟩, accessed December 18, 2023.

[172] Gasera ONE PULSE. Technical documents, gasera ONE PULSE. ⟨https://www.gasera.fi/wp-content/uploads/2018/06/gasera_esite_OnePulse_web_26062018.pd⟩, accessed December 18, 2023.

[173] Gasera ONE GHG. Technical documents, gasera ONE GHG. ⟨https://www.gasera.fi/wp-content/uploads/2020/03/GASERA_ONE_GHG_Brochure20032020_web.pdf⟩, accessed December 18, 2023.

[174] Gasera ONE HF. Technical documents, gasera ONE HF. ⟨https://www.gasera.fi/wp-content/uploads/2021/04/GASERA-ONE-HF_Hydrogen-fluoride-gas-monitor_Brochure_31032021_lores.pdf⟩, accessed December 18, 2023.

[175] Y. Li, B. Chen, P. Ouyang, Y. Duan, W.-J. Ong, and F. Dong. Engineering $ZnSn(OH)_6$ with ternary active sites-directed hydroxyl vacancies for robust deep C_6H_6 photo-oxidation: Experiment and DFT calculations. *Chem. Eng. J.*, 451(2):138695, 2023. ⟨https://doi.org/10.1016/j.cej.2022.138695⟩.

[176] W. Qu, P. Wang, X. Chen, and D. Zhang. Immunizing sulfate-mediated deactivation over TiO_2 photocatalysts for gaseous benzene purification via self-adaptive deoxygenation of sulfate radicals. *Appl. Catal. B: Environmental*, 321:122036, 2023. ⟨https://doi.org/10.1016/j.apcatb.2022.122036⟩.

[177] R. Fang, X. Huang, X. Luo, Y. Sun, Z. Liu, L. Ao, F. Dong, and H. Huang. Excellent stability for catalytic oxidation formaldehyde over defective δ-MnO_2 nanoparticles at room temperature. *J. Env. Chem. Eng.*, 11(1):109064, 2023. ⟨https://doi.org/10.1016/j.jece.2022.109064⟩.

[178] H. Gu, J. Lan, Y. Liu, C. Ling, K. Wei, G. Zhan, F. Guo, F. Jia, Z. Ai, L. Zhang, and X. Liu. Water enables lattice oxygen activation of transition metal oxides for volatile organic compound oxidation. *ACS Catal*, 12:11272–11280, 2022. ⟨https://doi.org/10.1021/acscatal.2c03552⟩.

[179] R. Yang, C. Lia, F. Yuan, C. Wu, Z. Sun, and R. Ma. Synergistic effect of diatomite and Bi self-doping Bi_2MoO_6 on visible light photodegradation of formaldehyde. *Micropor. Mesopor. Mater.*, 339:112003, 2022. ⟨https://doi.org/10.1016/j.micromeso.2022.112003⟩.

[180] F. Yuan, R. Yang, C. Li, Y. Tan, X. Zhang, S. Zheng, and Z. Sun. Enhanced visible-light degradation performance toward gaseous formaldehyde using oxygen vacancy-rich TiO_{2-x}/TiO_2 supported by natural diatomite. *Build. Environ.*, 12:11272–11280, 2022. ⟨https://doi.org/10.1016/j.buildenv.2022.109216⟩.

[181] M. Ran, W. Cui, K. Li, L. Chen, Y. Zhang, F. Dong, and Y. Sun. Light-induced dynamic stability of oxygen vacancies in $BiSbO_4$ for efficient photocatalytic formaldehyde degradation. *EEM*, 5 (1):305–312, 2022. ⟨https://doi.org/10.1002/eem2.12176⟩.

[182] D. Li, J. Lu, C. Wang, Y. Xing, S. Liang, R. Wang, X. Zhang, and Y. Liu. Photo-plasma catalytic degradation of high concentration volatile organic compounds. *Appl. Catal. A: General*, 647: 118908, 2022. ⟨https://doi.org/10.1016/j.apcata.2022.118908⟩.

[183] X. Li, J. Li, G. Zhang, W. Yang, L. Yang, Y. Shen, Y. Sun, and F. Dong. Enhanced reactant activation and transformation for efficient photocatalytic acetone degradation on SnO_2 via Hf doping. *Adv. Sustainable Syst.*, 5(8):2100115, 2021. ⟨https://doi.org/10.1002/adsu.202100115⟩.

[184] L. Chen, K. Li, Y. Yang, T. Xue, H. Wang, B. Lei, J. Sheng, F. Dong, and Y. Sun. Amorphous SnO_2 decorated $ZnSn(OH)_6$ promotes interfacial hydroxyl polarization for deep photocatalytic toluene mineralization. *J. Hazard. Mater.*, 444(B):103436, 2023. ⟨https://doi.org/10.1016/j.jhazmat.2022.130436⟩.

[185] H. Karlsson and S. Sinisalo. Air quality monitoring with photoacoustic spectroscopy. *Optik Photonik*, 12(1):36–39, 2017. ⟨https://doi.org/10.1002/opph.201700002⟩.

[186] P. J. Jodlowski, R. J. Jedrzejczyk, D. Chlebda, M. Gierada, and J. Lojewska. In situ spectroscopic studies of methane catalytic combustion over Co, Ce, and Pd mixed oxides deposited on a steel surface. *J. Catalyst*, 350:1–12, 2017. ⟨https://doi.org/10.1016/j.jcat.2017.03.022⟩.

[187] M. He, J. Ji, B. Liu, and H. Huang. Reduced TiO_2 with tunable oxygen vacancies for catalytic oxidation of formaldehyde at room temperature. *Appl. Surf. Sci.*, 473:934–942, 2019. ⟨https://doi.org/10.1016/j.apsusc.2018.12.212⟩.

[188] K. Li, J. Li, H. Huang, and M. He. Efficient activation of Pd/CeO_2 catalyst by non-thermal plasma for complete oxidation of indoor formaldehyde at room temperature. *Chemosphere*, 246: 125762, 2020. ⟨https://doi.org/10.1016/j.chemosphere.2019.125762⟩.

[189] W. Yang, W. Cui, L. Yang, G. Zhang, X. Li, Y. Shen, F. Dong, and Y. Sun. The structural differences of perovskite $ATiO_3$ (A = Ca, Sr) dictate the photocatalytic VOCs mineralization efficiency. *Chem. Eng. J.*, 425:130613, 2021. ISSN 1385-8947. ⟨https://doi.org/10.1016/j.cej.2021.130613⟩.

[190] W. Wang, F. Lin, T. An, S. Qiu, H. Yu, B. Yan, G. Chen, and L.-A. Hou. Photocatalytic mineralization of indoor VOC mixtures over unique ternary TiO_2/C/MnO_2 with high adsorption selectivity. *Chem. Eng. J.*, 425:131678, 2021. ISSN 1385-8947. ⟨https://doi.org/10.1016/j.cej.2021.131678⟩.

[191] L. Yan, Q. Wang, W. Qu, T. Yan, H. Li, P. Wang, and D. Zhang. Tuning $Ti^{\delta+}$-Vo-$Pt^{\delta+}$ interfaces over Pt/TiO_2 catalysts for efficient photocatalytic oxidation of toluene. *Chem. Eng. J.*, 431(2): 134209, 2022. ⟨https://doi.org/10.1016/j.cej.2021.134209⟩.

[192] M. C. Lind, H. Koskela, B. Venås, A.W. Vikan, P. Kalliomäki, and T. T. Harsem. Designing simplified airborne infection isolation rooms to reduce infection rate in future pandemics. *ASHRAE Transactions*, 125(2):280, 2019.

[193] S. Dugheri, D. Massi, N. Mucci, N. Berti, G. Cappelli, and G. Arcangeli. How improvements in monitoring and safety practices lowered airborne formaldehyde concentrations at an italian university hospital: a summary of 20 years of experience. *Arh. Hig. Rada. Toksikol.*, 71(3): 178–189, 2020. ⟨https://doi.org/10.2478/aiht-2020-71-3406⟩.

[194] P. Kalliomäki, H. Koskela, M. Waris, and J. W. Tang. Assessing the risk to healthcare workers of hospital-acquired infection from patients infected with aerosol-

transmissible pathogens. *IOSH Research Report*, 2020. ⟨https://iosh.com/media/8432/aerosol-infection-risk-hospital-patient-care-full-report.pdf⟩.

[195] A. Lipczynska, M. P. Bivolarova, L. Guo, W. Kierat, and A. K. Melikov. Airborne infection probability in relation of room air distribution: an experimental investigation. *E3S Web of Conferences*, 356:05014, 2022. ⟨https://doi.org/10.1051/e3sconf/202235605014⟩.

[196] A. Lipczynska, M. P. Bivolarova, L. Guo, W. Kierat, and A. K. Melikov. Experimental evaluation of the airborne infection probability in ventilated office room at different supply airflow rates. *E3S Web of Conferences*, 356:05001, 2022. ⟨https://doi.org/10.1051/e3sconf/202235605001⟩.

[197] S. Dorregaray-Oyaregui, A. Ariño, L. A. de Brito, A. Zuaua-Ros, J. C. Ramos, R. Manzueta, B. S. Sáiz-Ezquerra, and C. Martín-Gómez. The conceptualization of exhalation in buildings. In *Proceedings of CLIMA 2022 The 14th REHVA HVAC World Congress*. Federation of European Heating, Ventilation and Air Conditioning Association, 2022. ⟨https://doi.org/10.34641/clima.2022.424⟩.

[198] N. Kappelt, H. S. Russell, D. Fessa, K. van Ryswyk, O. Hertel, and M. S. Johnson. Particulate air pollution in the copenhagen metro part 1: Mass concentrations and ventilation. *Environ. Int.*, 171:107621, 2023. ⟨https://doi.org/10.1016/j.envint.2022.107621⟩.

[199] R. Ming, P. Mustakallio, R. Kosonen, T. Kaukola, S. Kilpeläinen, B. Li, Y. Wu, and R. Yao. Effect of active chilled beam layouts on ventilation performance and thermal comfort under variable heat gain conditions. *Build. Environ.*, 228:109872, 2023. ⟨https://doi.org/10.1016/j.buildenv.2022.109872⟩.

[200] M. Predotova, E. Schlecht, and A. Buerkert. Nitrogen and carbon losses from dung storage in urban gardens of Niamey, Niger. *Nutr. Cycl. Agroecosyst*, 87(1):103–114, 2010. ⟨https://doi.org/10.1007/s10705-009-9316-1⟩.

[201] G. Bekiaris, S. Bruun, C. Peltre, S. Houot, and L. S. Jensen. FTIR–PAS: A powerful tool for characterising the chemical composition and predicting the labile C fraction of various organic waste products. *Waste Manag.*, 39:45–56, 2015. ⟨https://doi.org/10.1016/j.wasman.2015.02.029⟩.

[202] C. Du, J. Wang, Z. Zhou, Y. Shen, and J. Zhou. In situ measurement of ammonia concentration in soil headspace using fourier transform mid-infrared photoacoustic spectroscopy. *Pedosphere*, 25(4):605–612, 2015. ⟨https://doi.org/10.1016/S1002-0160(15)30040-0⟩.

[203] G. Bekiaris, J. M. Triolo, C. Peltre, and L. S. Jensen S. Bruun. Rapid estimation of the biochemical methane potential of plant biomasses using fourier transform mid-infrared photoacoustic spectroscopy. *Bioresour. Technol.*, 197:475–481, 2015. ⟨https://doi.org/10.1016/j.biortech.2015.08.050⟩.

[204] V. Hansen, A. Saarsalmi, and C. Peltre. Changes in SOM composition and stability to microbial degradation over time in response to wood chip ash fertilisation. *Soil. Bio. Biochem.*, 99:179–186, 2016. ⟨https://doi.org/10.1016/j.soilbio.2016.05.012⟩.

[205] E. Negussie, J. Lehtinen, P. Mäntysaari, A. R. Bayat, A.-E. Liinamo, E. A. Mäntysaari, and M. H. Lidauer. Non-invasive individual methane measurement in dairy cows. *Animal*, 11(5):890–899, 2017. ⟨https://doi.org/10.1017/S1751731116002718⟩.

[206] C. Peltre, E. G. Gregorich S. Bruun, L. S. Jensen, and J. Magid. Repeated application of organic waste affects soil organic matter composition: Evidence from thermal analysis, FTIR-PAS, amino sugars and lignin biomarkers. *Soi. Biol. Biochem.*, 104:117–127, 2017. ⟨https://doi.org/10.1016/j.soilbio.2016.10.016⟩.

[207] M. Zhang, G. Cheng, H. Feng, B. Sun, Y. Zhao, H. Chen, J. Chen, M. Dyck, X. Wang, J. Zhang, and A. Zhang. Effects of straw and biochar amendments on aggregate stability, soil organic carbon, and enzyme activities in the Loess Plateau, China. *Environ. Sci. Pollut. Res.*, 24:20130311, 2017. ⟨https://doi.org/10.1007/s11356-017-8505-8⟩.

[208] B. Gómez-Muñoz, J. D. Larsen, G. Bekiaris, C. Scheutz, S. Bruun, S. Nielsen, and L.S. Jensen. Nitrogen mineralisation and greenhouse gas emission from the soil application of sludge from reed bed mineralisation systems. *J. Environ. Manag.*, 203(1):59–67, 2017. ⟨https://doi.org/10.1016/j.jenvman.2017.07.042⟩.

[209] N. S. Raymond, D. Müller Stöver, C. Peltre, H. Hauggaard Nielsen, and L. Stoumann Jensen. Use of *Penicillium bilaiae* to improve phosphorus bioavailability of thermally treated sewage sludge – a potential novel type biofertiliser. *Proc. Biochem.*, 69:169–177, 2018. ⟨https://doi.org/10.1016/j.procbio.2018.03.021⟩.

[210] J. L. Jensen, P. Schjønning, C. W. Watts, B. T. Christensen, C. Peltre, and L. J. Munkholm. Relating soil C and organic matter fractions to soil structural stability. *Geoderma*, 337:834–843, 2019. ⟨https://doi.org/10.1016/j.geoderma.2018.10.034⟩.

[211] P. C. Garnsworthy, G. F. Difford, M. J. Bell, A. R. Bayat, P. Huhtanen, B. Kuhla, J. Lassen, N. Peiren, M. Pszczola, D. Sorg, M. H. P. W. Visker, and T. Yan. Comparison of methods to measure methane for use in genetic evaluation of dairy cattle. *Animals*, 9(10):837, 2019. ⟨https://doi.org/10.3390/ani9100837⟩.

[212] J. P. McIlroy, K. L. McGeough, R. J. Laughlin, and R. Carolan. Abatement of ammonia emissions from dairy cow house concrete floor surfaces through additive application. *Biosyst. Eng.*, 188:320–330, 2019. ⟨https://doi.org/10.1016/j.biosystemseng.2019.10.016⟩.

[213] C. Lee, D.L. Morris, K.M. Lefever, and P.A. Dieter. Feeding a diet with corn distillers grain with solubles to dairy cows alters manure characteristics and ammonia and hydrogen sulfide emissions from manure. *J. Dairy Sci.*, 103(3):2363–2372, 2020. ⟨https://doi.org/10.3168/jds.2019-17524⟩.

[214] G. Bekiaris, C. Peltre, S. T. Barsberg, S. Bruun, K. M. Sørensen, S. B. Engelsen, J. Magid, M. Hansen, and L. S. Jensen. Three different fourier-transform mid-infrared sampling techniques to characterize bio-organic samples. *J. Environ. Qual.*, 49(5):1310–1321, 2020. ⟨https://doi.org/10.1002/jeq2.20106⟩.

[215] J. Huang, Å. Rinnan, T. B. Bruun, T. Engedal, and S. Bruun. Identifying the fingerprint of permanganate oxidizable carbon as a measure of labile soil organic carbon using fourier transform mid-infrared photoacoustic spectroscopy. *Eur. J. Soil Sci.*, 72(4):1831–1841, 2021. ⟨https://doi.org/10.1111/ejss.13085⟩.

[216] L. Furst, M. Feliciano, L. Frare, and G. Igrejas. A portable device for methane measurement using a low-cost semiconductor sensor: Development, calibration and environmental applications. *Sensors*, 21(22):7456, 2021. ⟨https://doi.org/10.3390/s21227456⟩.

[217] J. Huang, G. Bekiaris, T. Fitamo, C. Scheutz, and S. Bruun. Prediction of biochemical methane potential of urban organic waste using fourier transform mid-infrared photoacoustic spectroscopy and multivariate analysis. *Sci. Total Environ.*, 790:147959, 2021. ISSN 0048-9697. ⟨https://doi.org/10.1016/j.scitotenv.2021.147959⟩.

[218] C. E. Egene, I. Regelink, I. Sigurnjak, F. Adani, F. M. G. Tack, and E. Meersa. Saturated salt solutions in showcases: humidity control and pollutant absorption. *Appl. Soil Ecol.*, 178:104577, 2022. ⟨https://doi.org/10.1016/j.apsoil.2022.104577⟩.

[219] C. M. J. Hendriks, V. Shrivastava, I. Sigurnjak, J. P. Lesschen, E. Meers, R. van Noort, Z. Yang, and R. P. J. J.Rietra. Replacing mineral fertilisers for bio-based fertilisers in potato growing on sandy soil: A case study. *Appl. Sci*, 12(1):341, 2022. ⟨https://doi.org/10.3390/app12010341⟩.

[220] A. Szaja, A. Montusiewicz, S. Pasieczna-Patkowska, and M. Lebiocka. Technological and energetic aspects of multi-component co-digestion of the beverage industry wastes and municipal sewage sludge. *Energies*, 15(15):5395, 2022. ⟨https://doi.org/10.3390/en15155395⟩.

[221] H. M. Zynda, J. E. Copelin, W. P. Weiss, and C. Lee F. Sun. Effects of reducing dietary cation-anion difference on lactation performance and nutrient digestibility of lactating cows and ammonia emissions from manure. *J. Dairy. Sci.*, 105:4016–4031, 2022. ⟨https://doi.org/10.3168/jds.2021-21195⟩.

[222] H. M. Zynda, J. E. Copelin, L. R. Rebelo, W. P. Weiss, and C. Lee M. Wilcken. Effects of corn distillers grains with yeast bodies and manipulation of dietary cation and anion difference on production, nutrient digestibility, and gas emissions from manure in lactating cows. *J. Dairy. Sci.*, 105:8054–8068, 2022. ⟨https://doi.org/10.3168/jds.2021-21456⟩.

[223] J. Huang, N. Glæsner, J. M. Triolo, G. Bekiaris, S. Bruun, and F. Liu. Application of fourier transform mid-infrared photoacoustic spectroscopy for rapid assessment of phosphorus avail-

ability in digestates and digestate-amended soils. *Sci. Total Environ.*, 832:155040, 2022. ⟨https://doi.org/10.1016/j.scitotenv.2022.155040⟩.

[224] H. Huuki, M. Tapio, P. Mäntysaari, E. Negussie, S. Ahvenjärvi, J. Vilkki, A. Vanhatalo, and I. Tapio. Long-term effects of early-life rumen microbiota modulation on dairy cow production performance and methane emissions. *Front. Microbiol.*, 13, 2022. ⟨https://doi.org/10.3389/fmicb.2022.983823⟩.

[225] N. R. E. N. Impens, K. A. Jensen, L. Skipperud, A. Van Gompel, and N. Vanhoudt. In-depth understanding of local soil chemistry reveals that addition of Ca may counteract the mobilisation of ^{226}Ra and other pollutants before wetland creation on the grote nete river banks. *Sci. Total Environ.*, 823:153703, 2022. ⟨https://doi.org/10.1016/j.scitotenv.2022.153703⟩.

[226] J. Karhu and T. Hieta. Enhancement of photoacoustic spectroscopy with sorption enrichment for ppt-level benzene detection. *Appl. Opt.*, 61(8):1892–1897, 2022. ⟨https://doi.org/10.1364/AO.450407⟩.

[227] J. Lu, X. Liu, H. Zhang, M. Fu, H. Zheng, Q. Chen, and J. Zhou. Electrocatalytic activity of nano-flowered yavapaiite anchored on magnetic graphite oxide for nitrate selective reduction. *Chem. Eng. J.*, 433(1):134586, 2022. ⟨https://doi.org/10.1016/j.cej.2022.134586⟩.

[228] V. Sánches-Navarro, V. Shahrokh, S. Martínez-Martínez, J. A. Acosta, M. Almagro, M. Martínez-Mena, C. Boix-Fayos, E. Díaz-Pereir, and R. Zornoza. Perennial alley cropping contributes to decrease soil CO_2 and N_2O emissions and increase soil carbon sequestration in a Mediterranean almond orchard. *Sci. Tot. Environ.*, 845(1):157225, 2022. ⟨https://doi.org/10.1016/j.scitotenv.2022.157225⟩.

[229] K. R. Baral, J. McIlroy, G. Lyons, and C. Johnston. The effect of biochar and acid activated biochar on ammonia emissions during manure storage. *Environ. Pollut*, 317:120815, 2023. ⟨https://doi.org/10.1016/j.envpol.2022.120815⟩.

[230] C. Díaz-García, J. J. Martínez-Sánchez, and J. Álvarez-Rogel. Woodchip bioreactors for saline leachates denitrification can mitigate agricultural impacts in mediterranean areas: The campo de cartagena-mar menor environmental issue. *J. Environ. Manage.*, 331:117292, 2023. ⟨https://doi.org/10.1016/j.jenvman.2023.117292⟩.

[231] V. Sánches-Navarro, S. Martínez-Martínez, J. A. Acosta, M. Almagro, M. Martínez-Mena, C. Boix-Fayos, E. Díaz-Pereir, A. Temnani, P. Berrios, A. Pérez-Pastor, and R. Zornoza. Soil greenhouse gas emissions and crop production with implementation of alley cropping in a mediterranean citrus orchard. *Eur. J. Agron.*, 142:126684, 2023. ⟨https://doi.org/10.1016/j.eja.2022.126684⟩.

[232] M. Vargas-Sánchez, J. Alcocer, S. Sánchez-Carrillo, L. A. Oseguera, E. M. Rivera-Herrera, I. Soria-Reinoso, A. Guzmán-Arias, F. García-Oliva, and M. Merino-Ibarra. Carbon dioxide concentration and emissions along a trophic gradient in tropical karst lakes. *Water*, 15(1):13, 2023. ⟨https://doi.org/10.3390/w15010013⟩.

[233] M. Känsäkoski, M. Kurkinen, N. von Weymarn, P. Niemelä, P. Neubauer, E. Juuso, T. Eerikäinen, S. Turunen, S. Aho, and P. Suhonen. *Process analytical technology (PAT) needs and applications in the bioprocess industry*. VTT, 2006. ISBN 951-38-6612-2.

[234] M. Calderisi, A. Ulrici, S. Sinisalo, J. Uotila, and R. Seeber. Simulation of an experimental database of infrared spectra of complex gaseous mixtures for detecting specific substances. the case of drug precursors. *Sensors and Actuators B: Chemical*, 193:806–814, 2014. ⟨https://doi.org/10.1016/j.snb.2013.12.035⟩.

[235] P. V. Almeida, M.-A. Shahbazi, E. Mäkilä, M. Kaasalainen, J. Salonen, J. Hirvonen, and H. A. Santos. Amine-modified hyaluronic acid-functionalized porous silicon nanoparticles for targeting breast cancer tumors. *Nanoscale*, 6(17):10377–10387, 2014. ⟨https://doi.org/10.1039/C4NR02187H⟩.

[236] E. Mäkilä, H. Kivelä, N. Shrestha, A. Correia, M. Kaasalainen, E. Kukk, J. Hirvonen, H. A. Santos, and J. Salonen. Influence of surface chemistry on ibuprofen adsorption and confinement in mesoporous silicon microparticles. *Langmuir*, 32(49):13020–13029, 2016. ⟨https://doi.org/10.1021/acs.langmuir.6b03413⟩.

[237] J. W. Chung, O. C. Edewi, J. W. Foppen, G. Gerner, R. Krebs, and P. N. L. Lens. Removal of *Escherichia coli* by intermittent operation of saturated sand columns supplemented with hydrochar derived from sewage sludge. *Appl. Sci.*, 7(8):839, 2017. ⟨https://doi.org/10.3390/app7080839⟩.

[238] U. Jakobsson, E. Mäkilä, A. J. Airaksinen, O. Alanen, A. Etile, U. Köster, S. Ranjan, J. Salonen, H. A. Santos, and K. Helariutta. Porous silicon as a platform for radiation theranostics together with a novel RIB-based radiolanthanoid. *Contrast Media & Molec. Imaging*, page 3728563, 2019. ⟨https://doi.org/10.1155/2019/3728563⟩.

[239] S. A. P. Pereira, M. L. C. Passos, A. Correia, E. Mäkilä, J. Salonen, A.R.S.T. Araujo, H. A. Santos, and M.L.M.F.S. Saraiva. Automatic methodologies to perform loading and release assays of anticancer drugs from mesoporous silicon nanoparticles. *Talanta*, 196:277–283, 2019. ⟨https://doi.org/10.1016/j.talanta.2018.12.025⟩.

[240] A. Brangule, R. Šukele, and D. Bandere. Herbal medicine characterization perspectives using advanced FTIR sample techniques – diffuse reflectance (DRIFT) and photoacoustic spectroscopy (PAS). *Front. Plant Sci.*, 11:356, 2020. ⟨https://doi.org/10.3389/fpls.2020.00356⟩.

[241] D. Lumen, S. Wang, E. Mäkilä, S. Imlimthan, M. Sarparanta, A. Correia, C. W. Haug, J. Hirvonen, H. A. Santos, A. J. Airaksinen, W. Filtvedt, and J. Salonen. Investigation of silicon nanoparticles produced by centrifuge chemical vapor deposition for applications in therapy and diagnostics. *Eur. J. Pharm. Biopharm.*, 158:254–265, 2020. ISSN 0939-6411. ⟨https://doi.org/10.1016/j.ejpb.2020.11.022⟩.

[242] S. Dugheri, D. Massi, N. Mucci, N. Berti, G. Cappelli, and G. Arcangeli. Formalin safety in anatomic pathology workflow and integrated air monitoring systems for the formaldehyde occupational exposure assessment. *Int. J. Occup. Med. Environ. Health*, 34(3):319–338, 2020. ⟨https://doi.org/10.13075/ijomeh.1896.01649⟩.

[243] M. C. de Oliveira, S. B. d. S. Ferreira, L. V. d. Castro-Hoshino, K. d. S. S. Campanholi, I. R. Calori, F. A. P. de Morais, E. Kimura, R. C. da Silva Jr., M. L. Bruschi, F. Sato, N. Hioka, and W. Caetano. Thermoresponsive hydrogel-loading aluminum chloride phthalocyanine as a drug release platform for topical administration in photodynamic therapy. *Langmuir*, 37:3202–3213, 2021. ⟨https://doi.org/10.1021/acs.langmuir.1c00148⟩.

[244] C. M. Ribeiro, M. Souza, B. L. Pelegrini, R. S. Palacios, S. M. Lima, F. Sato, A. C. Bento, M. L. Baesso, and M. M. S. Lima. Ex vivo UV–vis and FTIR photoacoustic spectroscopy of natural nanoemulsions from cellulose nanocrystals and saponins topically applied into the skin: Diffusion rates and physicochemical evaluation. *J. Photochem. Photbiol. B, Biol.*, 236:112587, 2022. ⟨https://doi.org/10.1016/j.jphotobiol.2022.112587⟩.

[245] K. d. S. S. Campanholi, R. S. Gonçalves, J. B. da Silva, R. S. d. Santos, M. C. de Oliveira, S. B. d. S. Ferreira, L. V. d. Castro-Hoshino, R. B. Balbinot, D. Lazarin-Bidói, M. L. Baesso, M. L. Bruschi, C. V. Nakamura, and W. Caetano. Thermal stimuli-responsive topical platform based on copaiba oil-resin: Design and performance upon ex-vivo human skin. *J. Mol. Liq.*, 361:119625, 2022. ⟨https://doi.org/10.1016/j.molliq.2022.119625⟩.

[246] K. d. S. S. Campanholi and et al. Copaiba oil-based emulsion as a natural chemotherapeutic agent for the treatment of bovine mastitis: In vivo studies. *Pharmaceutics*, 15(2):346, 2023. ⟨https://doi.org/10.3390/pharmaceutics15020346⟩.

[247] L. Pauling, A. B. Robinson, R. Teranishi, and P. Cary. Quantitative analysis of urine vapor and breath by gas-liquid partition chromatography. *Proc. Nat. Acad. Sci. USA*, 68(10):2374–2376, 1971. ⟨https://doi.org/10.1073/pnas.68.10.2374⟩.

[248] B. Henderson, A. Khodabakhsh, M. Metsälä, I. Ventrillard, F. M. Schmidt, D. Romanini, G. A. D. Ritchie, S. te Lintel Hekkert, R. Briot, T. Risby, N. Marczin, F. J. M. Harren, and S. M. Cristescu. Laser spectroscopy for breath analysis: towards clinical implementation. *Appl. Phys. B*, 124:161, 2018.

[249] H. Moser and B. Lendl. Cantilever-enhanced photoacoustic detection of hydrogen sulfide (H_2S) using NIR telecom laser sources near 1.6 μm. *Appl. Phys. B*, 122(4), 2016. ⟨https://doi.org/10.1007/s00340-016-6355-6⟩.

[250] X. Zhang, Z. Cheng, and X. Li. Cantilever enhanced photoacoustic spectrometry: Quantitative analysis of the trace H_2S produced by SF_6 decomposition. *Infrared Phys. Technol.*, 78:31–39, 2016. ⟨https://doi.org/10.1016/j.infrared.2016.07.004⟩.

[251] S. Larnimaa, L. Halonen, J. Karhu, T. Tomberg, M. Metsälä, G. Genoud, T. Hieta, S. Bell, and M. Vainio. High-resolution analysis of the ν_{33} band of radiocarbon methane $^{14}CH_4$. *Chem. Phys. Lett.*, 750:137488, 2020. ⟨https://doi.org/10.1016/j.cplett.2020.137488⟩.

[252] M. Fatima, T. Hausmaninger, T. Tomberg, J. Karhu, M. Vainio, T. Hieta, and G. Genoud. Radiocarbon dioxide detection using cantilever-enhanced photoacoustic spectroscopy. *Opt. Lett.*, 46 (9):2083–2086, 2021. ⟨https://doi.org/10.1364/OL.420199⟩.

[253] P. Hildén, T. Rajamäki, J. Makkonen, S. Alyshev, A. Kharakhordin, and S. Firstov. Real-time HCl gas detection at parts-per-billion level concentrations utilising a diode laser and a bismuth-doped fiber amplifier. *Meas. Sci. Technol.*, 32:055206, 2021. ⟨https://doi.org/10.1088/1361-6501/abd651⟩.

[254] G. Eggert. Saturated salt solutions in showcases: humidity control and pollutant absorption. *Herit. Sci.*, 10:54, 2022. ⟨https://doi.org/10.1186/s40494-022-00689-3⟩.

[255] R. C. E. Dias, P. Valderrama, P. H. Março, M. B. d. S. Scholz, M. Edelmann, and C. Yeretzian. Quantitative assessment of specific defects in roasted ground coffee via infrared-photoacoustic spectroscopy. *Food Chem.*, 255:132–138, 2018. ⟨https://doi.org/10.1016/j.foodchem.2018.02.076⟩.

[256] E. Hulkko, O. Lopez-Acevedo, J. Koivisto, Y. Levi-Kalisman, R. D. Kornberg, M. Pettersson, and H. Häkkinen. Electronic and vibrational signatures of the $Au_{102}(p\text{-MBA})_{44}$. *J. Am. Chem. Soc.*, 133(11):3752–3755, 2011. ⟨https://doi.org/10.1021/ja111077e⟩.

[257] Y. Moreno, R. Arrue, R. Saavedra, J.-Y. Pivan, O. Pena, and T. Roisnell. Magnetic and structural study of unsolvated [$Cu(acac)_2$], (acac= acetylacetonate). *J. Chil. Chem. Soc.*, 58(4), 2013. ⟨https://doi.org/10.4067/S0717-97072013000400049⟩.

[258] S. Janssen, K. Schmitt, M. Blanke, M. L. Bauersfeld, J. Wöllenstein, and W. Lang. Ethylene detection in fruit supply chains. *Phil. Trans. R. Soc. A*, 372:20130311, 2014. ⟨https://doi.org/10.1098/rsta.2013.0311⟩.

[259] H. Miyazaki, J. Morimoto, G. Tsuji, Y. Takiguchi, and S. Miyajima. Characterization of Cu_2O thin films by photoacoustic spectroscopy. *Proc. Symposion on Ultrasonic Electronics.*, 36, 2015.

[260] S. Kambara, Y. Hayakawa, Y. Inoue, and T. Miura. Hydrogen production from ammonia using plasma membrane reactor. *J. Sustain. Dev. Energy Water Environ. Syst.*, 4(2):193–202, 2016. ⟨https://doi.org/10.13044/j.sdewes.2016.04.0016⟩.

[261] J. Canivet, V. Lysenko, J. Lehtinen, A. Legrand, F. M. Wisser, E. A. Quadrelli, and D. Farrusseng. Sensitive photoacoustic IR-spectroscopy for the characterization of amino/azido mixed-linker metal-organic frameworks. *ChemPhysChem*, 18(20):2855–2858, 2017. ⟨https://doi.org/10.1002/cphc.201700663⟩.

[262] W. Gac, W. Zawadzki, G. Slowik, A. Sienkiewicz, and A. Kierys. Nickel catalysts supported on silica microspheres for CO_2 methanation. *Microporous Mesoporous Mater.*, 272(8):79–91, 2018. ⟨https://doi.org/10.1016/j.micromeso.2018.06.022⟩.

[263] F. Lederle, C. Härter, and S. Beuermann. Inducing β phase crystallinity of PVDF homopolymer, blends and block copolymers by anti-solvent crystallization,. *J. Fluor. Chem.*, 234:109522, 2020. ISSN 0022-1139. ⟨https://doi.org/10.1016/j.jfluchem.2020.109522⟩.

[264] H. Cheng, X. Zhang, C. Bian, J. Cheng, Z. Chen, Y. Zhang, J. Tang, and S. Xiao. Photoacoustic spectroscopy: Trace CO detection by using 10 mW near-infrared laser and cantilever beam. *AIP Advances*, 10:105122, 2020. ⟨https://doi.org/10.1063/1.5134882⟩.

[265] F. Ma, Z. Liao, Y. Zhao, Z. Qiu, L. Wan, K. Li, and G. Zhang. Detection of trace C_2H_2 in N_2 buffer gas with cantilever-enhanced photoacoustic spectrometer. *Optik*, 232:166525, 2021. ISSN 0030-4026. ⟨https://doi.org/10.1016/j.ijleo.2021.166525⟩.

[266] S. Koziel, P. Hilber, P. Westerlund, and E. Shayesteh. Investments in data quality: Evaluating impacts of faulty data on asset management in power systems. *Appl. Energy*, 281:116057, 2021. ⟨https://doi.org/10.1016/j.apenergy.2020.116057⟩.

[267] T. Yamagishi, Y. Sakai, T. Takayama, S. Shibutani, and S. Yamauchi. Characterization of iron-loaded charcoal using infrared-photoacoustic spectroscopy: factors governing graphitization. *Wood. Sci. Tech.*, 57:229–252, 2023. ⟨https://doi.org/10.1007/s00226-022-01436-4⟩.

[268] T. Kuusela, J. Peura, B. A. Matveev, M. A. Remennyy, and N. M. Stus. Photoacoustic gas detection using a cantilever microphone and III–V mid-IR LEDs. *Vib. Spectrosc.*, 51:289–293, 2009. ⟨https://doi.org/10.1016/j.vibspec.2009.08.001⟩.

[269] N. E. Glauvitz, R. A. Coutu Jr., I. R. Medvedev, and D. T. Petkie. *MEMS-Based Terahertz Photoacoustic Chemical Sensing System*. IntechOpen, 2016. ISBN 978-953-2533-4. ⟨https://doi.org/10.5772/62571⟩.

[270] A. Brangule, L. Avotiņa, A. Zariņš, M. Haļitovs, K. A. Gross, and G. Kizane. Thermokinetic investigation of the drying conditions on amorphous calcium phosphate. *Key Eng. mater.*, 758: 204–209, 2017. ⟨https://doi.org/10.4028/www.scientific.net/KEM.758.204⟩.

[271] R. C. E. Dias, P. Valderrama, P. H. Março, M. B. d. S. Scholz, M. Edelmann, and C. Yeretzian. Data on roasted coffee with specific defects analyzed by infrared-photoacoustic spectroscopy and chemometrics. *Data in Brief*, 20:242–249, 2018. ⟨https://doi.org/10.1016/j.dib.2018.08.013⟩.

[272] V. Sallet, C. Sartel, S. Hassani, C. Vilar, G. Amiri, A. Lusson, F. Jomard, P. Galtier, I. Lefebvre, C. Delerue, M. K. Hamza, B. Canut, and B. Masenelli. Crystal facet engineering in Ga-doped ZnO nanowires for mid-infrared plasmonics. *Cryst. Growth Des.*, 18(8):4287–4295, 2018. ⟨https://doi.org/10.1021/acs.cgd.8b00048⟩.

[273] K. Chen, Z. Yu, Q. Yu, M. Guo, Z. Zhao, C. Qu, Z. Gong, and Y. Yang. Fast demodulated white-light interferometry-based fiber-optic fabry-perot cantilever microphone. *Opt. Lett.*, 43 (14):3417–3420, 2018. ⟨https://doi.org/10.1364/OL.43.003417⟩.

[274] J. Karhu, T. Hieta, F. Manoocheri, M. Vainio, and E. Ikonen. Led-based photoacoustic NO_2 sensor with a sub-ppb detection limit. *ACS Sens.*, 6(9):3303–3307, 2021. ⟨https://doi.org/10.1021/acssensors.1c01073⟩.

[275] J. Rossi, J. Uotila, S. Sharma, T. Laurila, R. Teissier, A. Baranov, E. Ikonen, and M. Vainio. Photoacoustic characteristics of carbon-based infrared absorbers. *Photoacoustics*, 23:100265, 2021. ⟨https://doi.org/10.1016/j.pacs.2021.100265⟩.

[276] C. M. Stevenson, A. K. Rogers, S. W. Novak, W. Ambrose, and T. N. Ladefoged. A molecular model for obsidian hydration dating. *J. Archaeol. Sci. Rep.*, 36:102824, 2021. ISSN 2352-409X. ⟨https://doi.org/10.1016/j.jasrep.2021.102824⟩.

[277] S. Sharma, T. Laurila, J. Rossi, J. Uotila, M. Vainio, F. Manoocheri, and E. Ikonen. Electromagnetic radiation detection using cantilever-based photoacoustic effect: A method for realizing power detectors with broad spectral sensitivity and large dynamic range. *Sens. Actuators A Phys.*, 2021. ⟨https://doi.org/10.1016/j.sna.2021.113191⟩.

[278] S. Sharma, M. Ahmadi, J. Rossi, M. Vainio, Z. Sun, A. Steiger, and E. Ikonen. Terahertz radiation detection with a cantilever-based photoacoustic sensor. *Opt. Exp.*, 30(24):43417–43425, 2022. ⟨https://doi.org/10.1364/OE.469295⟩.

[279] J. Rossi, J. Uotila, S. Sharma, T. Hieta, T. Laurila, R. Teissier, A. Baranov, E. Ikonen, and M. Vainio. Optical power detector with broad spectral coverage, high detectivity and large dynamic range. *Opt. Lett.*, 47(7):1689–1692, 2022. ⟨https://doi.org/10.1364/OL.455191⟩.

[280] M. Isaiev, G. Mussabek, P. Lishchuk, K. Dubyk, N. Zhylkybayeva, G. Yar-Mukhamedova, D. Lacroix, and V. Lysenko. Application of the photoacoustic approach in the characterization of nanostructured materials. *Nanomater.*, 125(4):708, 2022. ⟨https://doi.org/10.3390/nano12040708⟩.

[281] S. Larnimaa, M. Roiz, and M. Vainio. Photoacoustic phase-controlled fourier-transform infrared spectroscopy. *Opt. Continuum*, 2(3):564–578, 2023. ⟨https://doi.org/10.1364/OPTCON.483779⟩.

TURUN
YLIOPISTO
UNIVERSITY
OF TURKU

ISBN 978-951-29-9612-4 (PRINT)
ISBN 978-951-29-9613-1 (PDF)
ISSN 0082-7002 (PRINT)
ISSN 2343-3175 (ONLINE)

Painosalama Oy, Turku, Finland 2024